SINGLE-CRYSTAL GROWTH OF ORGANIC SEMICONDUCTORS AND ORGANIC ELECTRONIC APPLICATIONS

Bumjung Kim

Submitted in partial fulfillment of the
requirements for the degree of
Doctor of Philosophy
in the Graduate School of Arts and Sciences

COLUMBIA UNIVERSITY

2011

TABLE OF CONTENTS

LIST OF TABLES AND FIGURES

DEDICATION

I DEDICATE THIS THESIS TO GOD, MY LORD AND SAVIOR. TO MY FIANCÉE SARAH JOOYEON CHONG AND MY PARENTS; FOR THE UNDERSTANDING AND ENCOURAGEMENT THEY PROVIDED DURING ALL THESE YEARS OF STUDY. I LOVE YOU.

Remember how the LORD your God led you all the way in the wilderness these forty years, to humble and test you in order to know what was in your heart, whether or not you would keep his commands. He humbled you, causing you to hunger and then feeding you with manna, which neither you nor your ancestors had known, to teach you that man does not live on bread alone but on every word that comes from the mouth of the LORD.

DEUTRONOMY 8:2-3

Chapter 1

INTRODUCTION

1.1 Organic Semiconductors

We are now living in days of technology; we work, play, and fulfill our needs using high technology electronic devices in our daily lives. Since the first transistor was invented in 1947, people have been developing numerous technologies using these devices. Silicon-based inorganic devices have been the most predominantly used in electronics due to their high performance. However, the use of silicon necessitates high cost instrumentation using high temperature and high vacuum systems. Moreover, silicon-based devices are not environmentally favorable due to massive heavy metal usage.

As alternatives to silicon and other inorganic semiconductors, the study of organic semiconductors emerged. From the 1980s, organic semiconductors showed drastic improvement and their performance has reached up to that of amorphous silicon transistors.[1] (Figure 1-1) Moreover, organic semiconductors can be deposited at low temperature, and processed from solution, which enables large area printing without using a high vacuum system.[1-5] There have been various printing techniques developed using organic semiconductors: screen-printing,[6] ink-jet printing,[7-10] and microcontact printing.[11-13] Also, low temperature and low energy processes are key to flexible, transparent device fabrication, as film deposition on plastic substrates, such as polyethylene terephthalate film (PET), is possible.[14-17] These strengths give great potential in future electronics such as light-emitting diodes (LED) and photovoltaic cells (PVC).

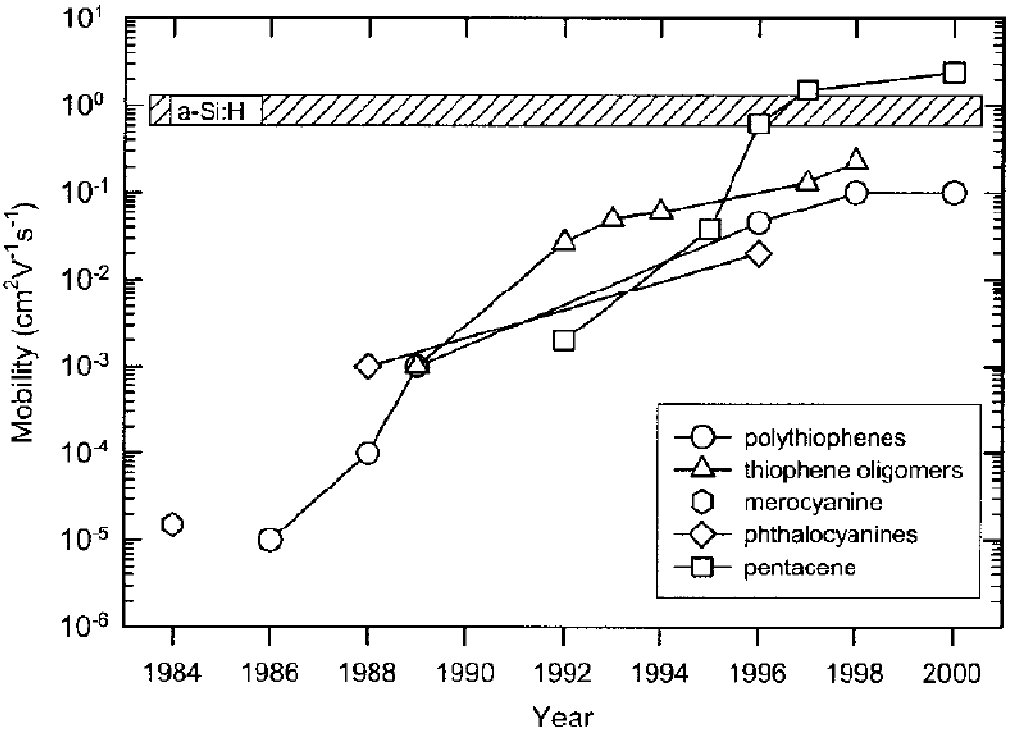

Figure 1-1 Evolution of organic field-effect transistors for the most common p-type organic semiconductors. This graph is reproduced from Reference [1].

In this study, we investigate semiconducting characteristics of polyaromatic hydrocarbon compounds, such as hexabenzocoronene, dibenzotetrathienocoronene and rubrene, through field-effect transistor (FET) and solar cell (SC) fabrications, and study their morphology change to improve their electrical properties.

1.2 Single Crystals of Organic Semiconductors

A crystal is defined as a uniformly ordered form of atoms or molecules. Every material has its own packing order, and the crystal packing structure is crucial to studying intrinsic characteristics of materials. Especially in molecular electronics, the way molecules are packed is critical to the performance of devices. More detail about charge transport in small molecules will be covered later. (Chapter 1.4)

As the crystallinity of organic films improve the performance of organic devices, organic single-crystals are the best form to study intrinsic charge carrier characteristics of organic semiconductors.[18-21] Earlier, the time-of-flight mobility of naphthalene single-crystal was found to be 400 cm^2/Vs under 10 K, which surpasses the performance of amorphous silicon device.[22] More recently, field-effect transistors of rubrene and pentacene single-crystal showed high hole-transport mobility above 20 cm^2/Vs, even in ambient room temperature condition.[23,24] This value outperforms compared to those of organic thin-film transistors, 0.001 ~ 0.1 cm^2/Vs.[25] The high performance of organic single-crystal devices give great promise in future organic electronics.

Single-crystals can be grown using physical vapor deposition (PVD) method. [26] This system is made up of a temperature gradient furnace and inert gas flowing tube. (Figure 1-2) Powder of the organic semiconductor is placed at the high temperature zone and the system is heated under inert carrier gas conditions. The molecule slowly vaporizes and crystallizes in the lower temperature zone. The temperature and flow rate of the carrier gas can vary depending on the material and preferable crystal shape.

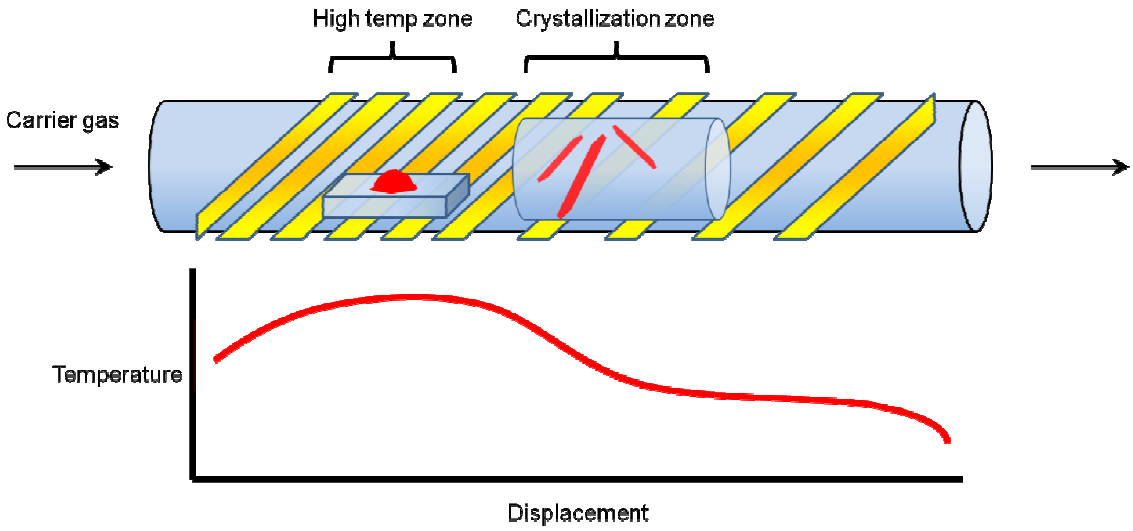

Figure 1-2 Schematics of physical vapor deposition system.

PVD method can grow single crystals of most organic semiconductors although there are some exceptions. If the molecule has long alkyl chains or double bonds, the molecule changes its conformation at high temperature, which hinders uniform packing to form crystals. Organic molecules with long sp^3-chains are not favorable for PVD crystal growth.

The images of single-crystals studied in this paper are shown in Figure 1-3. In Chapter 3, we used rubrene single-crystals to fabricate high mobility organic field-effect transistors. Chapter 4 mainly studies the surface dependence of dibenzotetrathienocoronene (DBTTC) crystal growth and its application. In Chapter 5, we studied co-crystals of hexabenzocoronene (HBC) and C_{60}, which helps understanding the effect of crystallinity in the bilayer interface of HBC and C_{60} in solar cells.

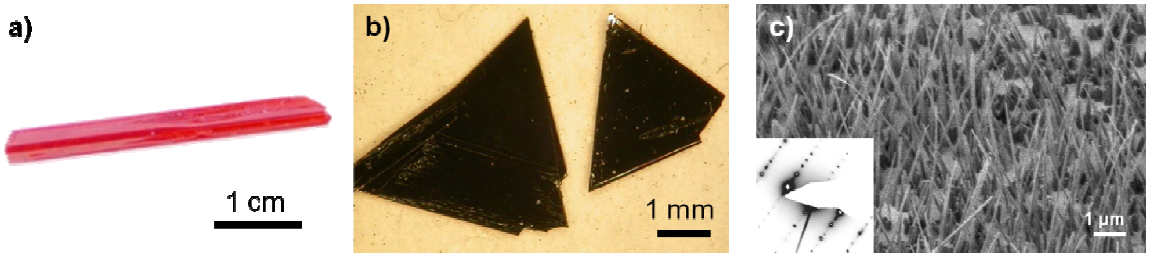

Figure 1-3 Single crystals grown in a PVD system: (a) rubrene, (b) C_{60}, and (c) DBTTC. (The inset shows TEM diffraction of DBTTC single-crystal)

1.3 Carbon Crystals: C_{60}, Carbon Nanotubes, and Graphene

It is well known that carbon has two different crystal structures: diamond (tetrahedral packing) and graphite (hexagonal packing). However in 1985, a soccer-ball shaped carbon crystal made up of 60 carbon atoms was found by the Smalley group in Rice University.[27] In 1991, Ijima found a tubular structure of carbon crystal, also known as a carbon nanotube (CNT).[28] Graphene, a planar sheet of sp^2-bonded carbon atoms, has been theoretically studied for sixty years,[29-31] while experimentation has been more recent due to the development of a novel way to get single-layer graphene from graphite.[32] All of these carbon crystals are called “fullerene”, and unlike diamond, all the bonding in these materials is π-bonding. As a result, sp^2-hybrid orbitals can be a channel for charge carrier transport, which gives exceptional metallic or semiconducting characteristics.

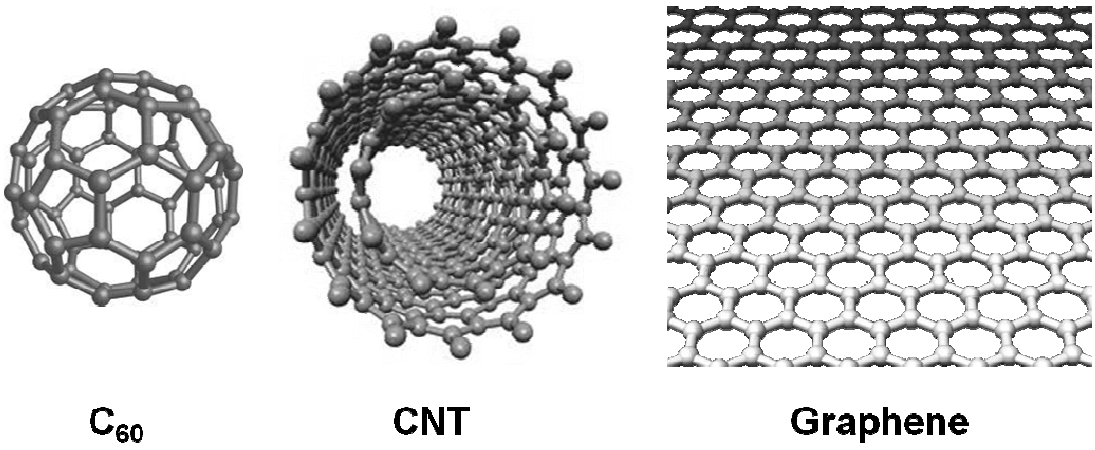

Figure 1-4 Structures of C_{60}, carbon nanotubes, and graphene. [33]

C_{60} is one of the most famous n-type organic semiconductor materials with mobility of 0.6 ~ 6 cm^2/Vs.[34-36] The most unique characteristic of C_{60} is super-conductivity at low temperature (18 K) when doped with alkali metals.[37-39] However, C_{60} thin films are quite sensitive to air and were unable to work in ambient condition. The actual application of C_{60} became more feasible when C_{60} was chemically modified. Numerous studies have been done to find air-stable and solution-processible C_{60} derivatives, and some of them, such as phenyl-C61-butyric acid methyl ester ([60] PCBM)[40], are now widely used in organic electronics. [41]

Carbon nanotubes (CNT) were found during the synthesis of fullerenes.[28] CNT is a crystal of carbon with a tubular structure, which has a length-to-diameter ratio up to 132,000,000 : 1.[42] The electrical and chiral characteristics of a CNT can be understood by the way it is rolled up. Considering that a CNT can be made by rolling up a graphene nanoribbon, the circumference of the CNT can be expressed as vector . By dividing into two different unit vector and , (n, m) can be decided based on the number of carbons along the and vectors.(Figure 1-5) These numbers can be used to determine if a CNT

is semiconducting or metallic.[43-46] Metallic nanotubes can be used as cathode-ray tubes,[47] scanning probe microscopy (SPM) tips,[48] single-molecular junction electrodes[49], or as transparent electrode films.[50,51] Semiconductor nanotubes can be used as nanowire field-effect transistors.[52,53] However, CNT application still suffers from its separation problem; the CNT growth produces both semiconductor and metallic CNTs and efficient way to separate them is crucial to CNT applications. There have been numerous methods to separate metallic and semiconductor nanotubes: dielectrophoresis,[54,55] density gradient centrifugation,[56] and chemical methods using functionalization.[57,58] Recently, Jin Zhang group found a facile way to separate nanotubes using scotch tape[59], although this method still needs further investigation.

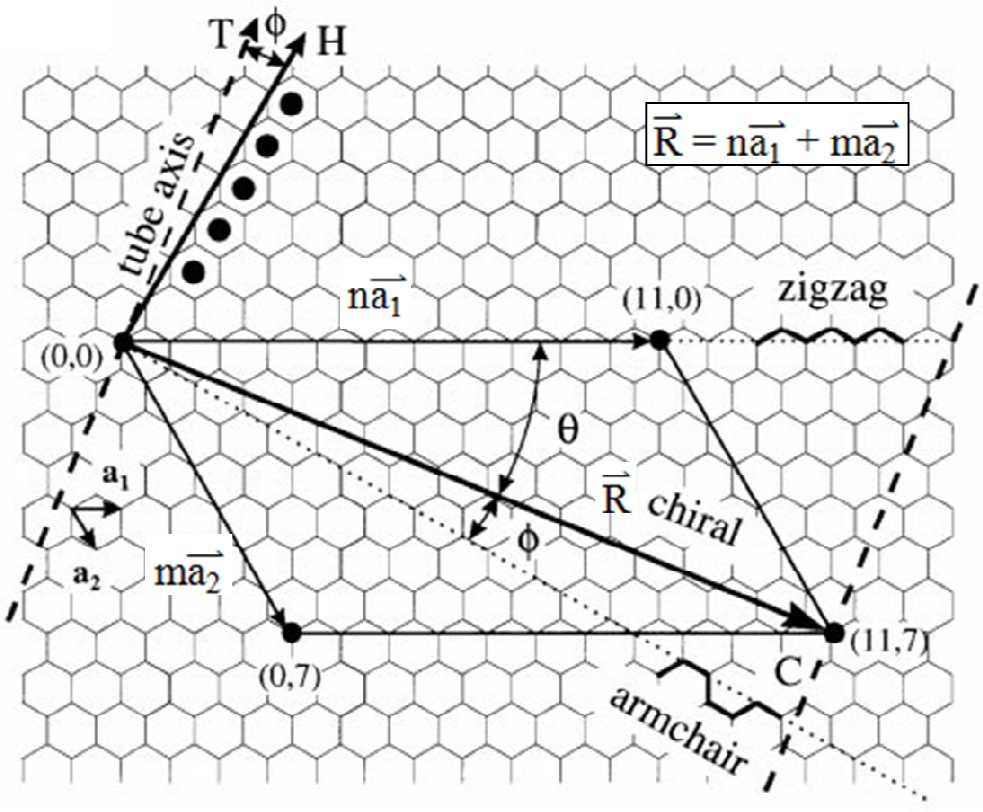

Figure 1-5 Relation between the hexagonal carbon lattice and the chirality of carbon nanotubes.[43]

Graphene, a single-layer version of graphite, has caught great interest because of its optical transparency (~98 %),[60] single-atomic thickness, and low electrical resistance.[61,62] Moreover, large-scale graphene growth using chemical vapor deposition (CVD) method opened various application possibilities as an organic electrode.[63,64] Especially, large-scale graphene shows great potential in organic optoelectric devices, such as solar cells (SC)[65-69] or light emitting diodes (LED)[70,71], as it promises high transparency as well as high conductivity.

In Chapter 2, a C_{60} thin film was used as an n-type semiconductor in field-effect transistors and the crystallinity dependence of this film on self-assembled monolayer surfaces was studied. Chapter 3 shows a non-destructive way to make graphene patterns which enables using graphene as source and drain electrode in OFETs.

1.4 Organic Field-Effect Transistors

Since organic semiconductors were discovered, there have been various measurements to study electrical characteristics of organic semiconductors. The time-of-flight (TOF)[72,73] and space charge limited current (SCLC) measurements[74] were performed to measure charge mobility along the vertical direction of organic semiconductor films.[75] Field-effect transistors (FET), on the other hand, measure the current along the source and drain electrode as the electric field applied from the gate electrode changes. Hence, FET is more suitable for studying the actual charge mobility of organic films along the surface direction.

However, unlike inorganic FETs, organic FETs have different charge transport mechanisms [76] and other approaches are required to improve their performance; surface

morphology (crystallinity), Schottky barrier, dielectric capacitance, and other factors are critical to the improvement of organic FETs.

In this thesis, as part of these efforts, we studied the effect of self-assembled monolayers (Chapter 2) and ultrathin organic electrodes (Chapter 3) as ways of improving FET devices.

1.5 Organic Solar Cells

Among numerous applications of organic semiconductors, organic solar cells are compelling due to their light weight, low-cost and flexibility.[77-80] The best organic solar cell was known to be a bulk heterojunction(BHJ) solar cell made up of poly-3-hexylthiophene (P3HT) and phenyl C_{60} butyric acid methyl ester (PCBM).[81,82] These devices can reach ~6 % efficiency, which is getting closer to that of amorphous silicon solar cells (13 %).[83] BHJ solar cells take advantage of the large interfacial area between *p* and *n*-type semiconductors. This architecture is made by depositing *p* and *n*-type semiconductors together so that they can be mixed. Phase separation occurs, resulting in numerous small domain formations with a drastically increased interface compared with a bilayer architecture. Considering that the exciton generation and charge transport in organic solar cell is highly dependent on the surface area of the *p*-*n* interface and diffusion length,[84-86] BHJ solar cells can be an easy and useful way to make organic solar cells with good efficiency.

However, the random phase separation of the BHJ film is not well controlled and further investigation of the film morphology is difficult due to random morphology. A deeper understanding of the film structure and morphology is necessary to reach higher solar cell efficiency. In this context, people have tried to make morphology-controlled

heterojunctions.[87-89] The important factors are the crystallinity and size of each material; each film thickness (or size) should be in good range of exciton diffusion, but the film should be crystalline enough to maximize charge transport. These is area that, although it has been somewhat studied, there is still a need for a deeper understanding and further insight to spur progress..

As part of these efforts, we attempted to grow single-crystals of dibenzotetrathieno-coronene (DBTTC) vertically on graphene films and to make solar cells using this nanopillar structure. (Chapter 4) Also in Chapter 5, the crystallizing effect of hexabenzocoronene (HBC) and C_{60} at the interface was studied when a bilayer of HBC and C_{60} was used in solar cells.

References for Chapter 1

[1] Dimitrakopoulos, C. D.; Malenfant, P. R. L. *Advanced Materials* **2002**, *14*, 99.

[2] Bao, Z.; A. Rogers, J.; E. Katz, H. *Journal of materials chemistry* **1999**, *9*, 1895.

[3] Horowitz, G. *Journal of materials chemistry* **1999**, *9*, 2021.

[4] Mas-Torrent, M.; Rovira, C. *Chemical Society Reviews* **2008**, *37*, 827.

[5] Murphy, A. R.; Fréchet, J. M. J. *Chemical Reviews* **2007**, *107*, 1066.

[6] Bao, Z.; Feng, Y.; Dodabalapur, A.; Raju, V. R.; Lovinger, A. J. *Chemistry of Materials* **1997**, *9*, 1299.

[7] Bharathan, J. *Applied physics letters* **1998**, *72*, 2660.

[8] Chang, S. C.; Bharathan, J.; Yang, Y.; Helgeson, R.; Wudl, F.; Ramey, M. B.; Reynolds, J. R. *Applied physics letters* **1998**, *73*, 2561.

[9] Hebner, T. R.; Sturm, J. C. *Applied physics letters* **1998**, *73*, 1775.

[10] Hebner, T. R.; Wu, C. C.; Marcy, D.; Lu, M. H.; Sturm, J. C. *Applied physics letters* **1998**, *72*, 519.

[11] Rogers, J. A.; Bao, Z.; Makhija, A.; Braun, P. *Advanced Materials* **1999**, *11*, 741.

[12] Rogers, J. A.; Bao, Z. N.; Dhar, L. *Applied physics letters* **1998**, *73*, 294.

[13] Rogers, J. A.; Bao, Z. N.; Raju, V. R. *Applied physics letters* **1998**, *72*, 2716.

[14] Rogers, J. A.; Huang, Y. *Proceedings of the National Academy of Sciences* **2009**, *106*, 10875.

[15] Rogers, J. A.; Someya, T.; Huang, Y. *Science* **2010**, *327*, 1603.

[16] Sekitani, T.; Noguchi, Y.; Hata, K.; Fukushima, T.; Aida, T.; Someya, T. *Science* **2008**, *321*, 1468.

[17] Service, R. F. *Science* **1997**, *278*, 383.

[18] de Boer, R. W. I. W. *Physica status solidi. A, Applied research* **2004**, *201*, 1302.

[19] Hasegawa, T. *Science and technology of advanced materials* **2009**, *10*, No.

[20] Jiang, L. *Journal of materials chemistry* **2010**, *20*, 4994.

[21] Reese, C.; Bao, Z. *Materials Today* **2007**, *10*, 20.

[22] Warta, W. *Physical review. B, Condensed matter* **1985**, *32*, 1172.

[23] Sundar, V. C. *Science (New York, N.Y.)* **2004**, *303*, 1644.

[24] Jurchescu, O. D. *Applied physics letters* **2004**, *84*, 3061.

[25] Dimitrakopoulos, C. D.; Mascaro, D. J. *Ibm J Res Dev* **2001**, *45*, 11.

[26] Laudise, R. A.; Kloc, C.; Simpkins, P. G.; Siegrist, T. *Journal of crystal growth* **1998**, *187*, 449.

[27] Kroto, H. W.; Heath, J. R.; O'Brien, S. C.; Curl, R. F.; Smalley, R. E. *Nature* **1985**, *318*, 162.

[28] Iijima, S. *Nature* **1991**, *354*, 56.

[29] McClure, J. W. *Physical Review* **1956**, *104*, 666.

[30] Wallace, P. R. *Physical Review* **1947**, *71*, 622.

[31] Slonczewski, J. C.; Weiss, P. R. *Physical Review* **1958**, *109*, 272.

[32] Novoselov, K. S.; Geim, A. K.; Morozov, S. V.; Jiang, D.; Zhang, Y.; Dubonos, S. V.; Grigorieva, I. V.; Firsov, A. A. *Science* **2004**, *306*, 666.

[33] The images are taken from suite101.com(C60), r. c. C., and gizmag.com(graphene).

[34] Anthopoulos, T. D. *Applied physics letters* **2006**, *89*, 213504.

[35] Haddon, R. C. *Applied physics letters* **1995**, *67*, 121.

[36] Singh, T. B.; Marjanovic, N.; Matt, G. J.; Gunes, S.; Sariciftci, N. S.; Ramil, A. M.; Andreev, A.; Sitter, H.; Schwodiauer, R.; Bauer, S. *Org Electron* **2005**, *6*, 105.

[37] Gunnarsson, O. *Reviews of Modern Physics* **1997**, *69*, 575.

[38] Hebard, A. F.; Rosseinsky, M. J.; Haddon, R. C.; Murphy, D. W.; Glarum, S. H.; Palstra, T. T. M.; Ramirez, A. P.; Kortan, A. R. *Nature* **1991**, *350*, 600.

[39] Haddon, R. C.; Hebard, A. F.; Rosseinsky, M. J.; Murphy, D. W.; Duclos, S. J.; Lyons, K. B.; Miller, B.; Rosamilia, J. M.; Fleming, R. M.; Kortan, A. R.; Glarum, S. H.; Makhija, A. V.; Muller, A. J.; Eick, R. H.; Zahurak, S. M.; Tycko, R.; Dabbagh, G.; Thiel, F. A. *Nature* **1991**, *350*, 320.

[40] Hummelen, J. C.; Knight, B. W.; LePeq, F.; Wudl, F.; Yao, J.; Wilkins, C. L. *The Journal of Organic Chemistry* **1995**, *60*, 532.

[41] Björström, C. M.; et al. *Journal of Physics: Condensed Matter* **2005**, *17*, L529.

[42] Wang, X.; Li, Q.; Xie, J.; Jin, Z.; Wang, J.; Li, Y.; Jiang, K.; Fan, S. *Nano letters* **2009**, *9*, 3137.

[43] Wilder, J. W. G.; Venema, L. C.; Rinzler, A. G.; Smalley, R. E.; Dekker, C. *Nature* **1998**, *391*, 59.

[44] Dekker, C. *Phys Today* **1999**, *52*, 22.

[45] Odom, T. W.; Huang, J.-L.; Kim, P.; Lieber, C. M. *Nature* **1998**, *391*, 62.

[46] Mintmire, J. W.; Dunlap, B. I.; White, C. T. *Physical review letters* **1992**, *68*, 631.

[47] Saito, Y.; Uemura, S.; Hamaguchi, K. *Japanese Journal of Applied Physics Part 2-Letters & Express Letters* **1998**, *37*, L346.

[48] Dai, H.; Hafner, J. H.; Rinzler, A. G.; Colbert, D. T.; Smalley, R. E. *Nature* **1996**, *384*, 147.

[49] Guo, X.; Small, J. P.; Klare, J. E.; Wang, Y.; Purewal, M. S.; Tam, I. W.; Hong, B. H.; Caldwell, R.; Huang, L.; O'Brien, S.; Yan, J.; Breslow, R.; Wind, S. J.; Hone, J.; Kim,

P.; Nuckolls, C. *Science* **2006**, *311*, 356.

[50] Hu, L.; Hecht, D. S.; Grüner, G. *Nano letters* **2004**, *4*, 2513.

[51] Wu, Z.; Chen, Z.; Du, X.; Logan, J. M.; Sippel, J.; Nikolou, M.; Kamaras, K.; Reynolds, J. R.; Tanner, D. B.; Hebard, A. F.; Rinzler, A. G. *Science* **2004**, *305*, 1273.

[52] Tans, S. J.; Devoret, M. H.; Dai, H. J.; Thess, A.; Smalley, R. E.; Geerligs, L. J.; Dekker, C. *Nature* **1997**, *386*, 474.

[53] Tans, S. J.; Verschueren, A. R. M.; Dekker, C. *Nature* **1998**, *393*, 49.

[54] Moshammer, K.; Hennrich, F.; Kappes, M. *Nano Research* **2009**, *2*, 599.

[55] Krupke, R.; Hennrich, F.; Löhneysen, H. v.; Kappes, M. M. *Science* **2003**, *301*, 344.

[56] Arnold, M. S.; Green, A. A.; Hulvat, J. F.; Stupp, S. I.; Hersam, M. C. *Nat Nano* **2006**, *1*, 60.

[57] Chen, Z.; Du, X.; Du, M.-H.; Rancken, C. D.; Cheng, H.-P.; Rinzler, A. G. *Nano letters* **2003**, *3*, 1245.

[58] Strano, M. S.; Dyke, C. A.; Usrey, M. L.; Barone, P. W.; Allen, M. J.; Shan, H.; Kittrell, C.; Hauge, R. H.; Tour, J. M.; Smalley, R. E. *Science* **2003**, *301*, 1519.

[59] Hong, G.; Zhou, M.; Zhang, R.; Hou, S.; Choi, W.; Woo, Y. S.; Choi, J.-Y.; Liu, Z.; Zhang, J. *Angewandte Chemie International Edition* **2011**, *50*, 6819-6823.

[60] Nair, R. R. *Science (New York, N.Y.)* **2008**, *320*, 1308.

[61] Novoselov, K. S.; Geim, A. K.; Morozov, S. V.; Jiang, D.; Katsnelson, M. I.; Grigorieva, I. V.; Dubonos, S. V.; Firsov, A. A. *Nature* **2005**, *438*, 197.

[62] Zhang, Y.; Tan, Y.-W.; Stormer, H. L.; Kim, P. *Nature* **2005**, *438*, 201.

[63] Kim, K. S. *Nature (London)* **2009**, *457*, 706.

[64] Li, X. *Science (New York, N.Y.)* **2009**, *324*, 1312.

[65] Wu, J. B.; Becerril, H. A.; Bao, Z. N.; Liu, Z. F.; Chen, Y. S.; Peumans, P. *Applied physics letters* **2008**, *92*.

[66] Wang, Y.; Chen, X. H.; Zhong, Y. L.; Zhu, F. R.; Loh, K. P. *Applied physics letters* **2009**, *95*.

[67] Wang, X.; Zhi, L. J.; Tsao, N.; Tomovic, Z.; Li, J. L.; Mullen, K. *Angew Chem Int Edit* **2008**, *47*, 2990.

[68] Eda, G.; Lin, Y. Y.; Miller, S.; Chen, C. W.; Su, W. F.; Chhowalla, M. *Applied physics letters* **2008**, *92*.

[69] De Arco, L. G.; Zhang, Y.; Schlenker, C. W.; Ryu, K.; Thompson, M. E.; Zhou, C. W. *ACS nano* **2010**, *4*, 2865.

[70] Wu, J.; Agrawal, M.; Becerril, H. c. A.; Bao, Z.; Liu, Z.; Chen, Y.; Peumans, P. *ACS nano* **2009**, *4*, 43.

[71] Matyba, P.; Yamaguchi, H.; Eda, G.; Chhowalla, M.; Edman, L.; Robinson, N. D. *ACS nano* **2010**, *4*, 637.

[72] Kepler, R. G. *Applied physics letters* **1995**, *66*, 3618.

[73] Meyer, H.; Haarer, D.; Naarmann, H.; ouml; rhold, H. H. *Phys Rev B* **1995**, *52*, 2587.

[74] Shen, Y. L.; Hosseini, A. R.; Wong, M. H.; Malliaras, G. G. *Chemphyschem* **2004**, *5*, 16.

[75] Murphy, A. R.; Frechet, J. M. J. *Chemical Reviews* **2007**, *107*, 1066.

[76] Newman, C. R.; Frisbie, C. D.; da Silva, D. A.; Bredas, J. L.; Ewbank, P. C.; Mann, K. R. *Chemistry of Materials* **2004**, *16*, 4436.

[77] Granstrom, M.; Petritsch, K.; Arias, A. C.; Lux, A.; Andersson, M. R.; Friend, R. H. *Nature* **1998**, *395*, 257.

[78] Halls, J. J. M.; Walsh, C. A.; Greenham, N. C.; Marseglia, E. A.; Friend, R. H.; Moratti, S. C.; Holmes, A. B. *Nature* **1995**, *376*, 498.

[79] Tang, C. W. *Applied physics letters* **1986**, *48*, 183.

[80] Yu, G.; Gao, J.; Hummelen, J. C.; Wudl, F.; Heeger, A. J. *Science* **1995**, *270*, 1789.

[81] Park, S. H.; Roy, A.; Beaupre, S.; Cho, S.; Coates, N.; Moon, J. S.; Moses, D.; Leclerc, M.; Lee, K.; Heeger, A. J. *Nat Photon* **2009**, *3*, 297.

[82] Peet, J.; Kim, J. Y.; Coates, N. E.; Ma, W. L.; Moses, D.; Heeger, A. J.; Bazan, G. C. *Nat Mater* **2007**, *6*, 497.

[83] Wronski, C. R.; Pearce, J. M.; Koval, R. J.; Ferlauto, A. S.; Collins, R. W. *RIO 02 – World Climate & Energy Event*, **2002**, *Jan. 8th*.

[84] Benanti, T.; Venkataraman, D. *Photosynthesis Research* **2006**, *87*, 73.

[85] Deibel, C.; Dyakonov, V. *Reports on Progress in Physics* **2010**, *73*.

[86] Lloyd, M. T.; Anthony, J. E.; Malliaras, G. G. *Materials Today* **2007**, *10*, 34.

[87] Chu, T.-Y. *Applied physics letters* **2011**, *98*, 253301.

[88] Mawyin, J.; Shupyk, I.; Wang, M.; Poize, G.; Atienzar, P.; Ishwara, T.; Durrant, J. R.; Nelson, J.; Kanehira, D.; Yoshimoto, N.; Martini, C.; Shilova, E.; Secondo, P.; Brisset, H.; Fages, F.; Ackermann, J. r. *The Journal of Physical Chemistry C* **2011**, *115*, 10881.

[89] Yang, F.; Shtein, M.; Forrest, S. R. *Nat Mater* **2005**, *4*, 37.

Chapter 2

CRYSTALLINITY CONTROL OF C_{60} THIN FILM USING C_{60} SELF-ASSEMBLED MONOLAYERS AND THIN-FILM TRANSISTOR FABRICATION*

* Part of this chapter was reproduced with permission from *Chemistry of Materials*:
"Simple Formation of C_{60} and C_{60}-Ferrocene Conjugated Monolayers Anchored onto Silicon Oxide with Five Carboxylic Acids and Their Transistor Applications" by Yoshimitsu Itoh, Bumjung Kim, Raluca I. Gearba, Noah J. Tremblay, Ron Pindak, Yutaka Matsuo, Eiichi Nakamura, and Colin Nuckolls. © 2011 American Chemical Society.
*My contribution on this study was focused on C_{60} thin-film transistor fabrication and device measurements. C_{60} derivative synthesis and self-assembly were done by Dr. Yoshimitsu Itoh.

2.1 Background

C_{60}, also known as buckminsterfullerene,[1] is an attractive material for electronic applications, such as photovoltaics[2-4] and FETs[5-7] as suggested by its high electron mobilities.[8,9] Of particular interests are the SAMs[10] of C_{60} showing unique properties and potential for advanced electronic applications.[11] There have been many studies of a monolayer of C_{60} derivatives on gold, ITO, or other substrates.[12-21] However, compared to the monolayer on gold, there are only a few reports for the formation of fullerene monolayers on silicon oxide surfaces[22-30] that are important for electronic device applications especially for organic FETs. Moreover, all of these prior studies involve covalent functionalization on silicon oxide surfaces. Some of them make a reaction of C_{60} itself with a nitrogen functional group on the surface[23-25,29], which have a possibility for an incomplete reaction of C_{60}, and the others make a reaction utilizing the C_{60} itself or prefunctionalized C_{60} with the surface using a coupling reagent[22,26-28,30], which might

result in a contamination of the surface. Therefore, it is difficult to avoid making a SiO_2 surface with a nonuniform electronic structure. Here, we suggest a simple way to form monolayers of C_{60} derivatives on silicon oxide surfaces by using SAMs of C_{60} molecules functionalized with five carboxylic acids (Figure 1). We also demonstrate the usefulness of these SAMs for organic FET applications using the C_{60} molecule itself and contorted hexabenzocoronene (HBC)[31] (Figure 1).

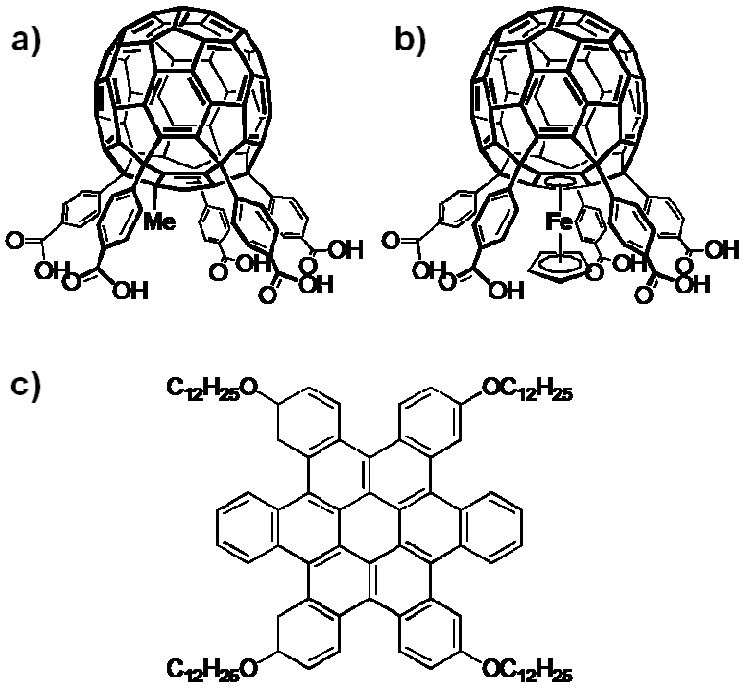

Figure 2-1 Molecular structure of the C_{60} derivatives (a) C_{60}(Ph-COOH)$_5$, (b) C_{60}(Ph-COOH)$_5$Fc, and (c) hexabenzocoronene (HBC).

2.2 C_{60} Monolayer Formation Using C_{60} Derivatives with Five Carboxylic Acids

C_{60}(Ph-COOH)$_5$ (CPC), C_{60}(Ph-COOH)$_5$Fc (CPCFe)[19,32] and contorted hexabenzocoronene (HBC) derivative (Figure 1) were synthesized according to the reported procedure. Silicon dioxide substrates were cleaned by soaking them into CH_2Cl_2 at room temperature for 15 min followed by 20 min in a 1:1:5 = NH_4OH : 30 % H_2O_2 : DI H_2O at 70 °C. Immediately after rinsing in DI H_2O and drying in a steam of N_2 gas, the samples were immersed in a 2 v/v % solution of 3-aminopropyltriethoxysilane (APTES) in ethanol for 25 min at room temperature. Post bake at 120 °C for 5 min gave the monolayer of APTES. The APTES covered samples were then immersed in 0.1 mM solution of CPC (or CPCFe) in THF for 24 hours (30 min for CPCFe) at room temperature. After the monolayer assembly, the samples were soaked in clean THF for 30 min at room temperature for washing out the unbound molecules.

To verify the monolayers, UV-vis spectroscopy was performed using a single-beam Agilent 8453 spectrometer with a modified sample holder. The monolayer was formed on ultrathin quartz flats to reduce background contributions. X-ray reflectivity measurements were performed at the National Synchrotron Light Source on beamline X22A using an X-ray beam of 32 KeV and 15 μm vertical and 1 mm horizontal beam size. The X-ray reflectivity data were fitted using a box based model having discrete layers corresponding to the Si substrate, native oxide layer, the APTES layer and C_{60}. The parameters for fitting have been adjusted with a Marquardt-Levenberg least square routine. Since the scattering length density (SLD) contrast between the APTES layer and the C_{60} material is low, to avoid the interdependence of the fitting parameters during the fitting procedure, the parameters corresponding to the APTES layer have been obtained from a separate sample without C_{60}

and then fixed in the subsequent fit.[33] XPS experiments were performed with a Kratos AXIS-Ultra Spectrometer equipped with a monochromatic Al source operated at 255 watts. The pass energy was set to 160 eV for survey spectrum and 20 eV for high resolution scan of N1s. IR spectroscopy was performed by using a N_2-purged Nicolet IR spectrometer with a mercury cadmium tellurium (MCT) detector. Spectra were obtained by using a GATR (Harrick Inc.) total reflectance accessory equipped with a hemispherical germanium crystal.

A monolayer of CPC was formed on an amine-modified silicon oxide surface. First, a monolayer of 3-aminopropyltriethoxysilane (APTES) was formed on a silicon oxide surface[34-37], then, the substrate was immersed into a 0.1 mM solution of CPC in THF at room temperature for 24 hours without any coupling reagent. The coverage on the surface was calculated to be 0.42 molecules/nm^2 from the absorption cross section (5.3×10^{-16} cm^2/molecules in THF solution.) This value is in good agreement with the calculated value for tightly packed molecules standing upright to the surface (0.45 molecules/nm^2, Figure 2-2). A monolayer of CPCFe (coverage = 0.50 molecules/nm^2) was obtained in the same way except that the substrate was immersed in the CPCFe solution for 30 minutes; this was to avoid the formation of multilayer of CPCFe. AFM images showed that the monolayers were uniform (Figure 2-3, 2-4). Without using an amine-modified surface, the immersion gave only islands of the molecules rather than uniform layers.

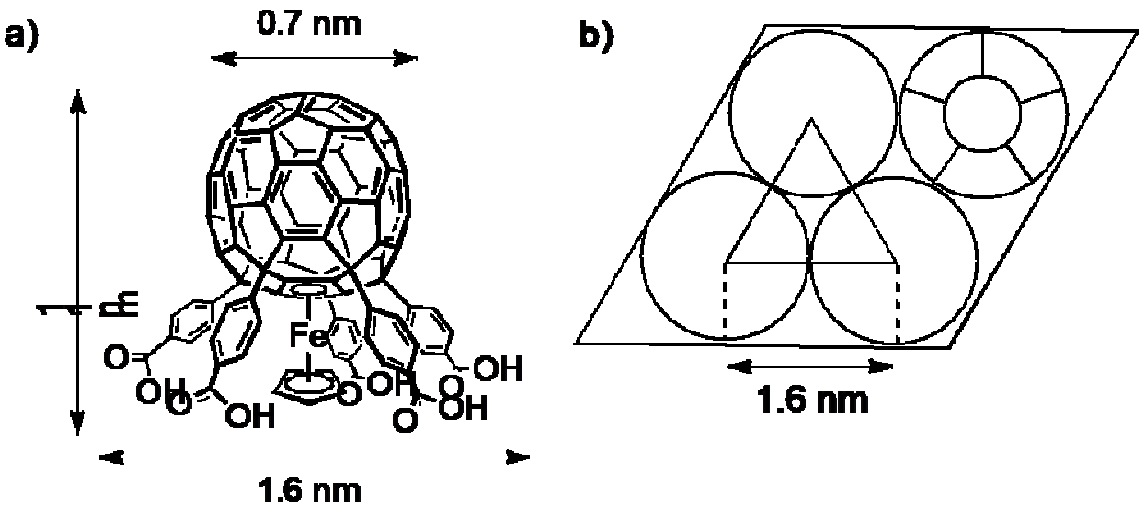

Figure 2-2 Size information of CPC and CPCFe molecules. (a) Molecular size of the CPCFe molecule according to the X-ray crystallography. (b) Ideal packing of CPC and CPCFe monolayer on a surface which corresponds to 0.45 molecules/nm^2.

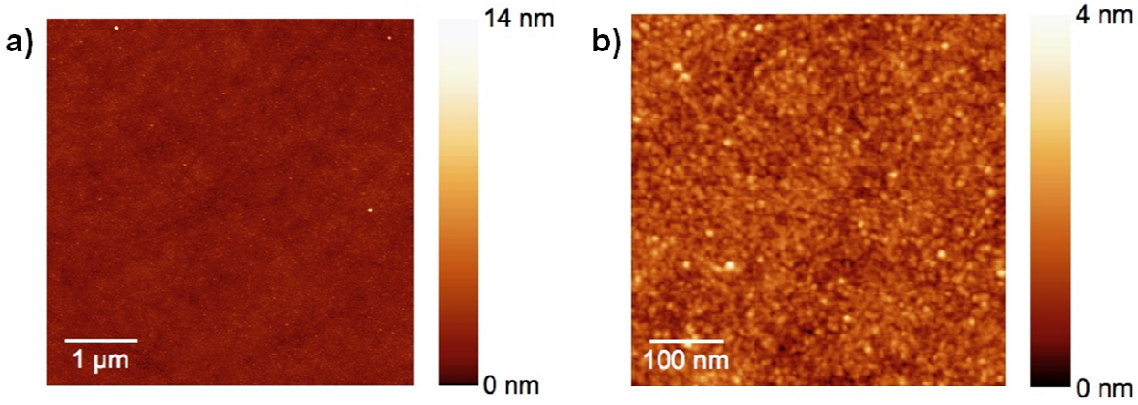

Figure 2-3 AFM height image of CPC monolayer. RMS roughness = 0.49 nm, average height = 1.64 nm. (a) 5 x 5 mm image, and (b) 500 x 500 nm image.

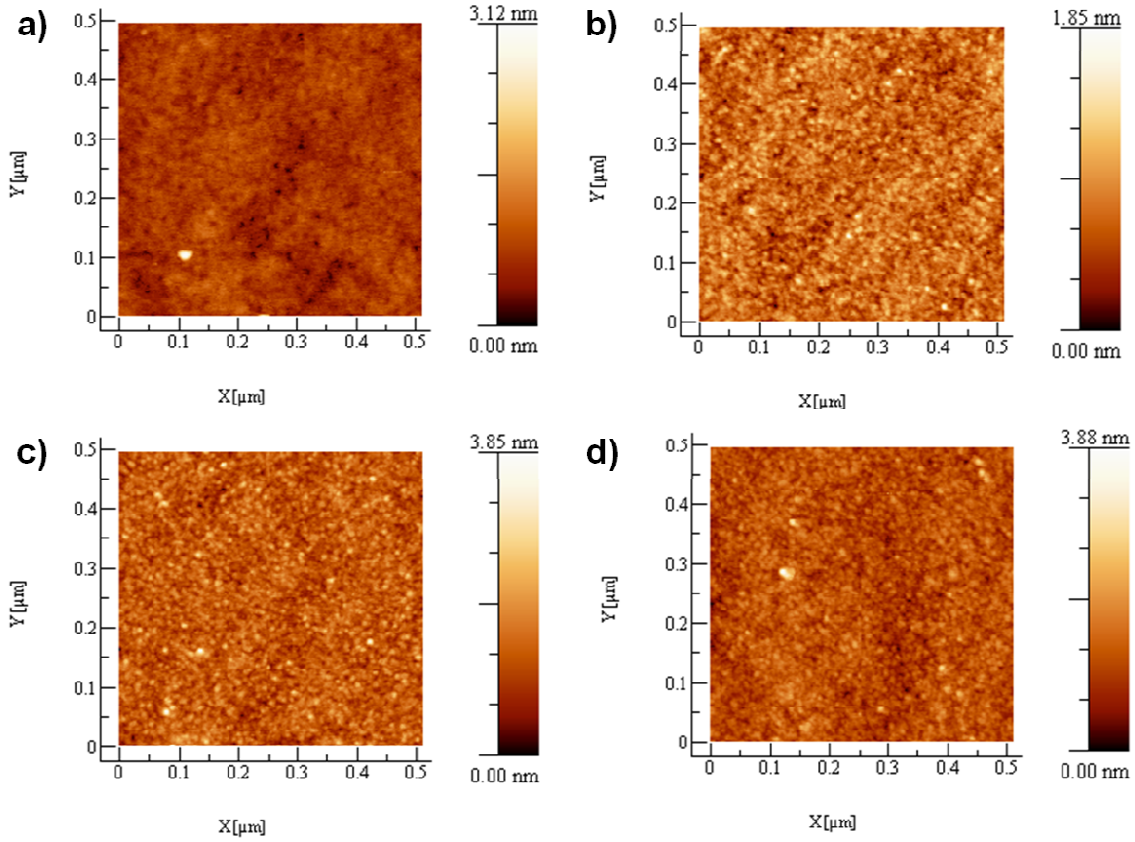

Figure 2-4 AFM images of (a) SiO_2 surface, (b) APTES monolayer, (c) CPC monolayer, and (d) CPCFe monolayer.

Structural analysis of the monolayer was performed using synchrotron X-ray reflectivity, XPS, IR and UV-vis spectroscopy. From synchrotron X-ray reflectivity, information about the thickness, electron density distribution and roughness of the monolayers was obtained. Figure 2-5 (a) shows the reflectivity data corresponding to the layer of CPC together with the fit. The fit was calculated based on a box model having discrete layers corresponding to the Si substrate, native oxide, the APTES layer and the CPC. The parameters corresponding to the APTES layer were obtained from a separate sample lacking CPC and were then fixed in the subsequent fit.[33] The corresponding scattering

length density (SLD) as a function of the film depth is shown in Figure 2-5 (b). This analysis gave thicknesses of 10.9±0.2 Å for CPC and 12.9±0.2 Å for CPCFe (Table 2-1). These numbers agree quite well with the size of the molecules and indicate the formation of a single monolayer. Surface roughness of the monolayer is 5.0±0.2 Å for CPC and 4.9±0.3 Å for CPCFe, and these values are in good agreement with the result of AFM (Figure 2-4).

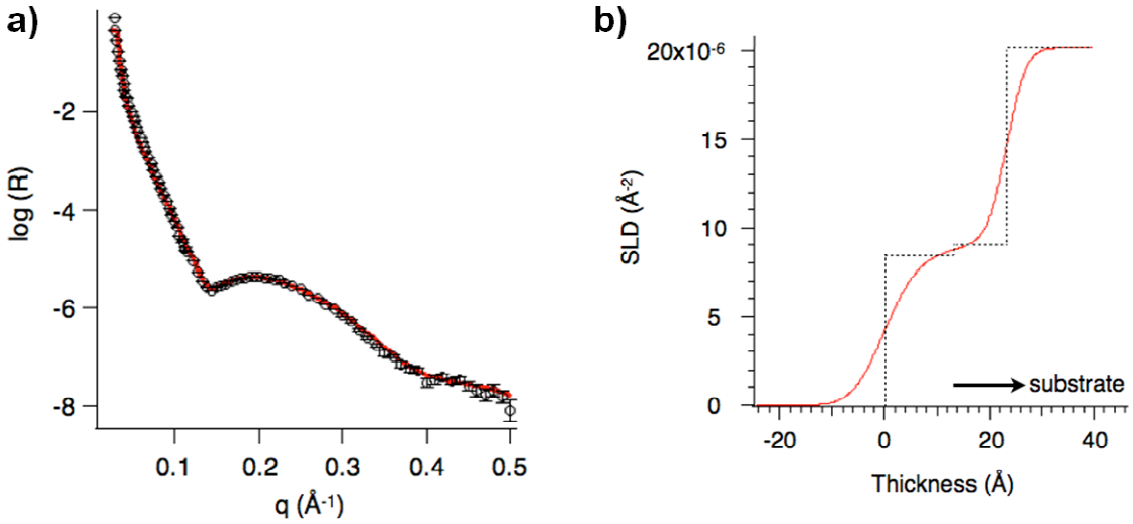

Figure 2-5 (a) X-ray reflectivity curve corresponding to CPC molecule (black open circles) along the plot of the data fit (solid red line). (b) Electron density profile (red) obtained from the model along with box diagram (dashed black) illustrating thickness and electron density with roughness equal to zero.

Table 2-1 X-ray model parameters corresponding to CPC and CPCFe molecule

Layer	Thickness (Å)	SLD ($x10^{-6}$ $Å^{-2}$)	Roughness (Å)
CPC	12.9±0.2	8.1±0.2	5.0±0.2
CPCFe	10.9±0.2	8.2±0.3	4.9±0.3
APS[a]	10.5± 0.13	9.2±0.4	4.7±0.3
SiO_2	21	20.1	3.0±0.5
Si		20.1	2.1±0.7

[a] Calculated standard deviation are from the sample without the top C_{60} based layer

The XPS spectrum shows that hydrogen bonding is involved in the monolayer formation. Figure 2-6 (a) is an XPS spectrum of N1s (escape angle 0 °) of an APTES monolayer in the absence of CPC; there are two peaks which can be assigned to $–NH_2$ (400.1 eV) and $–NH_3^+$ (401.9 eV) in a ratio of 81:19. This is consistent with the previous report.[37] After the CPC monolayer is formed the ratio of $–NH_2$ and $–NH_3^+$ peaks became 67:33 (Figure 2-6 (b)) which implies the formation of a salt between the compound CPC and APTES monolayer. XPS spectrum of CPCFe monolayer gave essentially the same result (Figure 2-6(c)). In addition, the ratio of Fe and C (Fe/C = 1.3 x 10^{-2}) decreased when the spectrum was taken with the escape angle of 75 ° (Fe/C = 7.4 x 10^{-3}) which in turn suggest the upright orientation of CPCFe on the surface.

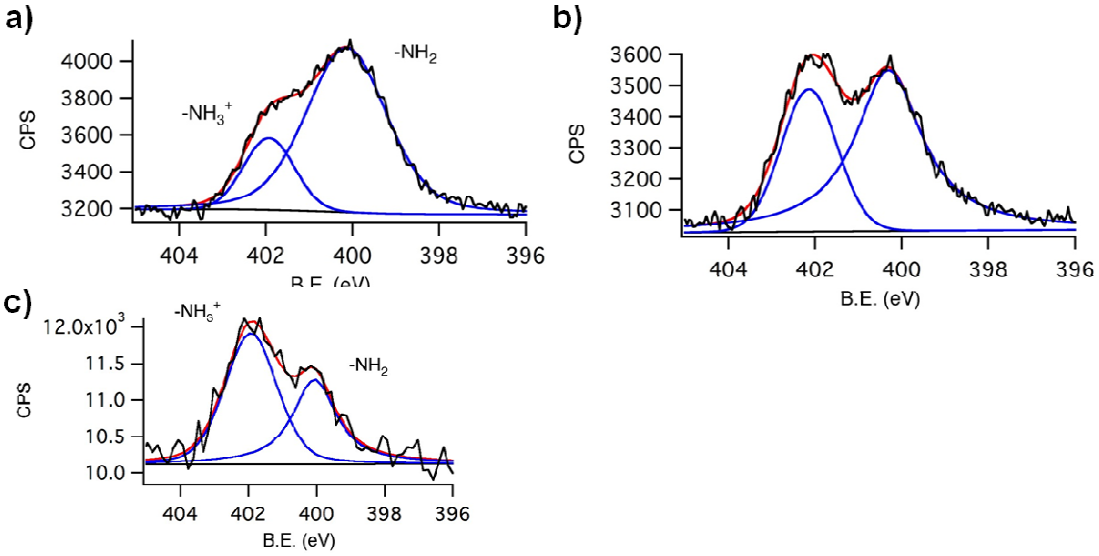

Figure 2-6 XPS spectrum for N1s region taken at the escape angle of 0 º. (a) APTES monolayer, (b) APTES monolayer with CPC monolayer, and (c) APTES monolayer with CPCFe monolayer.

Infrared spectroscopy yielded further chemical information about the interface of CPC monolayer and APTES. The C=O stretch of pure CPC (1701 cm^{-1}, Figure 2-7 (a)) disappeared in the spectrum of the monolayer (Figure 2-7 (b)). Instead, asymmetric and symmetric stretching modes of carboxylate CO_2^- (1608, 1396 cm^{-1} respectively) became predominant, which suggests that CPC is attached to the amine surface through hydrogen bonding. The differential spectrum in which the amine surface spectrum was subtracted from the monolayer spectrum, showed a small amount of C=O stretch remaining (Figure 2-9 (a)). This might be attributed to a residual amount of the carboxylic acids that are not hydrogen bonded to the APTES, or to an occasional molecule that is sitting in alternative orientation (lying on the side or standing upside down). Even so, the major resonances are CO_2^- stretches,

which suggest the predominant upright orientation for CPC. The monolayer spectrum of CPCFe is essentially the same (Figure 2-8, 2-9 (b)).

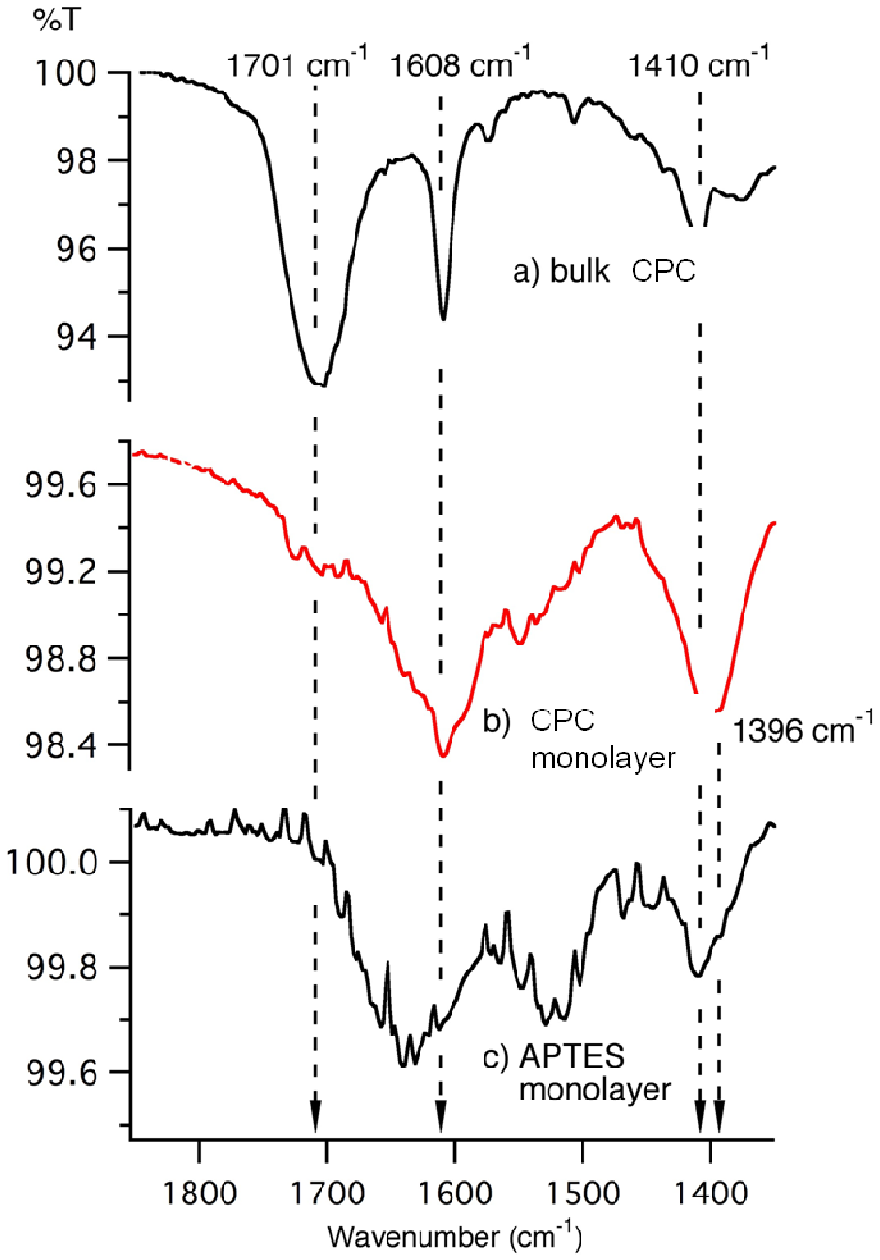

Figure 2-7 Carbonyl region of the IR spectrum of the (a) bulk CPC, (b) CPC monolayer on APTES monolayer, and (c) APTES monolayer.

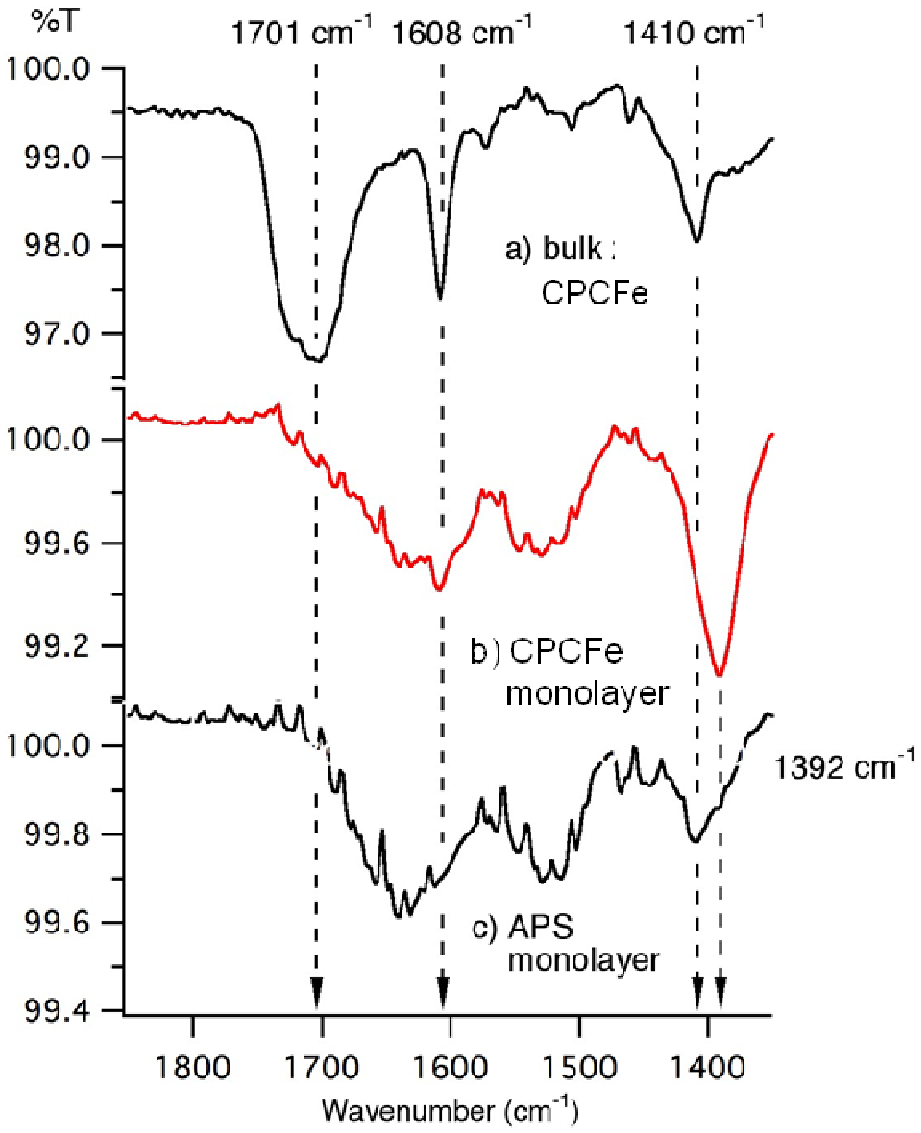

Figure 2-8 Carbonyl region of the IR spectrum of the (a) bulk CPCFe, (b) CPCFe monolayer on APTES monolayer, and (c) APTES monolayer.

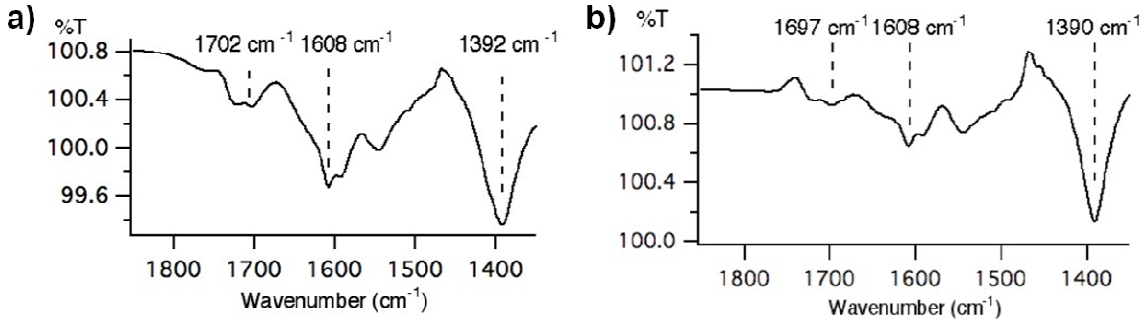

Figure 2-9 Differential IR spectrum of (a) CPC monolayer and (b) CPCFe monolayer subtracted with the spectrum of APTES monolayer.

Monolayers of both CPC and CPCFe are very stable; the UV-vis spectrum did not show significant change over several weeks under air or more than 15 hours under argon at 300 °C. Compared with the monolayer of C_{60} pentabiphenyl derivative ($C_{60}(C_6H_4C_6H_4$-$COOH)_5Me$) on gold,[15] the coverage 0.42 molecules/nm^2 for CPC monolayer and 0.50 molecules/nm^2 for CPCFe monolayer is quite reasonable (0.40 molecules/nm^2 for pentabiphenyl derivative). It is interesting to note that the pentabiphenyl derivative stands upright on bare gold surface without any adhesion layer under in situ STM conditions. To explore the utility of these monolayers, we will show examples of both n-type and p-type transistors using the monolayers as a functionalized insulating layer.

2.3 Device Fabrication and Characterization

The field-effect transistor devices were fabricated with bottom-contact geometry. A highly n-type doped (<0.005 cm) Si wafer with a 300 nm thermally grown silicon dioxide surface was used for electrical measurements. The wafer was cleaned with 70:30 = H_2SO_4: 30% H_2O_2 (Caution: This is called a piranha solution and is an extremely dangerous oxidizing

agent. The solution should be handled with care using appropriate shielding.) for 1 hour at 100 °C. Then, source and drain electrodes (5 nm Cr followed by 30 nm Au) were vacuum-deposited through a shadow mask. The resulting channel was (W, L) = (115 μm, 10 μm) for C_{60} transistors and (W, L) = (2 mm, 85 μm) for HBC transistors. The monolayer of CPC and CPCFe were formed according to the procedure described earlier. C_{60} transistors were then fabricated by thermal evaporation of 50 nm C_{60} on to the substrate at 1.5–1.7 Å/s at $<10^{-6}$ Torr. HBC transistors were fabricated by spin coating 1 mg/mL solution of tetradodecyloxy HBC in $CHCl_3$ or $(CH_2Cl)_2$ at 1200 rpm for 20 sec. The transistor characterization was carried out at room temperature, in Ar atmosphere (C_{60} transistors) or in an ambient atmosphere (HBC transistors) using an Agilent 4155C semiconductor characterization system and a Karl Suss (PM5) manual probe station. The mobility was calculated according to the reference.[38]

First monolayers of CPC and CPCFe were tested to see their effects on n-type FETs made from C_{60}. Au/Cr electrodes were deposited (5 nm Cr followed by 50 nm Au) through a shadow mask by thermal evaporation onto a silicon wafer that has a 300 nm oxide layer as an insulator, then the monolayer of either CPC or CPCFe was assembled on top of this. The channel length was 10 μm and the electrode width was 115 μm. C_{60} was then thermally evaporated onto the substrate (1.5–1.7 Å/s at $<10^{-6}$ Torr, C_{60} layer thickness: 50 nm). (As a reference, C_{60} was also evaporated on a bare silicon oxide substrate.) The measurement was carried out in a glove box without exposing the device to air.

2-4 Device performance

The output of the resulting transistor is shown in Figure 2-10 (b). With CPC monolayer, the mobility was = 0.02 cm^2/Vs, which is quite typical for C_{60} FETs.[7] With CPCFe monolayer the mobility was increased to 0.04 cm^2/Vs, which is twice as high as the value of CPC monolayer devices. The difference is attributable to the ferrocene moiety: since C_{60} is an electron acceptor and ferrocene is an electron donor, carrier generation is more efficient in the presence of ferrocene than in its absence. Compared to the mobility of a normal C_{60} transistor sample (on bare silicon wafer), 0.01 cm^2/Vs, both C_{60} transistors with CPC and CPCFe showed higher current, which can be the result of shielding the surface hydroxyl group and higher crystalline packing of C_{60} on the C_{60} monolayers. The threshold voltage was -34 V in the case of CPC devices and -22 V for CPCFe devices. This is a large shift from the typical value, which is >0 V. An aligned dipole layer generated by the salt of amine and carboxylic acid at the interface of CPC (or CPCFe) and APTES monolayer could be responsible for the shift of the threshold voltage.[39,40]

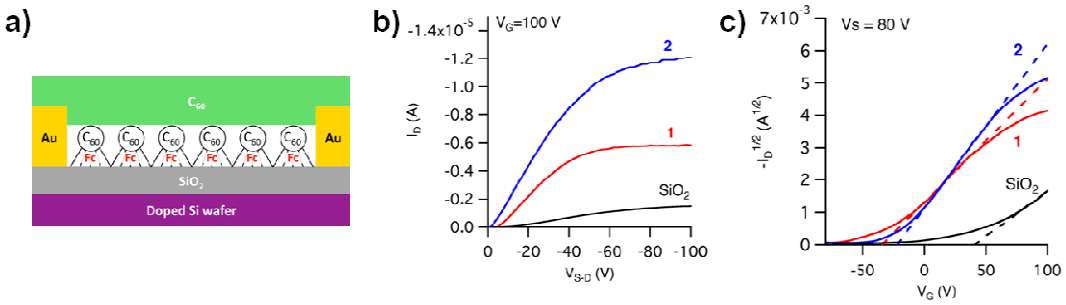

Figure 2-10 (a) Schematic illustration of a FET fabricated for C_{60} transistors. Fc: ferrocene. (b) Transistor output for C_{60} transistors with the monolayer of CPC(1), CPCFe(2), and bare SiO_2 surface. (c) Transconductance: the dotted lines are a fit of the linear portion of the data points. The source-drain voltage $V_{S\text{-}D}$ was held at 80 V.

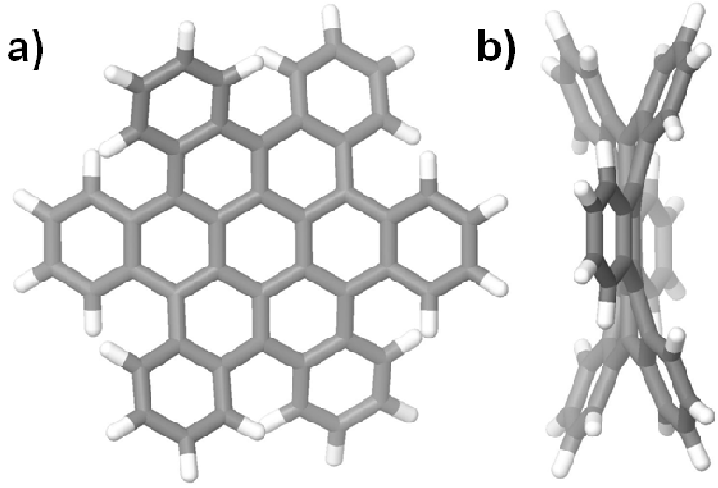

Figure 2-11 Structure of contorted hexabenzocoronene: (a) front view, (b) side view.

Recently, we reported that the contorted hexabenzocoronene (HBC), shows good performance in spuncoat OFETs.[31] The effect of monolayers of CPC and CPCFe in the FETs using HBC was investigated. Beneficial intermolecular interactions can be expected in

these pairings, not only because C_{60} is an electron acceptor and HBC is a donor, but also because their shapes, a ball and a socket respectively, are complementary (Figure 2-11). [41]

The device was fabricated as follows. Au/Cr electrodes were evaporated (5 nm Cr followed by 50 nm Au) through a shadow mask onto the silicon wafer which has 300 nm oxide layer as an insulator. The channel was 85 μm long and 2 mm wide. Then the solution of 3 was spuncoat onto the SAMs of CPC or CPCFe.

The transistor output is shown in Figure 2-10. When the measurement was carried out in the dark, two devices showed similar characteristics (dotted lines); however, when the measurement was carried out in the ambient light, we found an interesting change: the transistor incorporating CPC had higher current than the one with CPCFe. The light–dark current ratio (I_D(light)/I_D(dark)) at V_{S-D} = -100 V was 14 for the former and 3 for the latter. We measured a similar OFET that used an acetic acid layer[42] instead of CPC (or CPCFe). Although it had negligible current either with or without light, the light–dark current ratio at V_{S-D} = -100 V was 2.5, which is similar to the FET with the monolayer of CPCFe. Thus the behavior of the monolayer/HBC devices can be explained by the photo-induced charge transfer between C_{60} moiety of the monolayer and the HBC.[29,43] The lower current with the monolayer of CPCFe could be attributed to the electron-donating ferrocene. Charge transfer from HBC might be suppressed by ferrocene which leads to ineffective channel formation by light.

In summary, we have demonstrated the formation of uniform monolayers of CPC and CPCFe on silicon oxide surfaces with a straightforward method that involves dipping the amino-terminated surface into the solution of the C_{60} derivatives. This does not require any covalent modification of C_{60} on the surface, which could potentially result in a nonuniform

modification of the C_{60} molecules resulting in a surface of a nonuniform electronic structure. The monolayer could be used for the surface modification of the insulating layer of OFETs. When C_{60} was used as a semiconducting layer in an OFET, the mobility when CPC was used was 0.02 cm^2/Vs. This value doubles in the presence of CPCFe monolayer, indicating the efficient channel formation by electron donating ferrocene moiety. A more surprising fact is the generation of photocurrent in the presence of contorted HBC. Both the donor–acceptor interaction and the geometrical ball–socket interaction apparently play important roles in the photocurrent generation.[41]

Experimental Section

2.1. Material preparation

The C_{60} derivatives and contorted hexabenzocoronene derivative were synthesized according to the reported procedure. Quartz flats for UV-vis spectroscopy were purchased from NSG Precision Cells Inc. Silicon wafers for AFM, X-ray reflectivity, X-ray photoelectron spectroscopy, ATR-IR, FET fabrication were Process Specialities Inc. High purity C_{60} (>99.9%, sublimed) was purchased from Bucky USA.

2.2. Monolayer formation of CPC and CPCFe

Silicon oxide surface was cleaned by soaking them into CH_2Cl_2 at room temperature for 15 min followed by 20 min in a 1:1:5 = NH_4OH : 30% H_2O_2 : DI H_2O at 70 °C. Immediately after rinsed in DI H_2O and dried in a steam of N_2 gas, the samples were immersed in a 2 v/v % solution of 3-aminopropyltriethoxysilane (APS) in ethanol for 25 min at room temperature. Post bake at 120 °C for 5 min gave the monolayer of APS. APS covered samples were then immersed in 0.1mM solution of CPC (or CPCFe) in THF for 24 h (30 min for CPCFe) at room temperature. After the monolayer assembly, the samples were soaked in clean THF for 30 min at room temperature for washing out the surface unbouned molecule.

2.3. Surface characterization

UV-vis spectroscopy was performed by a single-beam Agilent 8453 spectrometer with a modified sample holder. The monolayer was formed on ultrathin quartz flats (NSG Precisions Cells) to reduce background contributions. X-ray reflectivity measurements were

performed at the National Synchrotron Light Source on beamline X22A using an X-ray beam of 32KeV and 15 μm vertical and 1mm horizontal beam. The fit was calculated based on a box model having discrete layers corresponding to the Si substrate, native oxide, the APS layer and C_{60}. The parameters for fitting have been adjusted with a Marquardt-Levenberg least square routine. Since the scattering length density (SLD) contrast between the APS layer and the C_{60} material is low, to avoid the interdependence of the fitting parameters during the fitting procedure, the parameters corresponding to the APS layer have been obtained from a separate sample without C_{60} and then fixed in the subsequent fit. XPS experiments were performed with a Kratos AXIS-Ultra Spectrometer equipped with a monochromatic Al source operated at 255 watts. The pass energy was set to 160 eV for survey spectrun and 20 eV for high resolution scan of N1s. IR spectroscopy was performed by using a N_2-purged Nicolet IR spectrometer with a mercury cadmium tellurium (MCT) detector. Spectra were obtained by using a GATR (Harrick Inc.) total reflectance accessory equipped with a hemispherical germanium crystal.

2.4. FET device fabrication

Bottom-contact geometry was used in all the transistor devices. A Highly *n*-type doped (<0.005 Ωcm) Si wafer with 300 nm thermally grown silicon oxide surface was used for electrical measurements. The wafer was cleaned with 70:30 = H_2SO_4:DI H_2O (piranha) for 1 h at 100 °C. Then, source and drain electrodes (30 nm Au followed by 5 nm Cr) were vacuum-deposited through a shadow mask. Resulting channel was (W, L) = (115 μm, 10 μm) for C_{60} transistors and (W, L) = (2 mm, 85 μm) for HBC transistors. The monolayer of CPC and CPCFe were formed according to the procedure described earlier. C_{60} transistors were

then fabricated by thermal evaporation of C_{60} on to the substrate at 1.5–1.7 Å/s at $<10^{-6}$ Torr for 50 nm. HBC transistors were fabricated by spin coating 1 mg/mL solution of HBC in $CHCl_3$ or $(CH_2Cl)_2$ at 1200 rpm for 20 sec. The transistor characterization was carried out at room temperature, in Ar atmosphere (C_{60} transistors) or in the ambient atmosphere (HBC transistors) in the ambient atmosphere using Agilent 4155C semiconductor characterization system and a Karl Suss (PM5) manual probestation.

References for Chapter 2

[1] Kroto, H. W.; Heath, J. R.; O'Brien, S. C.; Curl, R. F.; Smalley, R. E. *Nature* **1985**, *318*, 162–163.

[2] Mirikin, C. A.; Caldwell, W. B. *Tetrahedron* **1996**, *52*, 5113–5130.

[3] Konishi, T.; Ikeda, A.; Shinkai, S. *Tetrahedron* **2005**, *61*, 4881–4899.

[4] Gludi, D. M.; Illescas, B. M.; Atienza, C. M.; Wielopolski, M.; Martin, N. *Chem. Soc. Rev.* **2009**, *38*, 1587–1597.

[5] Sariciftci, N. S.; Smilowitz, L.; Heeger, A. J.; Wudl, F. *Science* **1992**, *258*, 1474–1476.

[6] Yu, G.; Gao, J.; Hummelen, J. C.; Wudl, F.; Heeger, A. J. *Science* **1995**, *270*, 1789–1791.

[7] Haddon, R. C.; Perel, A. S.; Morris, R. C.; Palstra, T. T. M.; Hebard, A. F.; Fleming, R. M. *Appl. Phys. Lett.* **1995**, *67*, 121–123.

[8] Priebe, G.; Pietzak, B.; Könenkamp, R. *Appl. Phys. Lett.* **1997**, *71*, 2160–2162.

[9] Anthopoulos, T. D.; Ramil, A. M.; Sitter, H.; Cölle, M.; Leeuw, D. M. *Appl. Phys. Lett.* **2006**, *89*, 213504/1–213504/3.

[10] Love, J. C.; Estroff, L. A.; Kriebel, J. K.; Nuzzo, R. G.; Whitesides, G. M. *Chem. Rev.* **2005**, *105*, 1103–1169.

[11] Ma, H.; Yip, H.-L., Huang, F.; Jen, A. K.-Y. *Adv. Funct. Mater.* **2010**, *20*, 1371–1388.

[12] Shi, X.; Caldwell, W. B.; Chen, K.; Mirkin, C. A. *J. Am. Chem. Soc.* **1994**, *116*, 11598–11599.

[13] Imahori, H.; Norieda, H.; Yamada, H.; Nishimura, Y.; Yamazaki, I.; Sakata, Y.; Fukuzumi, S. *J. Am. Chem. Soc.* **2001**, *123*, 100–110.

[14] Shirai, Y.; Cheng, L.; Chen, B.; Tour, J. M. *J. Am. Chem. Soc.* **2006**, *128*, 13479–13489.

[15] Chen, T.; Pan, G.–B.; Yan, H.–J.; Wan, L.–J.; Matsuo, Y.; Nakamura, E. *J. Phys. Chem. C* **2010**, *114*, 3170–3174.

[16] Matsuo, Y.; Lacher, S.; Sakamoto, A.; Matsuo, K.; Nakamura, E. *J. Phys. Chem. C* **2010**, *14*, 17741–17752.

[17] Yamada, H.; Imahori, H.; Nishimura, Y.; Yamazaki, I.; Ahn, T. K.; Kim, S. K.; Kim, D.; Fukuzumi, S. *J. Am. Chem. Soc.* **2003**, *125*, 9129–9139.

[18] Cho, Y.–J.; Ahn, T. K.; Song, H.; Kim, K. S.; Lee, C. Y.; Seo, W. S.; Lee, K.; Kim, S. K.; Kim, D.; Park, J. T. *J. Am. Chem. Soc.* **2005**, *127*, 2380–2381.

[19] Matsuo, Y.; Kanaizuka, K.; Matsuo, K.; Zhong, Y.–W.; Nakae, T.; Nakamura, E. *J. Am. Chem. Soc.* **2008**, *130*, 5016–5017.

[20] Matsuo, Y.; Ichiki, T.; Radhakrishnan S. G.; Guldi, D. M.; Nakamura, E. *J. Am. CHem. Soc.* **2010**, *132*, 6342–6348.

[21] Bonifazi, D.; Enger, O.; Diederich, F. *Chem. Soc. Rev.* **2007**, *36*, 390–414.

[22] Chupa, J. A.; Xu, S.; Fischetti, R.F.; Strongin, R. M.; McCauley Jr., J. P.; Smith, III, A. B.; Blasie, J. K. *J. Am. Chem. Soc*. **1993**, *115*, 4383-4384.

[23] Tsukruk, V. V. *Langmuir* **1994**, *10*, 996–999.

[24] Tsukruk, V. V. *Langmuir* **1996**, *12*, 3905–3911.

[25] Lee, H.; Jeon, C. *Synth. Met.* **1997**, *86*, 2297–2298.

[26] Wei, T.–X.; Zhai, J.; Ge, J.–H.; Gan, L.–B.; Huang, C.–H.; Luo, G.–B.; Ying, L.–M.; Liu, T.–T.; Zhao, X.–S. *Appl. Surf. Sci.* **1999**, *151*, 153–158.

[27] Wei, T.–X.; Zhai, J.; Ge, J.; Gan, L.–B.; Huang, C.–H.; Luo, G.–B.; Ying, L.–M. *J. ColloidInterface Sci.* **2000**, *222*, 262–264.

[28] Gulino, A.; Bazzano, S.; Condorelli, G. G.; Giuffrida, S.; Mineo, P.; Satriano, C.; Scamporrino, E.; Ventimiglia, G.; Vitalini, D.; Fragalà, I. *Chem. Mater*. **2005**, *17*, 1079-1084.

[29] Park, B.; Paoprasert, P.; In, I.; Zwickey, J.; Colavita, P. E.; Hamers, R. J.; Gopalan, P.; Evans, P. G. *Adv. Mater*. **2007**, *19*, 4353–4357.

[30] Guérin, D.; Lenfant, S.; Godey, S.; Vuillaume, D. *J. Mater. Chem.* **2010**, *20*, 2680–2690.

[31] Xiao, S.; Myers, M.; Miao, Q.; Sanaur, S.; Pang, K.; Steigerwald, M. L.; Nuckolls, C. *Angew. Chem. Int. Ed.* **2005**, *44*, 7390–7394.

[32] Zhong Y.–W.; Matsuo, Y.; Nakamura, E. *Org. Lett.* **2006**, *8*, 1463–1466.

[33] Gao, Y.; Tang, Z.; Watkins, E.; Majewski, J.; Wang, H.–L. *Langmuir* **2005**, *21*, 1416–1423.

[34] I. Haller, *J. Am. Chem. Soc.* **1978**, *100*, 8050–8055.

[35] E.T. Vandenberg, L. Bertilsson, B. Liedberg, K. Uvdal, R. Erlandsson, H. Elwing, I. Lundström, *J. Colloid Interface Sci.* **1991**, *147*, 103–118.

[36] P. A. Heiney, K. Grüneberg, J. Fang, *Langmuir* **2000**, *16*, 2651–2657.

[37] A.E. Hooper, D. Werho, T. Hopson, O. Palmer, *Surf. Interface Anal.* **2001**, *31*, 809-814.

[38] Miao, Q.; Lefenfeld, M.; Nguyen, T. Q.; Siegrist, T.; Kloc, C.; Nuckolls, C. *Adv. Mater.* **2005,** 17, 407–412.

[39] Kobayashi, S.; Nishikawa, T.; Takenobu, T.; Mori, S.; Shimoda, T.; Mitani, T.; Shimotani, H.; Yoshimoto, N.; Ogawa, S.; Iwasa, Y. *Nature Mater.* **2004**, 3, 317–322.

[40] Takeya, J.; Nishikawa, T.; Takenobu, T.; Kobayashi, S.; Iwasa, Y.; Mitani, T.; Goldmann, C.; Krellner, C.; Batlogg, B. *Appl. Phys. Lett.* **2004**, 85, 5078–5080.

[41] Tremblay, N. J.; Gorodetsky, A. A.; Cox, M. P.; Schiros, T.; Kim, B.; Steiner, R.; Bullard, Z.; Sattler, A.; So, W.-Y.; Itoh, Y.; Toney, M. F.; Ogasawara, H.; Ramirez, A. P.; Kymissis, I.; Steigerwald, M. L.; Nuckolls, C. *ChemPhysChem* **2010**, 11, 799–803.

[42] Acetic acid layer was prepared using the same method as for the preparation of the monolayer of **1** and **2**. The concentration of the acetic acid solution was five times higher than the solution of **1** and **2** in order to make the concentration of the "acid" (number of the –COOH group) same. We consider that the acetic acid makes a salt on APTES surface which prevents from evaporation.

[43] Yamamoto, Y.; Zhang, G.; Jin, W.; Fukushima, T.; Ishii, N.; Saeki, A.; Seki, S.; Tagawa, S.; Minari, T.; Tsukagoshi, K.; Aida, T. *Proc. Nat. Acad. Sci. USA* **2009**, *106*, 21051–21056.

Chapter 3

RUBRENE FIELD-EFFECT TRANSISTORS USING CVD GROWN GRAPHENE AS ELECTRODES*

* Part of this chapter was reproduced with permission from *Advanced Materials*:
"Inking Elastomeric Stamps with Micro-Patterned, Single Layer Graphene to Creat High-Performance OFETs" by Seok Ju Kang, Bumjung Kim, Keun Soo Kim, Yue Zhao, Zheyuan Chen, Gwan Hyoung Lee, James Hone, Philip Kim, and Colin Nuckolls. © 2011 John Wiley and Sons.

3.1 Background

Two dimensional (2D) graphene has promise in many electronic and optoelectronic device applications because of its useful properties such as low resistance,[1,2] high flexibility,[3] high mechanical stability[4] and high transparency to visible light.[5-8] There are two current methods to process graphene electrodes over the large scale: graphitization of single crystal SiC[9,10] and chemical vapor deposition (CVD) on metal films.[3,11,12] Specifically for electrodes, CVD-grown graphene has promise in producing electrodes because the films have low resistance, high optical transmittance and flexibility.[3,12] Several reports have demonstrated organic thin film transistors (OTFT) using CVD-grown graphene as source and drain electrodes.[13-18] However, in these studies, fabricating reliable junctions while maintaining clean interface between the channel and electrodes remains as a challenge. Although photolithography with subsequent dry and wet etching processes has been shown to work with graphene, these processes are not compatible with organic devices due to the harsh patterning conditions. Recently, Kim et al.[3] successfully transferred multilayer graphene grown on patterned Ni, using PDMS transfer printing over large areas.

The key feature of this study is that it reveals a method to pattern and transfer CVD-grown graphene using an elastomeric stamp, a method that also enables patterned graphene to be transferred to any substrate without conventional lithography. Using a variation on this method, we have transferred CVD-grown single layer graphene to Si/SiO_2 substrates in a pattern defined by the geometry of the PDMS stamp. As a demonstration of one application of the technique, we formed high-performance bottom contact organic field effect transistors with graphene as the source and drain electrodes. The devices have high hole mobility exceeding 10 cm^2/Vs, high on-off current ratios larger than 10^7 and a low threshold voltage for switching.

3.2 Large-scale Growth of Graphene using Chemical Vapor Deposition Method

Single-layer graphene sheet was prepared by thermal chemical vapor deposition (CVD) method.[3,12] 0.05 inch thick copper foil (99 %) was used as a catalyst. The copper foil was placed in a tube furnace and the system was purged with argon gas (200 SCCM, ultra high purity, 99.999 %) with roughing pumping to have 1.2 Torr of pressure. Then the furnace was rapidly heated up to 1000 °C. When the furnace reached 1000 °C, hydrogen gas (10 SCCM) was added to reduce the copper foil surface for 10 minutes. (64 mTorr) After the annealing step, the growth was started by adding methane gas (170 SCCM, 1.7 Torr) for 18 min. When the growth was done, the system was purged with argon gas and slowly cooled down to room temperature.

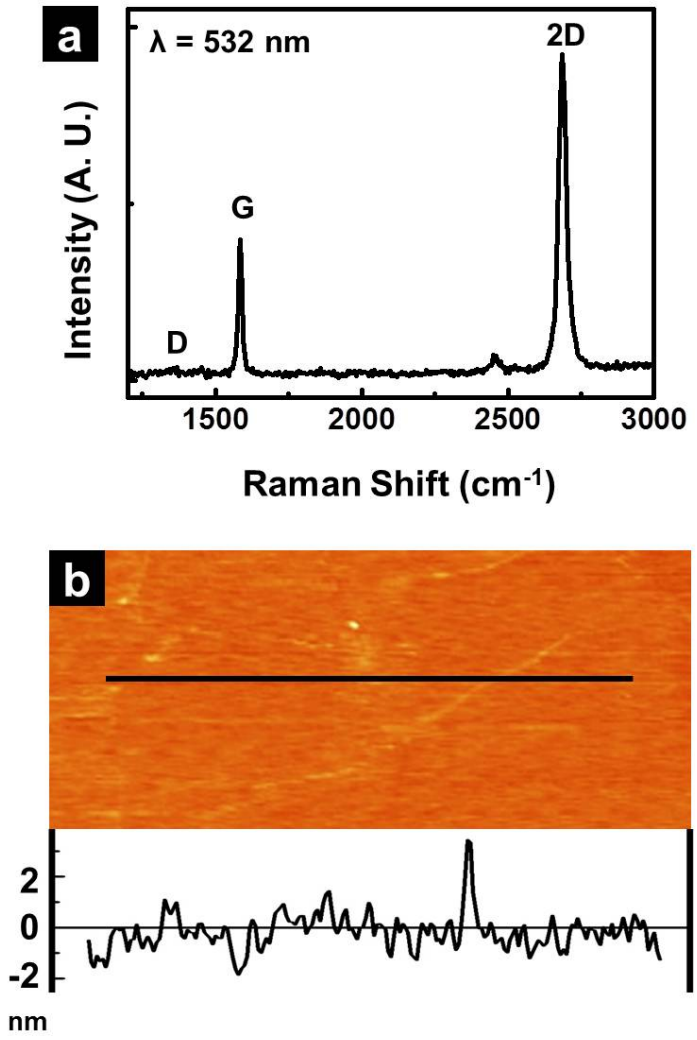

Figure 3-1 (a) Raman spectra of transferred SLG pattern with absorptions at 1538 and 2680 cm^{-1} were observed using a 514 nm laser source, as indicated with G and 2D, respectively. (b) AFM image in height contrast of transferred graphene on SiO_2 layer.

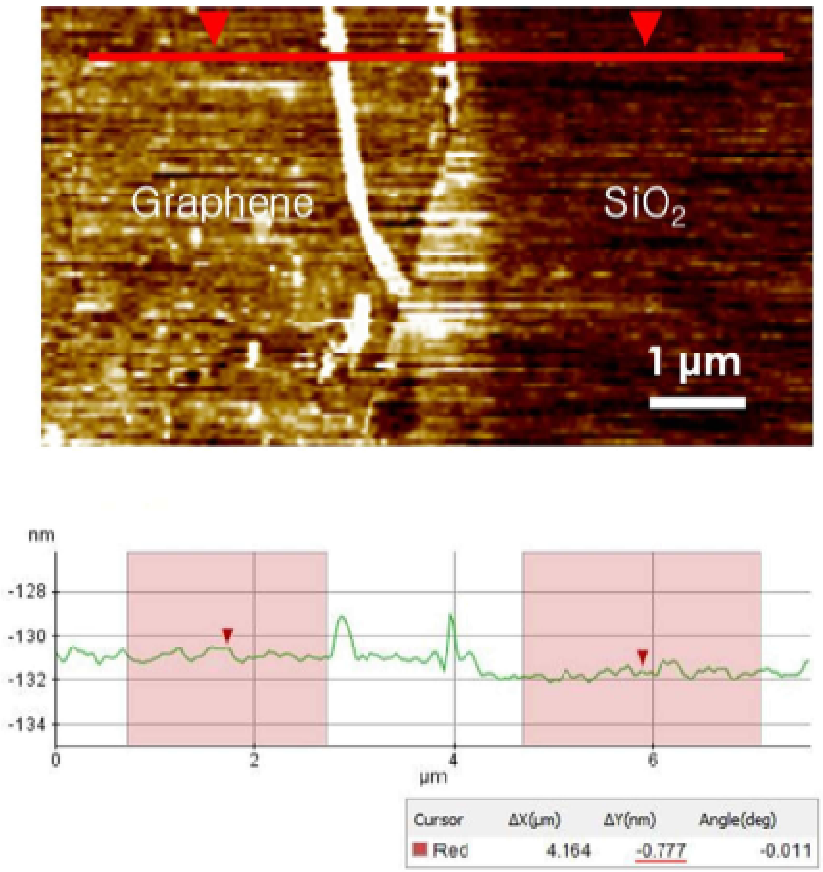

Figure 3-2 An AFM image of transferred SLG on SiO_2 layer (top) The height profile of SLG along the red line (down).

Raman scattering was used to investigate the properties of the SLG after it was transferred to a SiO_2 substrate (Figure 3-1(a)). The single Lorentzian line shape of 2D peak indicates that the film is single layer graphene.[3] The G and 2D bands had a reasonable ratio, 2.3, and the band positions were also well aligned at 1583 cm^{-1} and 2680 cm^{-1}. Negligible D band intensity indicates a low level of defects in the transferred SLG pattern. Furthermore, the cross-sectional profile of the single layer graphene obtained from AFM images of the transferred pattern shows an average height of approximately 0.7 nm. This height in the AFM measurement indicates that there is a single layer of graphene on a SiO_2 layer, consistent with

a previous report (Figure 3-2).[19] The transferred SLG showed that the sheet resistance of SLG is about ~1.8k Ω/sq, as measured by a four-point probe method.[20] An AFM micrograph of a transferred SLG film on SiO_2 is shown in Figure 3-1(b), showing that the films are somewhat rough and buckled during the transfer process. Further process improvements will likely produce material with lower sheet resistance. Despite the relatively high sheet resistance, these patterned graphene layers can be used as source and drain contacts in organic FETs

3.3 Graphene Transfer and Patterning Technique and Characterization

Organic field-effect transistors (OFET) with 2D single layer graphene (SLG) as source and drain electrodes were fabricated by the procedure schematically shown in Figure 3-3. An elastomeric PDMS mold was prepared by curing a PDMS precursor (Sylgard 184, Dow Corning Corp) on a pre-patterned silicon master. We used a mixture of PDMS precursor and curing agent (10 : 1 by weight) that had been degassed under vacuum. The pre-patterned photoresist masters were prepared by standard photolithography, and the surface of a master was modified with 1H,1H,2H,2H- perfluorodecyltrichlorosilane (Aldrich) SAM in the vacuum before casting the PDMS precursor on the master. The graphene grown Cu foil was then laminated onto a micron scale patterned PDMS stamp. The Cu foil was removed by etching the copper with an $(NH_4)_2S_2O_8$ (ammonium persulfate) solution (0.1 M in DI water), and the PDMS stamp was thoroughly rinsed with DI water. Once the copper is etched, the raised features in the PDMS are “inked” with SLG that has the same pattern as the PDMS stamp. The patterned SLG was then transferred to the target substrates by pressing and gently removing the PDMS mold.

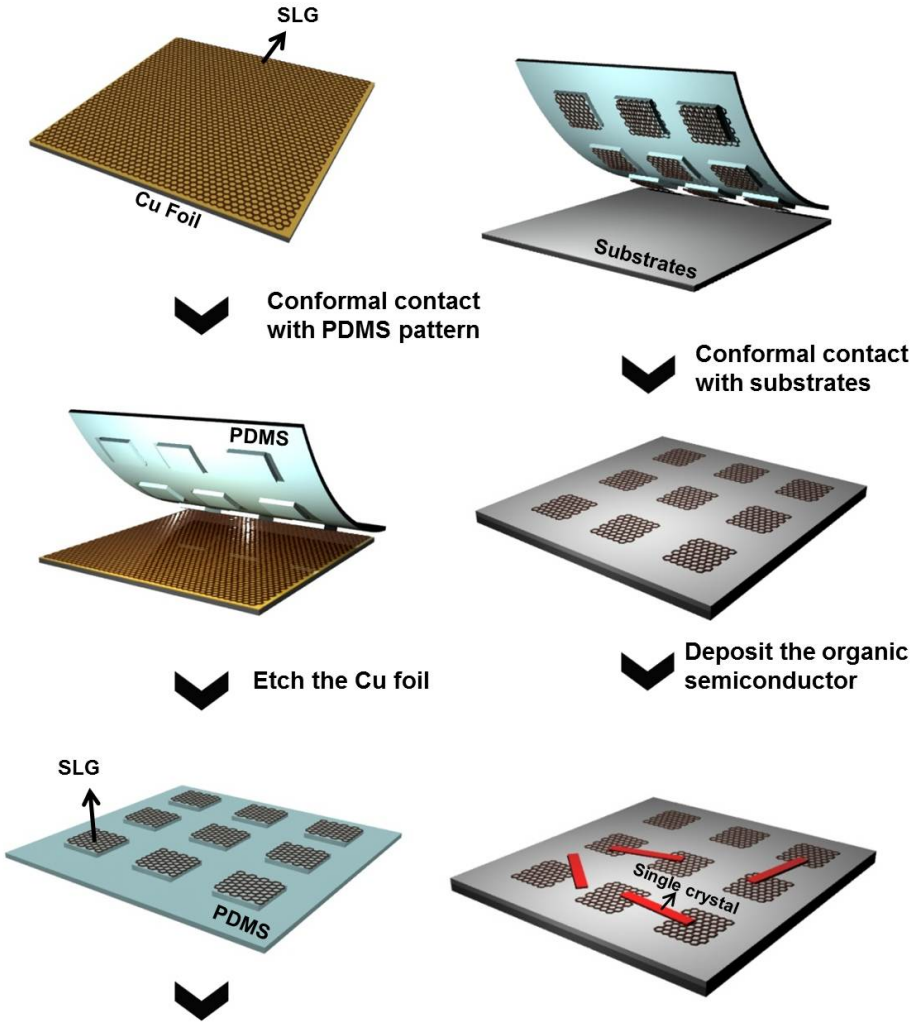

Figure 3-3 Schematics of the fabrication procedure for transferred micro patterned SLG electrode based organic field effect transistor using rubrene single crystal semi-conductor.

Microscale features from SLG graphene on SiO_2 layer are visualized in Figure 3-4(a). SLG patterns on SiO_2 substrates are apparent over large area and have feature size of 20 μm and 1000 μm in width and length, respectively. Our stamping method for SLG electrodes is very reliable for large area pattern transfer onto SiO_2 layer. The SLG transfer from PDMS to an acceptor substrate is governed by the difference of work of adhesion in surface tension of

each layer. In order to transfer SLG, the adhesion force for the SLG and the target substrate should be higher than that of the PDMS/SLG interface. (Table 3-1)[21-23] Using this technique, we are able to transfer SLG onto a variety of substrates. Figure 3-4(b) shows the result of transferring SLG onto a poly(4-vinylphenol) (PVP) substrate. The organic dielectric is not compatible with conventional photolithography methods due to the harsh conditions.[18] Figure 3-4(b) shows well-defined SLG pattern arrays on PVP on a flexible PET substrate. The inset in Figure 3-4(b) shows a photograph of graphene/PVP/patterned graphene structure devices on a transparent PET substrate.

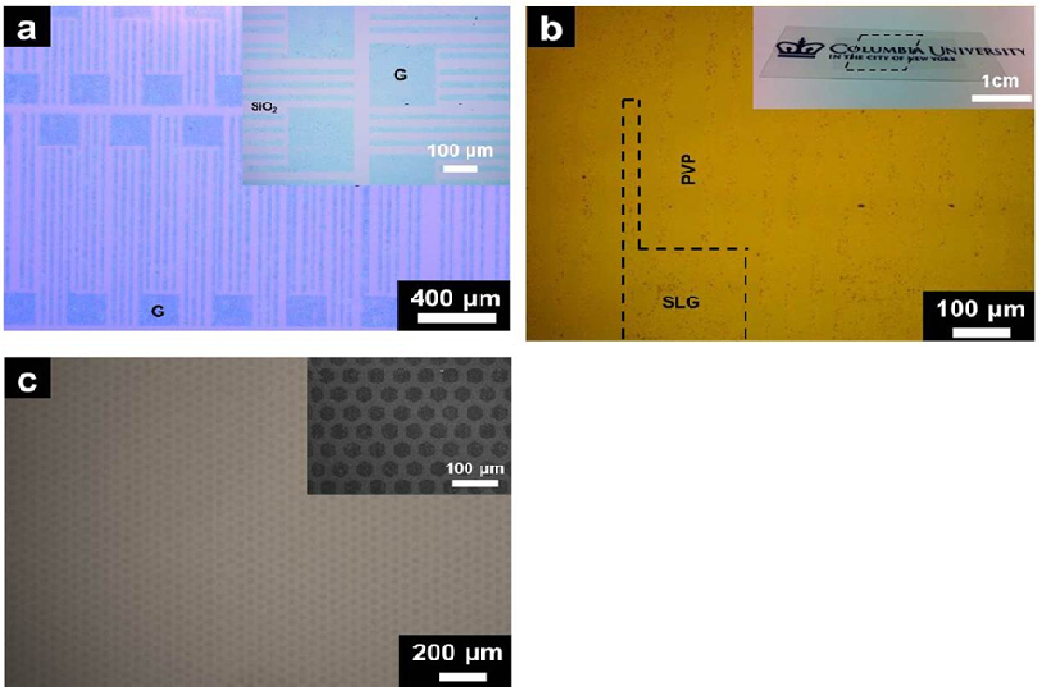

Figure 3-4 (a) An optical microscope image of patterned SLG electrodes on SiO_2 layer fabricated by stamping method. The inset of (a) is a magnified optical microscope image of micro patterned SLG. (b) An optical microscope image of SLG patterned electrode fabricated on PET/graphene/PVP layer. The inset shows a photograph of the transparent PET/graphene/PVP/patterned graphene structure. (c) An SEM image of the hexagonal arrays of SLG electrodes micropatterned onto a SiO_2 substrate. The inset of (c) displays a magnified image of SLG having 20 µm edge length arrayed with *p6mm* symmetry.

It is easy with this method to transfer a variety of shapes that could be useful in electronic devices. Using this method we were able to create 20 µm hexagonal tiles of SLG arrayed into p6mm symmetry shown in Figure 3-4(c). We applied another PDMS mold with 20 µm periodic lines arranged in a p2mm symmetry. These are patterned over a large area and can easily produce features on the ~ 10 µm scale. (Figure 3-5).

Substrate	γ ($\gamma^p + \gamma^d$)/mJ m^{-2}	γ^d/mJ m^{-2}	γ^p/mJ m^{-2}	$W_{SLG/Subs}$/mJ m^{-2}
SLG[a]	27.3	19.1	8.2	N/A
PDMS[a]	19.8	19	0.8	41
SiO_2[b]	71.9	21.9	50	68.9
Al_2O_3[b]	29	27.7	1.2	49.5
PVP[a]	36.6	26.1	10.5	62.5
Au[b]	46.8	34.9	11.9	68.8

[a] Calculated from the geometric mean equation based on the contact angle measurement of water and ethylene glycol.

[b] Obtained from literature [20]

Table 3-1 Work of adhesion value chart

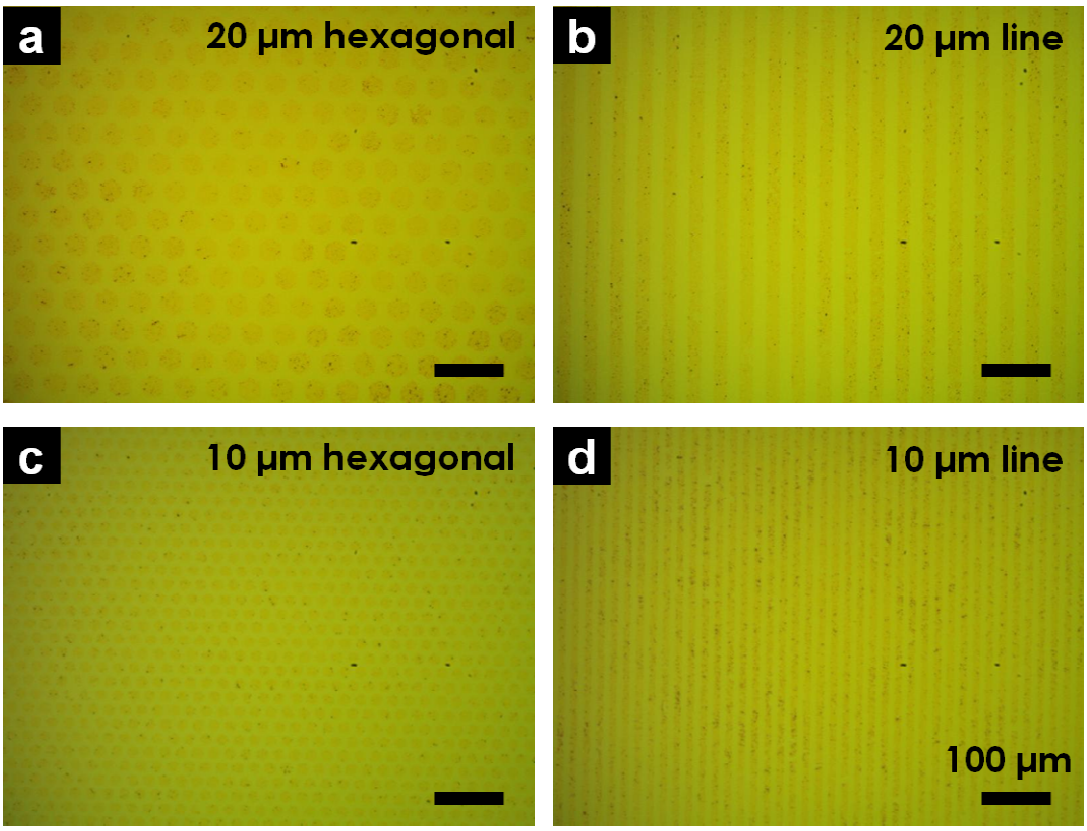

Figure 3-5 Optical microscope images of SLG micropatterned on SiO_2 layer by pre-patterned PDMS mold with different size over lager area.

3.4 Single Crystal Growth of Rubrene: Growth System and Conditions

Rubrene single crystal was grown in physical vapor transport furnace.[24] 2 mg of sublimed rubrene powder (> 99.5%) was weighed and placed in a hot zone of the furnace (330 °C). For a direct growth, the substrate with patterned SLG was placed in a crystallization zone (280 °C). Crystals were grown on a glass wall of tube and then transferred to a substrate for the crystal transfer FETs. 50 SCCM of ultra high purity argon gas (99.999 %) was used as a purging gas as well as a carrier gas. After 5 minutes of pre-purging, the system was heated to 330 °C. The reaction was performed for 2 minutes and the system was cooled down to the room temperature. After the growth, FET devices with directly grown rubrene crystals were ready for measurement. For a transfer method, thin crystals (less than 200 μm thick) were transferred to the substrate with patterned SLG using static force.

3.5 Field-Effect Transistor Fabrication and Characterization

Two different device fabrication processes were employed to demonstrate bottom contact transistor with our patterned SLG electrodes. First, the rubrene crystals were directly grown onto the SLG in the PVD furnace. The transfer curves clearly exhibit current modulation of the p-type rubrene active layer at negative gate voltage. The output characteristics of the OFET also show excellent saturation behavior beyond a drain-source voltage, V_{DS}, of -50 V with gate field modulated step (Figure 3-6). The sublinear onset of the output curve indicates good charge injection from SLG electrode to the rubrene single crystal. The field-effect mobility is calculated from the slope of a plot of the square root of the drain current (I_{DS}) versus gate voltage (V_G) in the saturation regime (Figure 3-6(b)). To calculate the mobility we use $I_{DS}=(W/2L)C_i\mu(V_G-V_T)^2$, where W and L are the width and length of

channel and C_i, μ, and V_T correspond to the capacitance per unit area of the gate insulator, the field-effect mobility and threshold voltage, respectively. The field-effect hole mobility is ~2 cm^2/Vs and the on/off ratio is approximately 10^7 with a threshold voltage of +3 V.

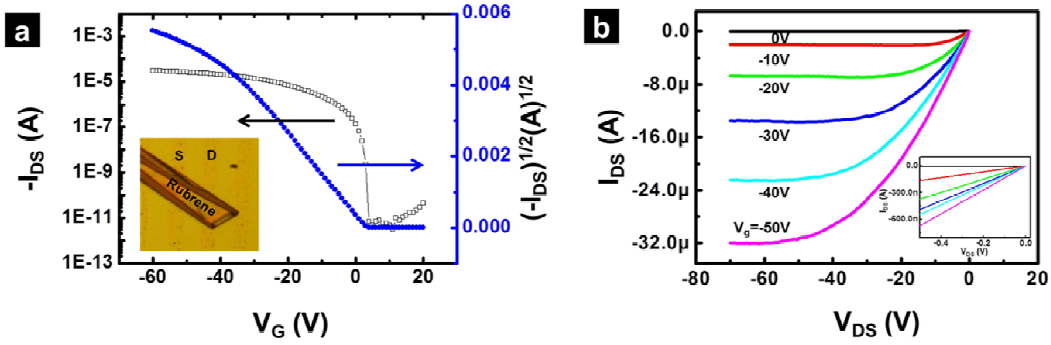

Figure 3-6 (a) Transfer and (b) output curves of a representative OFET with directly grown rubrene crystal on patterned SLG electrodes. The inset of (a) shows optical microscope image of top view of device. The inset of (b) shows the low bias range of the main panel.

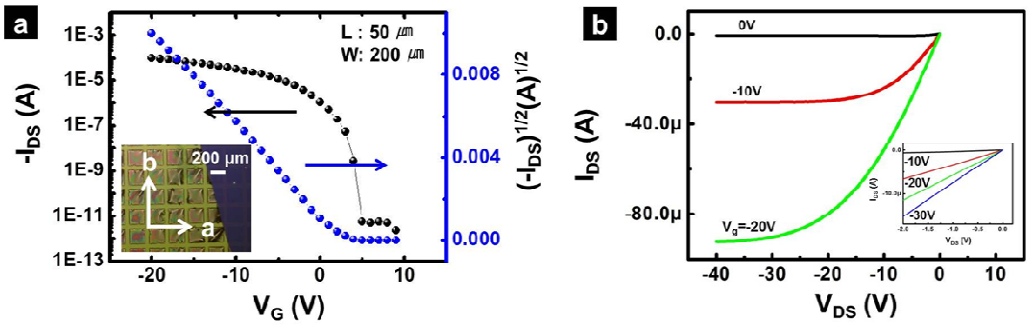

Figure 3-7 (a) I_D-V_G transfer curve of OFET with patterned SLG using transferred method. The inset optical microscope image shows top view of an OFET with single crystal rubrene on patterned SLG source and drain electrodes, (b) Output characteristics of SLG electrodes based OFET. The gate voltage carried from 0 V to -30 V with a step of -10 V. The inset shows the low bias voltage zoom in of the main panel.

We were also able to transfer thin (ca. 100 nm) rubrene single crystal onto the SLG pattern using static force between SiO_2 and organic crystal. The transfer technique not only improved the positioning of rubrene crystal but also exhibited higher performance transistor characteristics. Using this technique we were able to measure the statistical distribution in electrical characteristics along the crystallographic a and b axes (Figure 3-7 inset). The average field-effect mobility values from 36 devices were calculated to be 6.0 and 3.8 cm^2/Vs for different rubrene crystal direction b and a, respectively (Figure 3-8). The on/off current ratio of > 5 x 10^6 was obtained at normal ambient condition. The on/off ratio is higher than this value but unfortunately the current is too high in many devices to be measured in the on-state with our present measurement apparatus. We extract a subthreshold swing value, *S*, of ~ 0.2 to 0.5 V/decade from the equation given by $S=d(V_g)/d(logI_{SD})$ and a normalized subthreshold swing, $S_i = SC_i$, of 2.5 to 5 $VnF/decade^{-1}cm^{-2}$. Furthermore, the highest mobility of transferred rubrene transistor shows a mobility of 10.3 cm^2/Vs with approximately 10^7 of on/off ratio, as shown Figure 3-7(a). Figure 3-7(b) shows that the low Schottky barrier between SLG and rubrene crystal give rise to excellent output curves showing up to 100 μA at a gate voltage of -20 V.

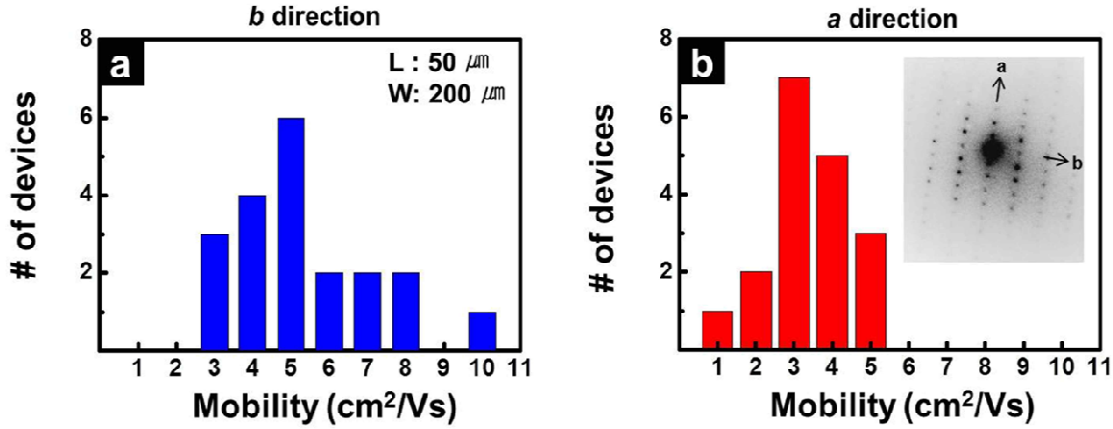

Figure 3-8 Histograms of laminated rubrene crystal on the SLG electrodes along the *b* and *a* axes. Inset of (b) shows SAED of the rubrene single crystal confirmed the orientation of the *ab* crystalline plane.

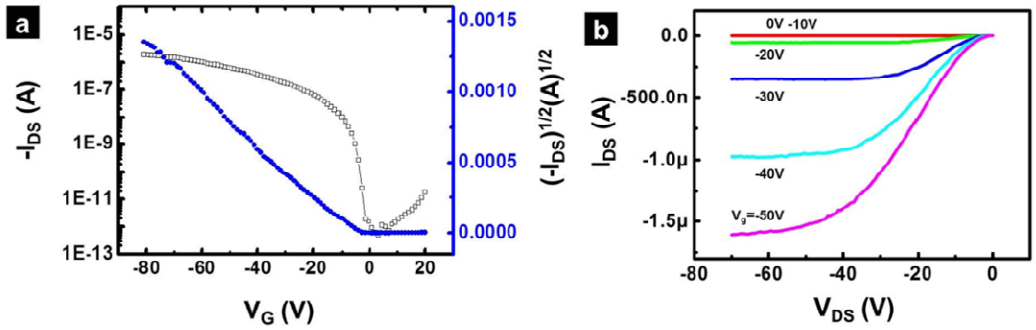

Figure 3-9 (a) Transfer characteristics of a top-contact OFET with Au source and drain, exhibiting charge-carrier mobility of 0.7 cm^2/Vs calculated in the saturated regime. (b) Output characteristics.

For comparison, we also fabricated an OFET with gold as source and drain contacts. We first tried to deposit the gold electrodes and grow the rubrene crystals as we did for the SLG contacts. We were unable to produce any devices that functioned appreciably well. We speculate that when using bottom contact gold, which is relatively thick, the crystals do not

grow well. We were able to create top contact devices, which showed much diminished properties such as higher threshold voltage and lower mobility (Figure 3-9). The degradation in properties may result from poor contact resistance between the metal electrode and the rubrene crystal.

The SLG electrodes have the dual advantage that they encourage the crystal growth of organic materials and have a work-function similar to the organic materials. Moreover the extreme thinness of the graphene electrodes allows single crystals to have homogeneous contacts. Unlike the commonly used carbon paste electrodes for organic materials,[25,26] here graphene provides us more controllability in the electrode fabrication process and better carrier injection efficiency owing to the work function adjustment.[27]

In summary, we have demonstrated a new method to pattern SLG using a PDMS mold. The micro patterning allowed us to use SLG as electrodes for OFETs. With single crystalline rubrene as an active channel, the devices exhibited excellent p-type characteristics, with on/off current ratio of ~10^7, field effect mobility of ~10 cm^2/Vs and low threshold voltage of +5 V. It is also clear that using this approach all three electrodes could be applied to a transparent substrate through lamination. Furthermore, our approach is also compatible with reel-to-reel processing of organic devices such as organic light emitting diodes, capacitors, and heterostructured materials for photovoltaics.

Experimental Section

3.1. Large-scale graphene growth

Single-layer graphene sheet was prepared by thermal chemical vapor deposition (CVD) method. 0.05 inch thick copper foil (99 %) was used as a catalyst. The copper foil was placed in a tube furnace and the system was purged with argon gas (200 SCCM, ultra high purity, 99.999 %) with roughing pumping to have 1.2 Torr of pressure. Then the furnace was rapidly heated up to 1000 °C. When the furnace reached 1000 °C, hydrogen gas (10 SCCM) was added to reduce the copper foil surface for 10 minutes. (6.4×10^{-2} Torr) After the annealing step, the growth was started by adding methane gas (170 SCCM, 1.7 Torr) for 18 min. When the growth was done, the system was purged with argon gas and slowly cooled down to room temperature.

3.2. Fabrication of PDMS mold

An elastomeric PDMS mold was fabricated by curing a PDMS precursor (Sylgard 184, Dow Corning Corp) on a pre-patterned silicon master. We used a mixture of PDMS precursor and curing agent (10 : 1 by weight) that had been degassed under vacuum. The pre-patterned photoresist masters were prepared by standard photolithography, and the surface of a master was modified with 1H,1H,2H,2H- perfluorodecyltrichlorosilane (Aldrich) SAM in the vacuum before casting the PDMS precursor on the master.

3.3. Rubrene single-crystal growth using PVD

Rubrene single crystal was grown in physical vapor transport furnace. 2 mg of sublimed rubrene powder (> 99.5%) was weighed and placed in a hot zone of the furnace (330 ˚C). Then, the substrate with patterned SLG was placed in a crystallization zone (280 ˚C). 50 SCCM of ultra high purity argon gas (99.999 %) was used as a purging gas as well as a carrier gas. After 5 minutes of pre-purging, the system was heated to 330 ˚C. The reaction was performed for 2 minutes and the system was cooled down to the room temperature

3.4 FET characterization

OFET transfer and output characteristics were recorded using semiconductor systems in ambient condition at room temperature (Agilent Technologies, HP4284A).

3.5. Microstructure characterization

Optical microscope was used to visualized the patterned SLG using stamping method with an Nikon ME600 instrument. SEM images were obtained with a Hitach-4700 field-emission-gun electron microscope. Atomic force microscopy (AFM) was performed in height contrast by a Digital Instrument NanoScope IIIa.

References for Chapter 3

[1] Novoselov, K. S.; Geim, A. K.; Morozov, S. V.; Jiang, D.; Katsnelson, M. I.; Grigorieva, I. V.; Dubonos, S. V.; Firsov, A. A. *Nature* **2005**, *438*, 197.

[2] Zhang, Y.; Tan, Y.-W.; Stormer, H. L.; Kim, P. *Nature* **2005**, *438*, 201.

[3] Kim, K. S.; Zhao, Y.; Jang, H.; Lee, S. Y.; Kim, J. M.; Kim, K. S.; Ahn, J.-H.; Kim, P.; Choi, J.-Y.; Hong, B. H. *Nature* **2009**, *457*, 706.

[4] Lee, C.; Wei, X.; Kysar, J. W.; Hone, J. *Science* **2008**, *321*, 385.

[5] Watcharotone, S.; Dikin, D. A.; Stankovich, S.; Piner, R.; Jung, I.; Dommett, G. H. B.; Evmenenko, G.; Wu, S. E.; Chen, S. F.; Liu, C. P.; Nguyen, S. T.; Ruoff, R. S. *Nano Lett*. **2007**, *7*, 1888.

[6] Nair, R. R.; Blake, P.; Grigorenko, A. N.; Novoselov, K. S.; Booth, T. J.; Stauber, T.; Peres, N. M. R.; Geim, A. K. *Science* **2008**, *320*, 1308.

[7] Wang, X.; Zhi, L.; Mullen, K. *Nano Lett.* **2008**, *8*, 323.

[8] Li, X.; Zhang, G.; Bai, X.; Sun, X.; Wang, X.; Wang, E.; Dai, H. *Nat. Nanotechnol.* **2008**, *3*, 538.

[9] Berger, C.; Song, Z.; Li, X.; Wu, X.; Brown, N.; Naud, C.; Mayou, D.; Li, T.; Hass, J.; Marchenkov, A. A. N.; Conrad, E. H.; First, P. N.; de Heer, W. A. *Science* **2006**, *312*, 1191.

[10] Emtsev, K. V.; Bostwick, A.; Horn, K.; Jobst, J.; Kellogg, G. L.; Ley, L.; McChesney, J. L.; Ohta, T.; Reshanov, S. A.; Rohrl, J.; Rotenberg, E.; Schmid, A. K.; Waldmann, D.; Weber, H. B.; Seyller, T. *Nat. Mater.* **2009**, *8*, 203.

[11] Reina, A.; Jia, X.; Ho, J.; Nezich, D.; Son, H.; Bulovic, V.; Dresselhaus, M. S.; Kong, J. *Nano Lett.* **2009**, *9*, 30.

[12] Li, X. S.; Cai, W. W.; An, J. H.; Kim, S.; Nah, J.; Yang, D. X.; Piner, R. D.; Velamakanni, A.; Jung, I.; Tutuc, E.; Banerjee, S. K.; Colombo, L.; Ruoff, R. S. *Science* **2009**, *324*, 1312.

[13] Lee, S.; Jo, G.; Kang, S.-J.; Wang, G.; Choe, M.; Park, W.; Kim, D.-Y.; Kahng, Y. H.; Lee, T. *Adv. Mater.* **2011**, *23*, 100.

[14] Liu, W.; Jackson, B. L.; Zhu, J.; Miao, C.-Q.; Chung, C.-H.; Park, Y.-J.; Sun, K.; Woo, J.; Xie, Y.-H. *ACS Nano* **2010**, *4*, 3927.

[15] Jang, S.; Jang, H.; Lee, Y.; Suh, D.; Baik, S.; Hong, B. H.; Ahn, J.-H. *Nanotech.* **2010**, *21*, 425201.

[16] Yu, W. J.; Lee, S. Y.; Chae, S. H.; Perello, D.; Han, G. H.; Yun, M.; Lee, Y. H. *Nano Lett.* **2011**, *11*, 1344.

[17] Zhang, L.; Diao, S.; Nie, Y.; Yan, K.; Liu, N.; Dai, B.; Xie, Q.; Reina, A.; Kong, J.; Liu, Z. *J. Am. Chem. Soc.* **2011**, *133*, 2706.

[18] Lee, W. H.; Park, J.; Sim, S. H.; Jo, S. B.; Kim, K. S.; Hong, B. H.; Cho, K. *Adv. Mater.* **2011**, *23*, 1752.

[19] Lshigami, M.; Chen, J. H.; Cullen, W. G.; Fuhrer, M. S.; Williams, E. D. *Nano Lett.* **2007**, *7*, 1643.

[20] By the method of Van der Pauw using the following equation, $R_s = (\pi/\ln 2)[(R_x + R_y)/2]f$, where R_s, R_x, R_y, and f correspond to the sheet resistance, transverse resistance, longitudinal resistance and ratio of R_y/R_x, respectively. Van der Pauw, L. J. *Philips Tech. ReV.* **1958**, *20*, 220.

[21] Kim, H.; Yoon, B.; Sung, J.; Choi, D.-G.; Park, C. *J. Mater. Chem.* **2008**, *18*, 3489.

[22] Chang, J.; Jung, H. J.; Jeong, H.; Park, Y. J.; Sung, J.; Kang, S. J.; Jung, G. Y.; Sung, M. M.; Park, C. *Org. Electron.* **2011**, *12*, 98.

[23] The work of adhesion at layer 1 and 2 is given by $W_{12} = 4((\gamma_1^d\gamma_2^d/(\gamma_1^d+\gamma_2^d)) + (\gamma_1^p\gamma_2^p/(\gamma_1^p+\gamma_2^p)))$, where γ^p and γ^d correspond to polar and dispersion component of overall surface tension ($\gamma = \gamma^p + \gamma^d$), respectively. The surface tension of SLG was calculated from the geometric-mean method based on the equation followed by $(1+\cos\theta_t)\gamma_t = 2\{(\gamma_t^d\gamma_s^d)^{1/2} + (\gamma_t^p\gamma_s^p)^{1/2}\}$, where θ is the contact angle of a testing liquid on SLG surface. Water and ethylene glycol were used as testing liquids (see supporting information).

[24] Laudise, R. A.; Kloc, C.; Simpkins, P. G.; Siegrist, T. *Journal of Crystal Growth* **1998**, *187*, 449.

[25] Podzorov, V.; Pudalov, V. M.; Gershenson, M. E. *Appl. Phys. Lett.* **2003**, *82*, 1739.

[26] Zeis, R.; Besnard, C.; Siegrist, T.; Schlockermann, C.; Chi, X.; Kloc, C. *Chem. Mater*. **2006**, *18*, 244.

[27] Yu, Y.-J.; Zhao, Y.; Ryu, S.; Brus, L. E.; Kim, K. S.; Kim, P. *Nano Lett.* **2009**, *9*, 3430.

Chapter 4

CRYSTAL MORPHOLOGY STUDY OF DIBENZOTETRATHIENOCORONENE (DBTTC) SINGLE CRYSTALS GROWN ON DIFFERENT SUBSTRATES*

*My contribution on this study was mainly focused on graphene synthesis and crystal growth of DBTTC on graphene. GIXD measurement and analysis were done by Dr. Theanne Schiros.

4.1 Background

Organic single crystal growth has been considered as the best way to study intrinsic electronic properties of organic semiconductor materials.[1-3] Advantaged by highly ordered packing over large area, charge carrier mobility of organic single crystals is comparable to that of polycrystalline silicon semiconductors; the highest intrinsic time-of-flight hole mobility of naphthalene at 4.2 K was found to be 400 cm^2/Vs[4], and pentacene and rubrene single crystal field-effect transistors (FET) showed hole mobility of 20~40 cm^2/Vs in ambient condition.[5-8] However, not many studies have applied organic single crystals in optoelectronic devices such as light emitting diodes (LED) or photovoltaic cells (PVC). Conventional crystal handling techniques only allow one-step attachment of organic single crystals onto substrates; further steps are arduous due to brittleness, excessive thickness for charge transport, and organic solvent-based spincoat disability. Only few studies have been successful to make PVCs with low efficiency.[9,10] Moreover, most crystal packing of organic semiconductors have favorable charge transport along the planar direction, which is disadvantageous for LED or PVCs. These problems necessitate further study on direct growth of organic crystals on substrate; the breakthrough is to control crystal packing orientation, crystal size, uniformity, and thickness.

Recently, large-scale graphene film[11-13] has caught great interest as a transparent electrode attributed by its optical transparency (~98 %),[14] single-atomic thickness, and low resistance.[15,16] Moreover, sp^2-orbitals of graphene enable great compatibility with organic semiconductors which have massively conjugated sp^2-orbitals. Some studies already showed great compatibility of organic thin film with graphene film.[17] However, study of organic crystal growth on graphene film still remains unexplored.

In this study, we report on the vertical growth of organic nanowire crystals of dibenzotetrathienocoronene (DBTTC) on large-scale graphene films. DBTTC has a coronene core, which can possibly have great interaction with graphene. Within the benzocoronene family, DBTTC is particularly remarkable in that it has one-dimensional columnar packing crystal structure, as shown in Figure 4-1, presumably attributed to its sulfur-to-sulfur interlocking interaction as well as its contorted molecular conformation.[18] Moreover, we have previously demonstrated DBTTC to be a promising photovoltaic material due to a controlled heat-induced self-assembly process that produces high surface area donor layers of DBTTC that lead to improved organic heterojunctions.[19] Here, we demonstrate another manifestation of self-assembly and grow vertical DBTTC crystals on graphene with a nanowire structure. We show that both the columnar packing of the pi-stacked DBTTC molecules and the growth axis of the nanowire crystals share the vertical orientation relative to graphene. In the following we present the crystal growth conditions along with the resulting macrostructures and morphologies of DBTTC on graphene using SEM and the molecular scale packing and crystallographic orientation at the ensemble level with Grazing Incidence X-ray Diffraction (GIXD) and at the single fiber level with TEM.

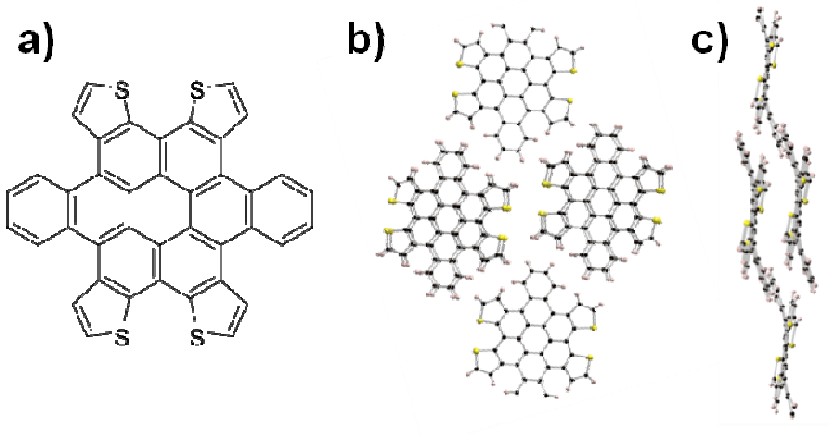

Figure 4-1 Chemical structure (a) and front (b) and side (c) views of the columnar molecular packing of DBTTC.

4.2 Large-scale graphene growth and transfer technique

Pristine, single-layer graphene was prepared by the CVD growth technique performed by Xuesong Li et al.[12] As a pretreatment, copper foil (50 μm thick), used as a catalyst substrate, was placed in a tube furnace and purged with argon gas under vacuum to have constant pressure (1.2 Torr). Then the system was annealed at 1000 °C with flow of ultra high-purity hydrogen gas (6.4 x 10^{-2} Torr) for 10 minutes. Methane gas was added (1.7 Torr) to start the growth for 18 minutes. The system was then slowly cooled down to room temperature.

The graphene film produced was then transferred to a Si substrate with a 300 nm native oxide layer selected to optimize graphene visualization with optical microscopy.[20] Graphene grown copper foil was cut into desirable size (1.5 x 1.5 cm^2) and mounted onto glass substrate with tape. Then 950 PMMA (A5) was spincoated on the graphene grown copper film with 5000 rpm for 60 seconds. Then photoresist (AZ P4330-RS) was

consequently spincoated on the copper film with 5000 rpm for 60 seconds. The spincoated film was baked at 50 °C for 10 minutes, to make sure that the film is dried. This foil was then floated on $FeCl_3$ solution (30% wt). The removal of copper film was checked by the film transparency; if the film turned transparent, copper is all etched by $FeCl_3$ solution. After the etching is finished, the floating film was transferred to water to rinse out some residual copper as well as $FeCl_3$ solution, and the film was finally caught on SiO_2 substrate. The substrate with graphene film was dried under mild heating (~ 40 °C) until water is fully dried. After the film was fully stuck on the substrate, the substrate was dipped in acetone to remove PMMA and photoresist films. To make sure that all the residuals were removed, the samples were annealed at 300 °C under 150 SCCM of argon and 10 SCCM of hydrogen for an hour. The Raman spectrum of the transferred graphene sheet (Figure 4-2) showed ~0.3 G:2D intensity ratio and a narrow 2D peak bandwidth (32 cm^{-1}), indicating single-layer graphene.[21] An almost undetectable D peak verified the high quality of the graphene film, except for a slight upshift of the G peak and 2D peak to 1587 and 2694 cm^{-1}, respectively, possibly due to residual iron chloride from the transfer procedure.

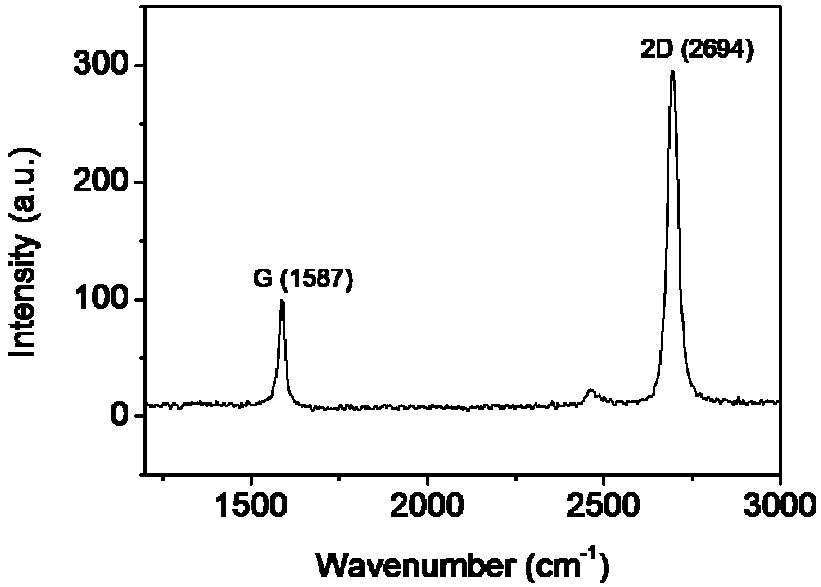

Figure 4-2 Raman spectrum of CVD grown graphene film.

4.3 Crystal growth of dibenzotetrathienocoronene (DBTTC)

Nanocrystals of DBTTC on graphene sheet were grown in a temperature gradient furnace.[22] DBTTC powder was placed at the high temperature zone (330~350 °C), while the graphene–coated substrate was placed in the low temperature zone (139~152 °C). Ultra-high purity argon gas was used as an inert carrier gas and vacuum was applied to keep the pressure constant. Temperature and pressure were varied to probe their effects on crystal size and density; pressure was varied from 0.58 ± 0.01 Torr (100 SCCM of argon) to 1.20 ± 0.01 Torr (300 SCCM of argon), and DBTTC source temperature was varied from 330 to 350 °C. Growth time and the amount of DBTTC were kept constant at 6 hours and 2 mg for reproducibility. (Figure 4-3) To understand growth mechanism, time dependence of crystal growth was also investigated, varying growth time from 2 hours to 6 hours. 45 °-tilted angle SEM images of the grown crystals under these conditions are shown in Figure 4-4.

All the DBTTC crystals grown on CVD grown graphene film formed vertically-oriented nanowires with 50 nm diameter in average. This supports the intuition that the π-π stacking system and molecular conformation of DBTTC are well matched to that of graphene, and that this similarity opens an opportunity for directed crystal growth. Crystal growth time dependence study also showed that only vertically grown crystals survive after 6 hour growth, indicating graphene surface directs crystal growth orientation. (Figure 4-3) To verify this hypothesis, four representative samples are chosen (Figure 4-5) and the structure and molecular packing of the crystals are examined at the ensemble level by Grazing Incidence X-ray Diffraction (GIXD).

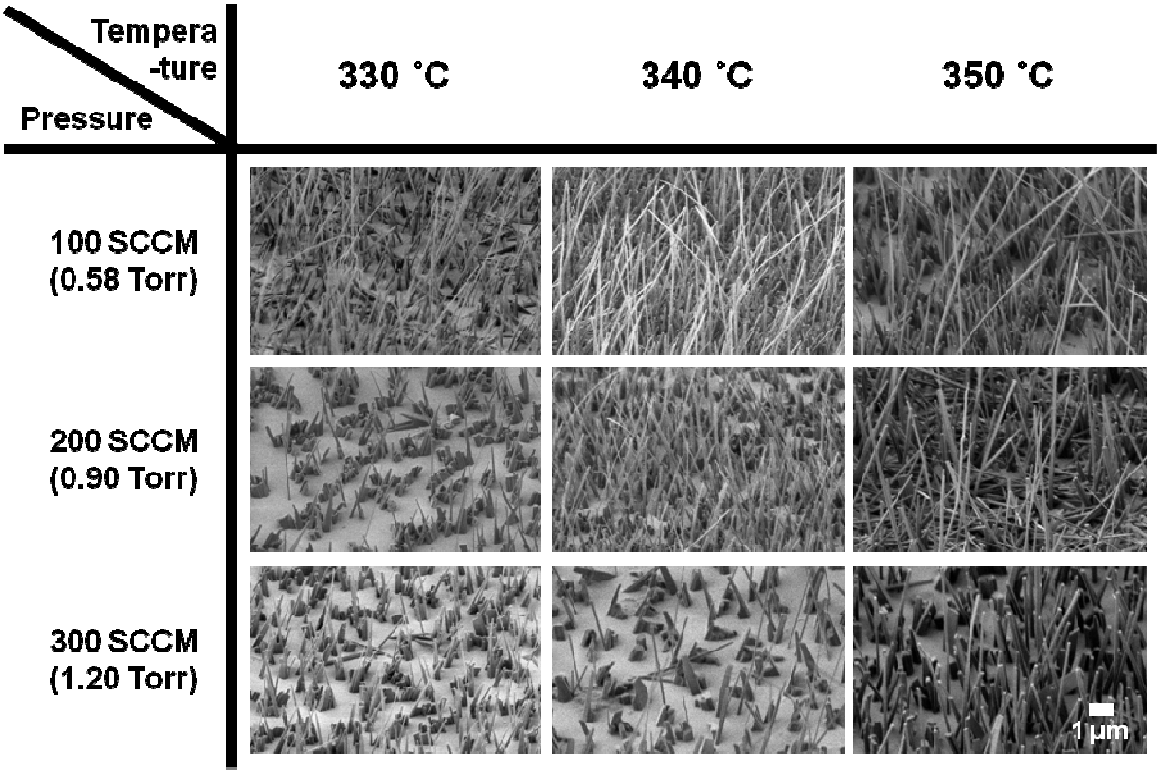

Figure 4-3 Temperature and pressure dependence of DBTTC crystal growth on graphene film.

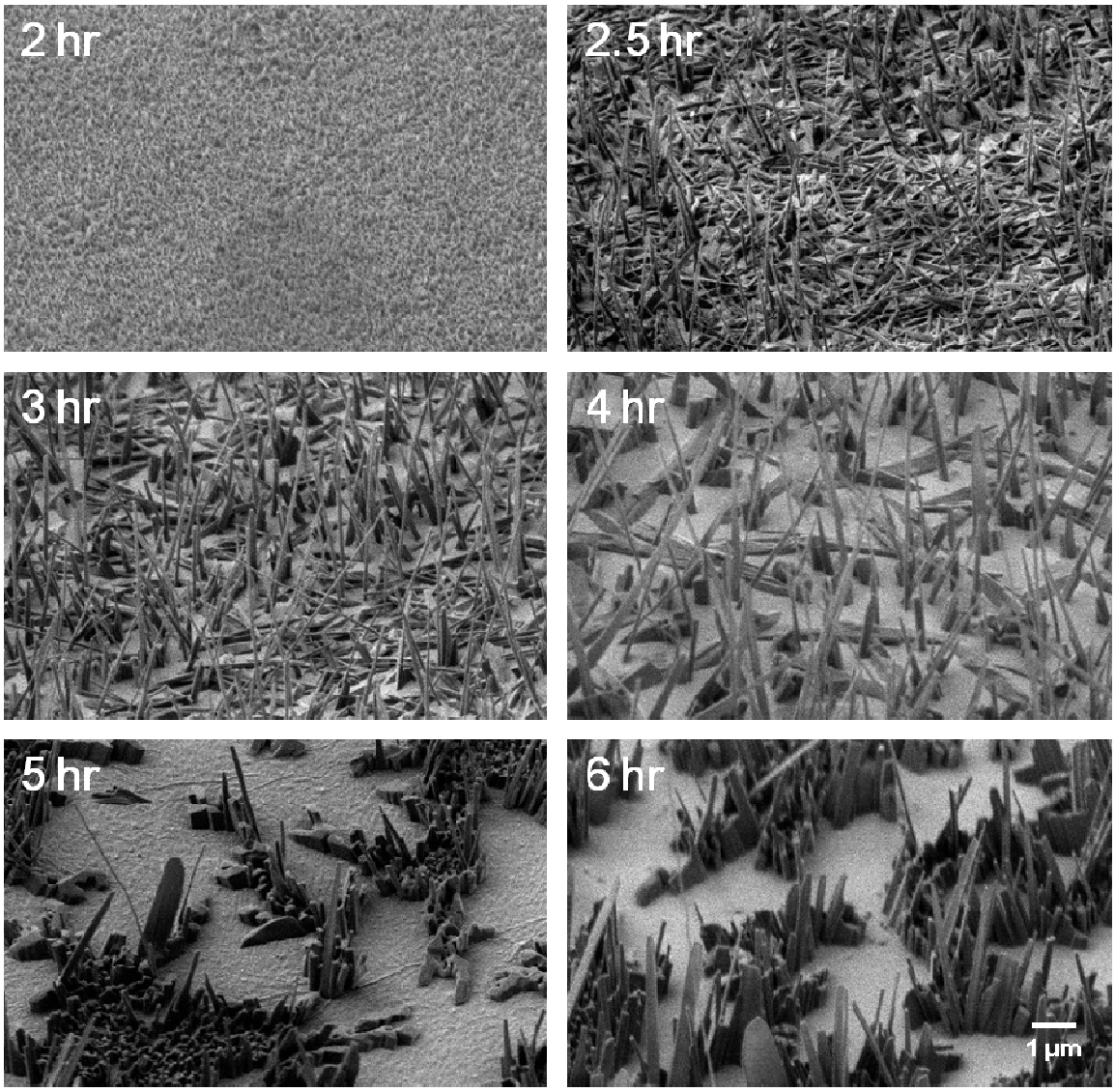

Figure 4-4 Time dependence of DBTTC crystal growth (340 °C, 200 SCCM, 4 mg of DBTTC) 2 hr, 2.5 hr, 3 hr, 4 hr and 6 hr growth (from left to right).

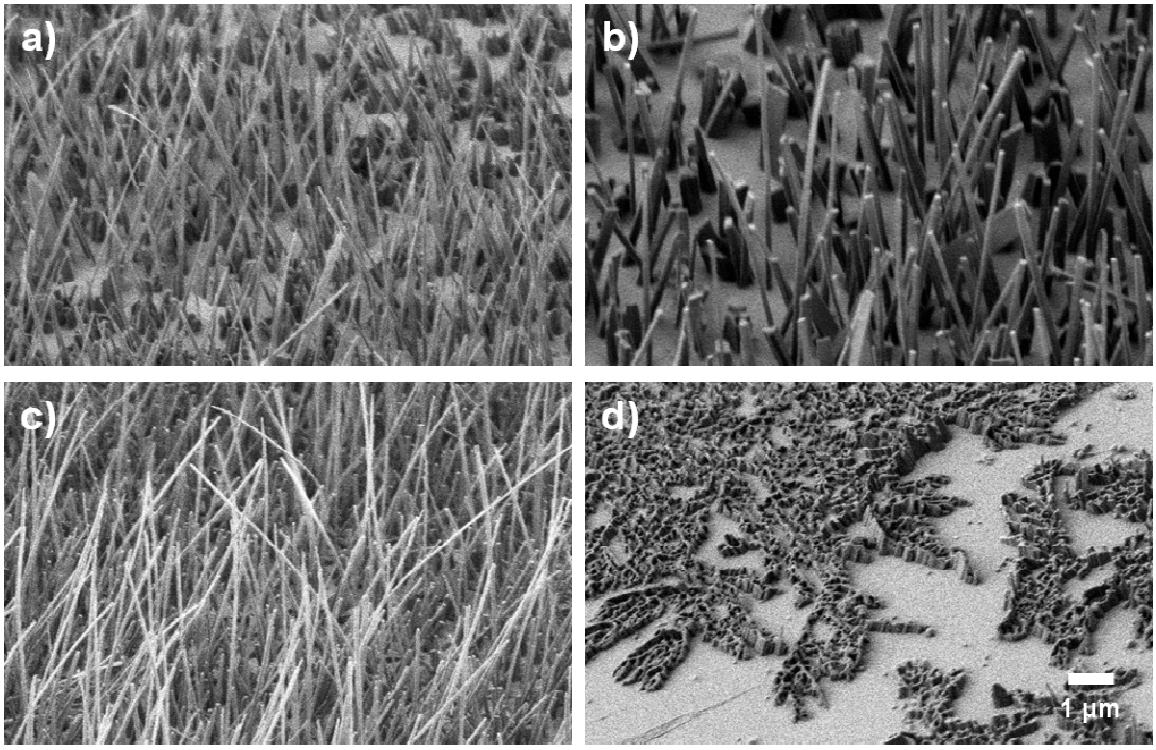

Figure 4-5 SEM images of DBTTC crystals grown on graphene sheets. (a) 340 °C, 200 SCCM, 6 hour growth, (b) 350 °C, 300 SCCM, 6 hour growth, (c) 340 °C, 100 SCCM, 6 hour growth, and (d) 340 °C, 200 SCCM, 2 hour growth. The amount of DBTTC in the feedstock was fixed to 2 mg.

4.4 GIXD analysis of DBTTC crystals

Figure 4-6 shows the 2-D reciprocal (q-) space diffraction patterns for samples (a) through (d) measured at an incident angle of 0.07°, below the critical angle for DBTTC films, measured at NSLS beamline X9. We note that the salient features in the GIXD discussed are observed at higher incident angles (even up to local specular measurements), ensuring the results are representative of the bulk of the film and not dominated by surface effects. Transmission-mode x-ray diffraction of single crystals of DBTTC indicates a triclinic unit

cell with columnar packing of the DBTTC molecules (Figure 4-7); the q-values of the peaks observed in GIXD are in good agreement with the single crystal pattern reflections. Crystallographic order repeated in- and out-of-plane of the DBTTC film are indicated by intensity along the q_r and q_z axes, respectively.

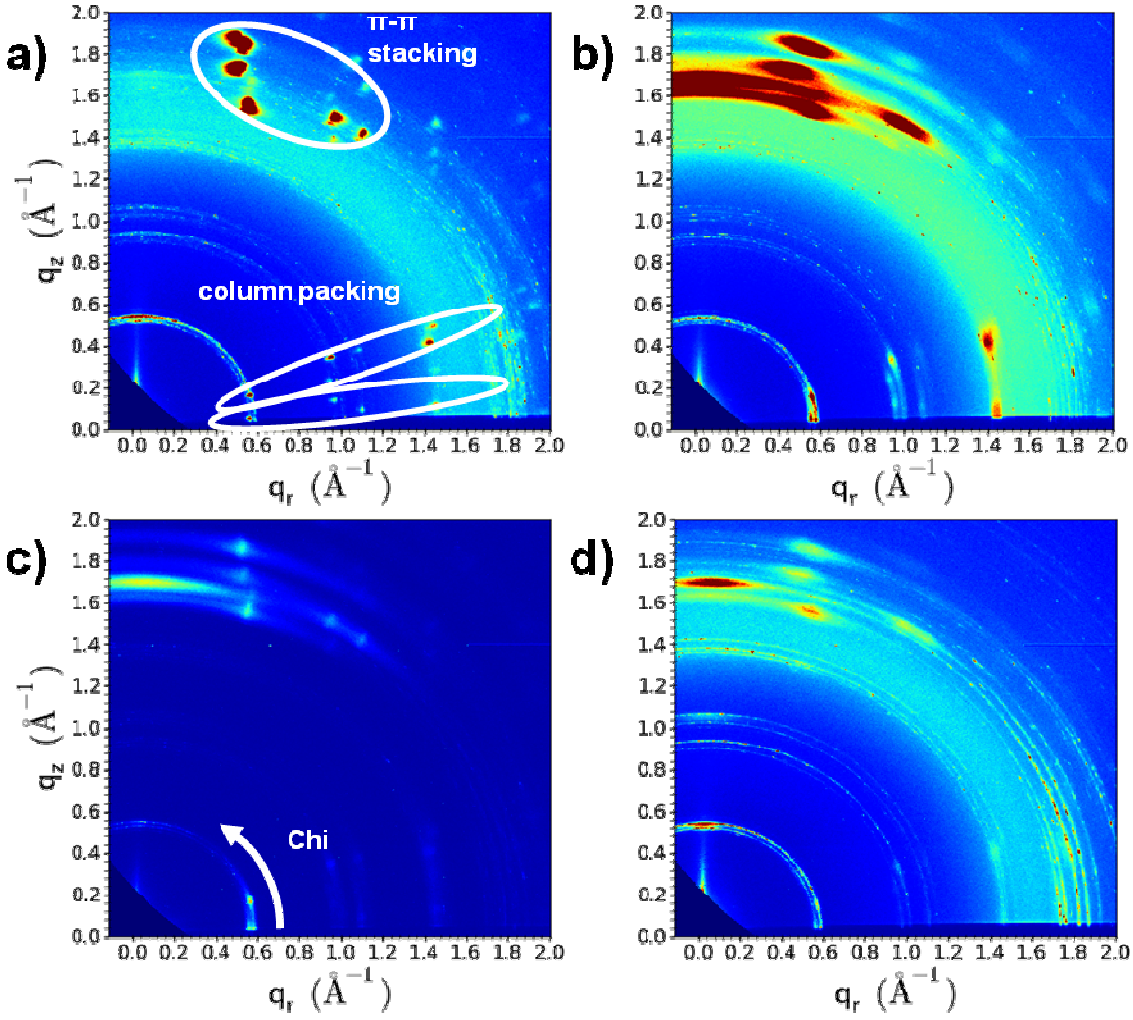

Figure 4-6 GIXD patterns of DBTTC crystals grown on graphene sheets corresponding to the SEM images shown in Figure 4-5 (a) 340 °C, 200 SCCM, 6 hour growth, (b) 350 °C, 300 SCCM, 6 hour growth, (c) 340 °C, 100 SCCM, 6 hour growth, and (d) 340 °C, 200 SCCM, 2 hour growth.

Certain features of the GIXD characterize all DBTTC films on graphene independent of the particular growth conditions explored, from which we can infer the molecular packing and substrate-crystallographic orientation of the films using the unit cell obtained from single crystal diffraction as a reference. These include the trio of reflections between 1.65-2.0 $Å^{-1}$ and neighboring doublet of reflections at q~1.8 $Å^{-1}$, which are all related to the π-stacking of the DBTTC molecules and correspond to repeat distances of ~3.65 Å. The intensity at q=0.51, 0.5399 and 0.542 A^{-1} correspond to the (001), (01-1) and (010) reflections, respectively, and describe the packing of the molecular DBTTC columns, and higher order reflections of the low-q (~0.5 $Å^{-1}$) peaks are observed at 0.9, 1.0 and 1.40 $Å^{-1}$ are also observed. The sharpness and of the molecular packing peaks and the presence of higher order reflections along q_r indicate a highly ordered in-plane packing of the molecular columns, i.e. the crystals consist of rigidly packed 1-D columns which share the vertical axis of the crystal growth.

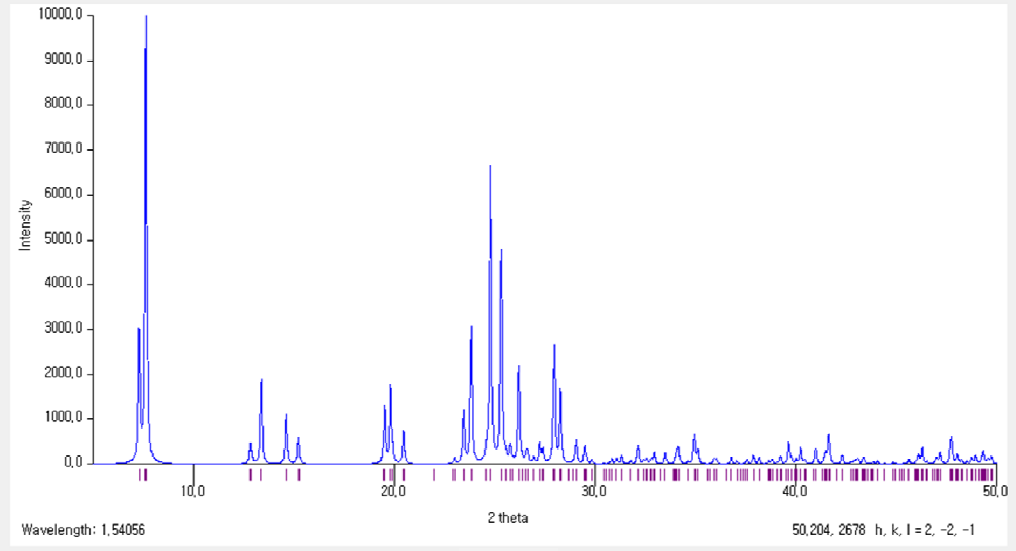

Figure 4-7 X-ray diffraction of single-crystal DBTTC.

In contrast to the molecular column peaks which are always sharp, if not intense, it is clear from Figure 4-6 that the angular spread of the π-stacking reflections is strongly dependent upon DBTTC growth conditions, varying from ~0.05-0.3 $Å^{-1}$ along the Chi-arc direction, with much less variance along the q direction (~0.05-0.1 $Å^{-1}$). This is not unexpected in columnar crystal growth, as deviations from vertical orientation observed in the SEM images of Figure 4-5 would produce a Chi variation in the GIXD. However, the GIXD reflections attributed to columnar packing are quite narrow (<0.05 $Å^{-1}$), and have little to no spread along Chi, independent of the growth conditions. This suggests that the Chi-variance of the π-stacking reflections may be attributable to internal crystal disorder rather than an ensemble-averaged crystal misorientation, which would affect the Chi-spread of all reflections equally. Moreover, we observe both (11-1) and (10-1) reflections, corresponding to repeat distances associated with the DBTTC plate-like core and the “arms” which protrude from the core at a ~20 ° angle, respectively (shown in Figure 4-8(b)), with comparable intensity. This suggests a flexibility of the individual molecules to interact with the graphene through either the π-orbitals of the structurally matched DBTTC core as well as to “anchor” on the substrate through interaction with the hydrogen atoms of the arms of the molecule, which are sensitive to variation of charge density along the graphene surface. This flexibility would facilitate the vertical stacking and manifest as a larger angular spread of the diffraction peaks relative to those of the column packing for the same crystals.

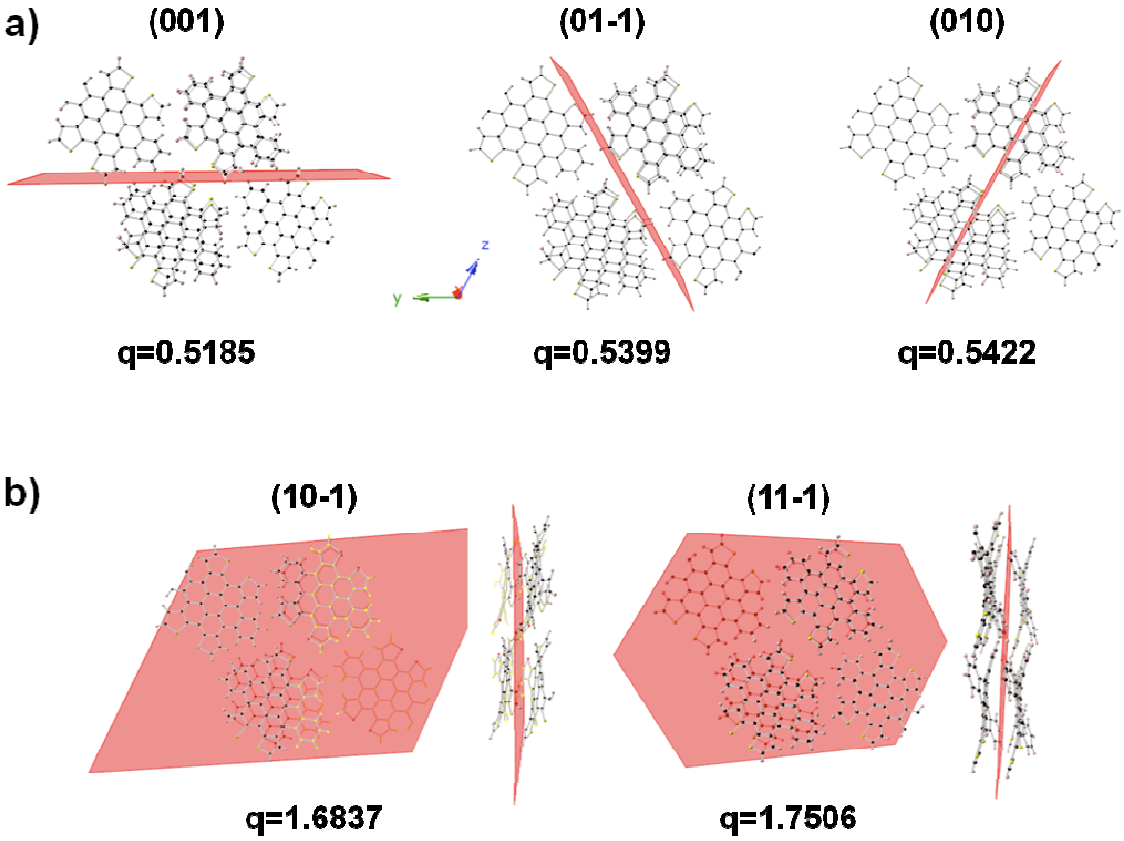

Figure 4-8 Crystal packing distances of DBTTC. (a) columnar packing, (b) π- π stacking.

Having addressed the molecular structure of the crystalline DBTTC nanowires, we now turn to the gross morphology of the overall DBTTC ensemble and gain further insight to the growth mechanism from GIXD. In addition to the well-defined, localized peaks discussed previously, sets of weakly textured rings are also present in the GIXD patterns (Figure 4-6). This combination suggests a bimodal distribution in the films; i.e. two classes of crystallites. We attribute the well-defined peaks to the primary, highly oriented, crystalline rods achieved with extended growth time as indicated in Figure 4-6. The weakly textured rings and broad prominent feature centered at qz=1.72 $Å^{-1}$ are attributed to the residual isotropic crystals that characterize the films in the initial stages of growth seen in Figure 4-5(d).

Thus, the ratio of the integrated intensity of the bright, localized diffraction spots and that of the rings provides an estimate of the volume fraction of nanowire crystals and residual isotropic crystallites. We estimate that samples (a) and (b) (Figure 4-5) exhibit the highest fraction of well-ordered nanowires. However, the wires in sample (b) have a much larger angular distribution of GIXD intensity than sample (a). Since no significant differences were observed at the single wire level with TED, we attribute, the chi-variance in sample (b) to a greater average crystal misorientation from the graphene surface normal. Samples (c) and (d) exhibit much weaker scattering from the nanowires, and may be less ideal for device performance. A larger fraction of hole-conducting vertical nanowires in the DBTTC film should increase the performance of photovoltaic devices made from these materials by maximizing charge separation and extraction.

To gain further insight on the vertical nanocrystal growth mechanism for DBTTC on graphene transferred to SiO_2, we investigate the resulting structure and morphology of DBTTC growth on other surfaces, including highly-oriented pyrolytic graphite (HOPG), CVD pristine graphene grown on copper foil (PG-Cu), SiO_2 surface, and mica with GIXD and SEM, shown in Figure 4-9. The orientation of DBTTC crystals on SiO_2 surface looked mostly arbitrary, presumably due to the lack in π-orbital matching interaction. The same crystal morphology was found on mica film, indicating that vertical growth of DBTTC is mainly attributed by sp^2-carbon surface. However, highly-oriented pyrolytic graphite (HOPG) surface did not grow vertical nanowire DBTTC crystals despite its π-orbital surface. DBTTC crystals on PG-Cu foil were vertically grown, but 2-D nanowalls rather than 1-D nanowires. We attribute these differences to the varying surface roughness of the substrates. AFM and STM studies show that transferred graphene film on SiO_2 has about 1.5 nm RMS surface

roughness while HOPG surface is almost flat with less than 1 nm roughness. (Figure 4-11, 4-12) Graphene-grown copper foil also showed significant surface roughness with preferential puckered pattern formed by thermal annealing. Crystal morphology of graphene grown copper foil shows that DBTTC crystals are grown along the puckers of copper foil, which results in 2-D nanowall crystals. In contrast, the surface roughness on HOPG is negligible and π-orbital interaction between graphite and DBTTC predominates; consequently, DBTTC molecules spread out on the surface rather than stack one on another. Despite different macroscopic morphologies, all of these growths on sp^2-carbon surfaces had the same stacking fashion of DBTTC.

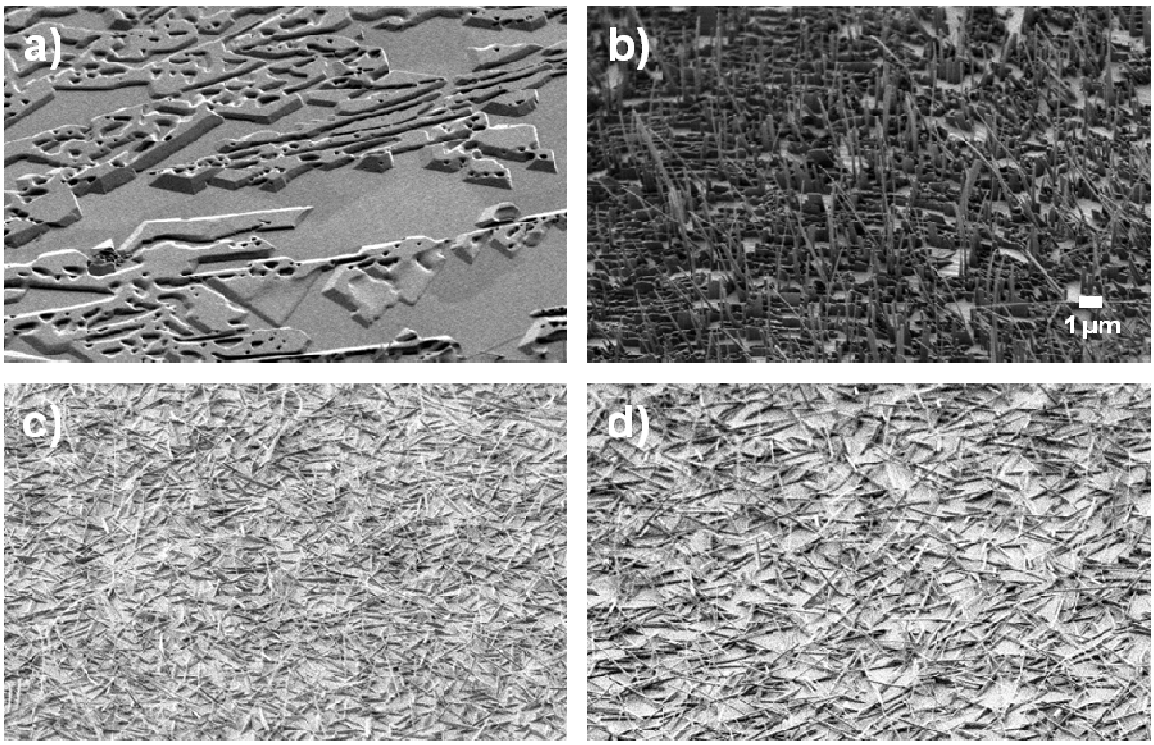

Figure 4-9 DBTTC crystal growth on (a) HOPG, (b) CVD graphene-grown copper foil, (c) SiO_2, and (d) mica film.

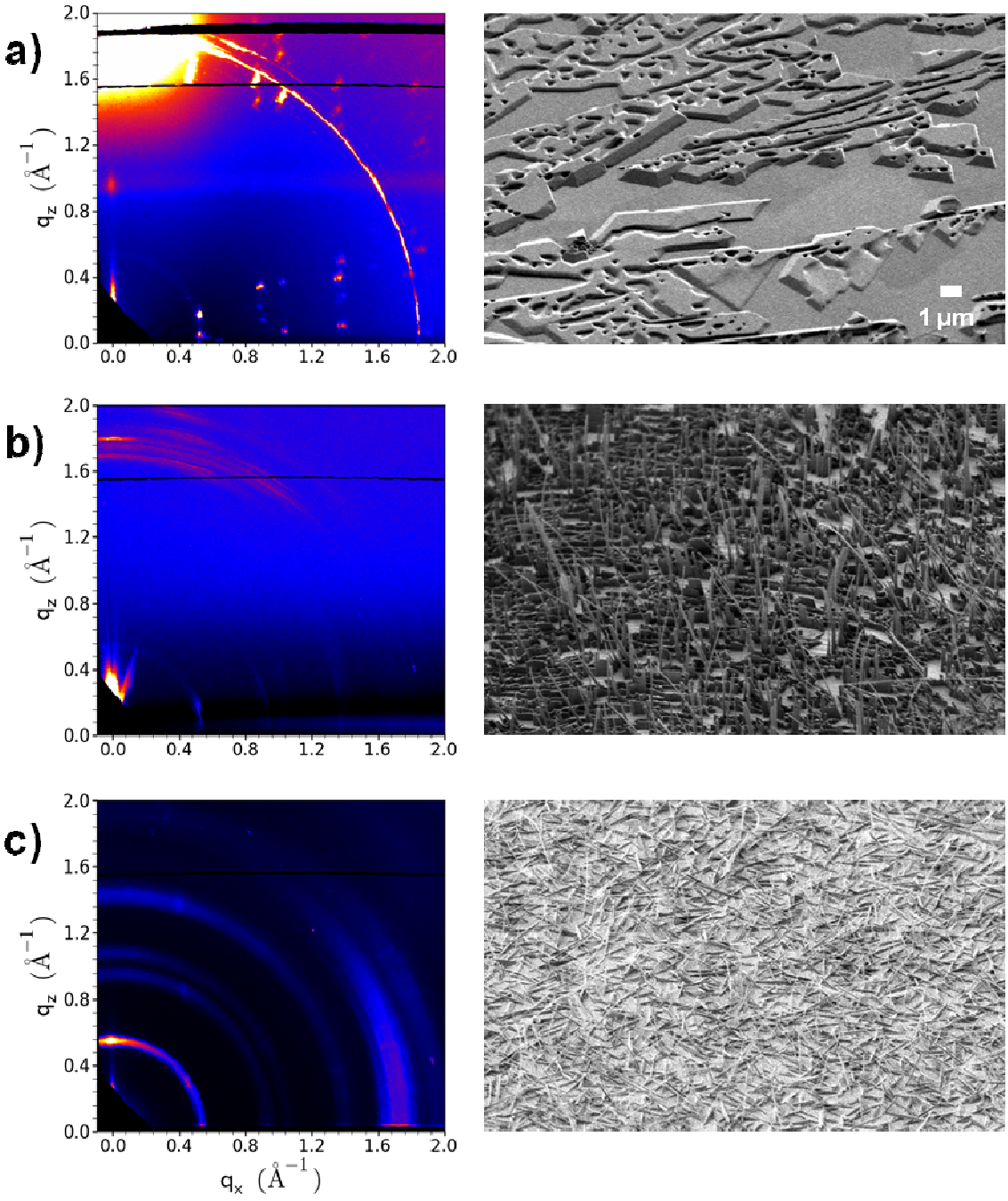

Figure 4-10 GIXD (left) measured at a 0.07 ° incident angle and SEM images (right) for DBTTC crystals grown on: (a) HOPG, (b) graphene (on Cu foil), and (c) SiO_2 surface.

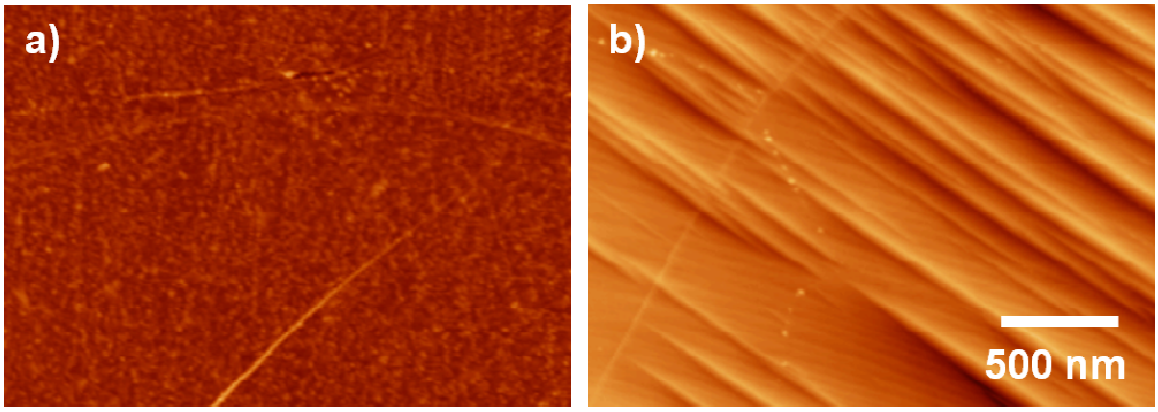

Figure 4-11 AFM images of (a) graphene transferred to SiO_2 surface, and (b) graphene grown copper foil.

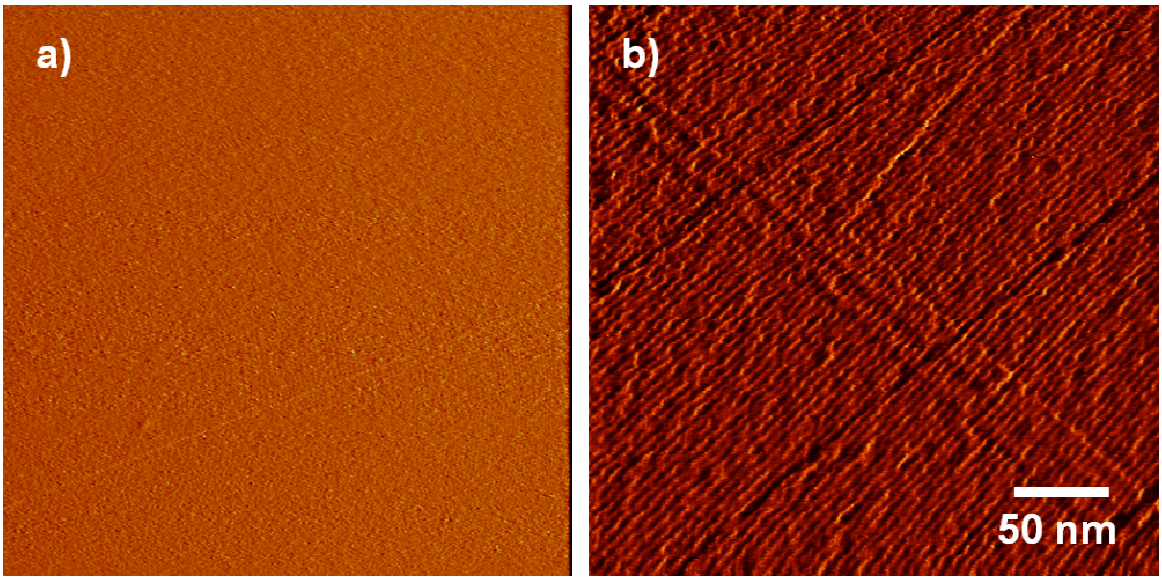

Figure 4-12 STM images of (a) HOPG and (b) graphene grown on copper foil.

GIXD measurement of these samples was performed to study morphology change of DBTTC crystals as the surface changes. (Figure 4-10) DBTTC crystals on SiO_2 surface showed the same crystallinity, which indicates that the crystal packing structures are the same no matter where the crystals were grown. However, it showed radial peaks rather than

specific peaks; this can be explained by arbitrary direction of DBTTC crystals on SiO_2. On the other hand, the GIXD of DBTTC crystals on HOPG showed much well-defined peaks than GIXD in Figure 4-10(a); it shows multiple order peaks of π-π stacking and columnar packing. From the SEM images, it shows parallelogram-shaped crystals, which correspond to macroscopic crystal packing of planar direction (100 plane). This suggests greater interaction between HOPG and DBTTC molecules; the surface interaction is superior to columnar stacking of DBTTC, and consequently DBTTC molecules tend to spread out over the HOPG surface rather than stacked up as nanowires. Instead, DBTTC interacts only with π-orbitals, and doesn't have any angular variation which guarantees more refined peaks.

Field-effect transistor (FET) of DBTTC single crystal was fabricated to investigate device characteristics of the crystals. (Figure 4-13) FETs were fabricated by gold electrode evaporation (50 nm) on DBTTC crystals grown on SiO_2 surface with argon flow (1 atm, 100 SCCM). The transfer curve showed that DBTTC crystal works as p-type semiconductor under negative gate voltage. The steep rise of output characteristic curve indicates that this device has great carrier injection, and no contact resistance problem was found. The field-effect mobility was calculated to be 0.022 cm^2/Vs.

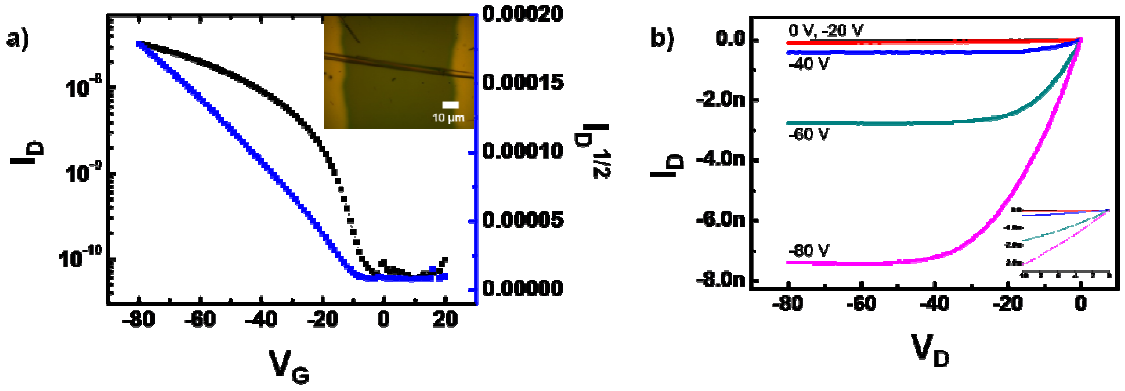

Figure 4-13 Field-effect transistor characteristics of DBTTC crystal: (a) gate-sweep transfer curve and (b) output curve.

In conclusion, we grew vertical organic nanowire crystals of DBTTC on large-scale graphene with reasonable coverage and uniformity. DBTTC crystals were grown vertically only on graphene film transferred onto SiO_2 surface. By measuring GIXD of DBTTC crystals grown on different surfaces, π-π interaction and surface roughness were found to be the driving force of nanowire growth on graphene surface. On HOPG film, π-π interaction was maximized and DBTTC molecules were spread over HOPG surface due to the lack of surface roughness. GIXD also verified the crystal packing structures and orientation, showing the nanowires consist of well-packed molecular columns with the π -stacking. This is noteworthy in that vertical π-stacking with perfect overlap advantages in hole transport, which gives a great potential of extensive applications in organic optoelectronics. Long and thin crystals can be used in light-collecting antenna devices; short and dense crystals can be a great bulk-heterojunction photovoltaic cell.

Experimental Section

4.1. Large-scale graphene growth

Single-layer graphene sheet was prepared by thermal chemical vapor deposition (CVD) method. 0.05 inch thick copper foil (99 %) was used as a catalyst. The copper foil was placed in a tube furnace and the system was purged with argon gas (200 SCCM) with roughing pumping to have 1.2 Torr of pressure. Then the furnace was rapidly heated up to 1000 °C. When the furnace reached 1000 °C, hydrogen gas (10 SCCM) was added to reduce the copper foil surface for 10 minutes. (6.4×10^{-2} Torr) After the annealing step, the growth was started by adding methane gas (170 SCCM, 1.7 Torr) for 18 min. When the growth was done, the system was purged with argon gas and slowly cooled down to room temperature.

4.2. Graphene transfer to SiO_2 substrate

Graphene grown copper foil was cut into desirable size (1.5×1.5 cm^2) and mounted onto glass substrate with tape. Then 950 PMMA (A5) was spincoated on the graphene grown copper film with 5000 rpm for 60 seconds. Then photoresist (AZ P4330-RS) was consequently spincoated on the copper film with 5000 rpm for 60 seconds. The spincoated film was baked at 50 °C for 10 minutes, to make sure that the film is dried. This foil was then floated on $FeCl_3$ solution (30% wt). The removal of copper film was checked by the film transparency; if the film turned transparent, copper is all etched by $FeCl_3$ solution. After the etching is finished, the floating film was transferred to water to rinse out some residual copper as well as $FeCl_3$ solution, and the film was finally caught on SiO_2 substrate. The substrate with graphene film was dried under mild heating (~ 40 °C) until water is fully dried.

After the film was fully stuck on the substrate, the substrate was dipped in acetone to remove PMMA and photoresist films. To make sure that all the residuals were removed, the samples were annealed at 300 °C under 150 SCCM of argon and 10 SCCM of hydrogen for an hour.

4.3. Crystal growth of DBTTC

Crystal growth of DBTTC on graphene was performed in physical vapor deposition system. The growth system was prepared with a temperature gradient zone furnace, argon gas flow and a vacuum pump. The powder of DBTTC was placed in the highest temperature zone, while the SiO_2 substrate with pristine graphene sheet was in a temperature gradient zone. It was important to place the substrate with a right angle to the gas flow so that graphene react uniformly with vaporized DBTTC molecules. After the sample was loaded, the system was purged with argon gas and vacuum was applied to maintain constant pressure. Temperature of the system was then gradually increased to the target temperature (50 °C/min). After 6 hours of growth, the system was cooled down and the sample was retrieved for further analysis.

References for Chapter 4

[1] de Boer, R. W. I. W. *Physica status solidi. A, Applied research* **2004**, *201*, 1302.

[2] Hasegawa, T. *Science and technology of advanced materials* **2009**, *10*, No.

[3] Jiang, L. *Journal of materials chemistry* **2010**, *20*, 4994.

[4] Warta, W. *Physical review. B, Condensed matter* **1985**, *32*, 1172.

[5] Menard, E. *Advanced materials (Weinheim)* **2004**, *16*, 2097.

[6] Podzorov, V. *Physical review letters* **2004**, *93*, 086602.

[7] Sundar, V. C. *Science (New York, N.Y.)* **2004**, *303*, 1644.

[8] Takeya, J. *Applied physics letters* **2007**, *90*, 102120.

[9] Campione, M. *The open applied physics journal* **2010**, *3*, 17.

[10] Tseng, R. J.; Chan, R.; Tung, V. C.; Yang, Y. *Advanced Materials* **2008**, *20*, 435.

[11] Kim, K. S. *Nature (London)* **2009**, *457*, 706.

[12] Li, X. *Science (New York, N.Y.)* **2009**, *324*, 1312.

[13] Li, X. *Nano letters* **2009**, *9*, 4359.

[14] Nair, R. R. *Science (New York, N.Y.)* **2008**, *320*, 1308.

[15] Novoselov, K. S.; Geim, A. K.; Morozov, S. V.; Jiang, D.; Katsnelson, M. I.; Grigorieva, I. V.; Dubonos, S. V.; Firsov, A. A. *Nature* **2005**, *438*, 197.

[16] Zhang, Y.; Tan, Y.-W.; Stormer, H. L.; Kim, P. *Nature* **2005**, *438*, 201.

[17] Lee, W. H. *Journal of the American Chemical Society* **2011**, *133*, 4447.

[18] Chiu, C.-Y.; Kim, B.; Gorodetsky, A. A.; Sattler, W.; Wei, S.; Sattler, A.; Steigerwald, M.; Nuckolls, C. *Chemical Science* **2011**.

[19] Gorodetsky, A. A.; Chiu, C.-Y.; Schiros, T.; Palma, M.; Cox, M.; Jia, Z.; Sattler, W.;

Kymissis, I.; Steigerwald, M.; Nuckolls, C. *Angewandte Chemie* **2010**, *122*, 8081.

[20] Blake, P. *Applied physics letters* **2007**, *91*, 063124.

[21] Meyer, J.; Scardaci, V.; Casiraghi, C.; Lazzeri, M.; Mauri, F. *Physical Review Letters* **2006**, *97*.

[22] Laudise, R. A.; Kloc, C.; Simpkins, P. G.; Siegrist, T. *Journal of Crystal Growth* **1998**, *187*, 449.

Chapter 5

Photovoltaic Universal Joints: Ball-and-Socket Interfaces in Molecular Photovoltaic Cells*

* Part of this chapter was reproduced with permission from *ChemPhysChem*:
"Photovoltaic Universal Joints: Ball-and-Socket Interfaces in Molecular Photovoltaic Cells" by Noah J. Tremblay, Alon A. Gorodetsky, Marshall P. Cox, Theanne Schiros, Bumjung Kim, Rachel Steiner, Zachary Bullard, Aaron Sattler, Woo-Young So, Yoshimitsu Itoh, Michael F. Toney, Hirohito Ogasawara, Arthur P. Ramirez, Ioannis Kymissis, Michael L. Steigerwald, and Colin Nuckolls. © 2011 John Wiley and Sons.
*My contribution on this study was mainly focused on co-crystal growth of C_{60} and HBC. Solar cell fabrication and analysis were done by others.

5.1 Background

Herein, we detail how to grow one crystalline organic semiconductor on another epitaxially and thereby provide a method to tune the electronic nature of the p–n junction in organic photovoltaics (OPVs). While OPVs are attractive as materials for conversion of sunlight into electrical energy,[1] higher conversion efficiencies[2] are needed for OPVs to become a viable technology.[3–6] Regardless of the type of OPV, either a bilayer[7] or bulk-heterojunction (BHJ)[4] (Figure 5-1(a)), the interface between the hole and electron transporting films is the critical locus for exciton formation and dissociation.[8–11] In inorganic materials, the interface between two semiconductors is crucially important in determining and controlling the electrical properties of these materials and is controlled by a heteroepitaxial growth of one crystalline material on another. We show here that p-type and n-type organic semiconductors can be designed to have nested shapes that create an epitaxial growth that achieves higher conversion efficiencies and open circuit voltages in these devices

to within 10% of the theoretical limit. We utilize the class of molecules known as contorted hexabenzocoronenes (HBCs, Figure 5-1(b)) because they are established p-type semiconductors[12–14] and are also photoconductive.[15, 16] This HBC has an unusual shape in that it is contorted and doubly-concave.[12] The size and shape of this molecule are complementary to buckminsterfullerene (C_{60}), which is a well-known n-type semiconductor (Figure 5-1(c)). It is this potential for shape and electronic complementarity between these two molecular structures that led us to investigate them in the context of heteroepitaxial growth.

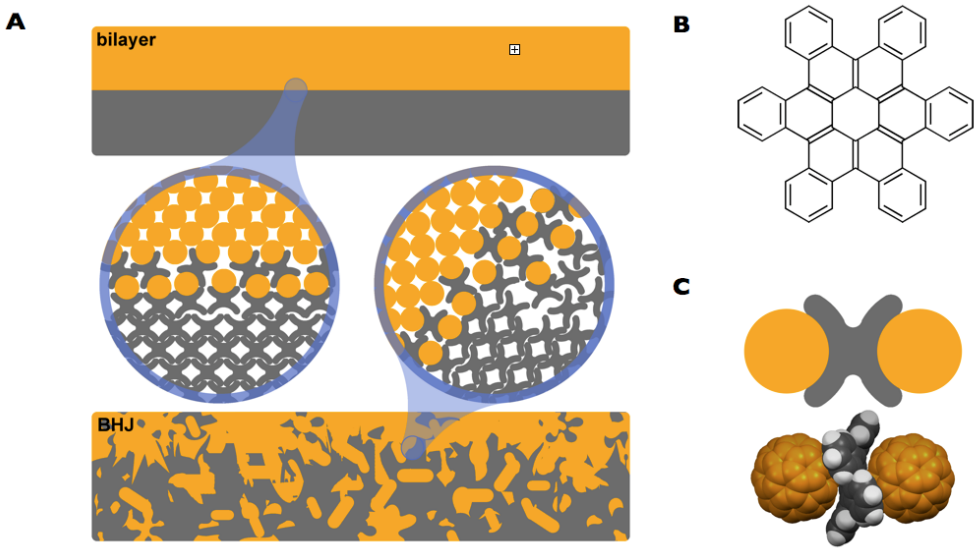

Figure 5-1 (a) Depiction of ball-and-socket interfaces in bilayer and bulk heterojunction devices. (b) The chemical structure of the *contorted*-HBC. (c) Correlation between depiction (*top)* and molecular structure from the co-crystal of HBC and C_{60} (*bottom*).

5.2 Co-crystal Growth of Hexabenzocoronene and C_{60}

We first focused on whether HBC and C_{60} formed co-crystalline, supramolecular assemblies. Two experiments, one from solution (Figure 5-2(a)) and one from the gas phase (Figure 5-2(b)) show that the materials form co-crystals. Large purple-gray crystals were produced from a saturated solution of C_{60} and HBC in chlorobenzene.

The molecular structure determined from the solution grown crystals reveals that HBC and C_{60} spontaneously formed an interdigitated supramolecular complex (complex **1**). The three-dimensional structure of HBC comprises two opposing concave aromatic faces, wherein a C_{60} had nestled into each face (Figure 5-2(a)). It is important to note that a number of organic molecules have been specifically designed to form complementary interactions with C_{60} and have yielded co-crystals.[17–20] However, few of these molecules are suitable candidates for the formation of a p–n junction.[17]

The crystal of **1** comprises C_{60}, HBC, and chlorobenzene (2:1:1), wherein HBC and C_{60} organize into a repeating pattern of ABAABA as shown in Figure 5-2(a). Each HBC has two C_{60} nearest neighbors, and each C_{60} has one HBC nearest neighbor and one C_{60} nearest neighbor. The C_{60} is centered over one of the six-membered rings on the edge of the coronene core of HBC; in this instance, the vertical π–π distance is 3.00 Å.

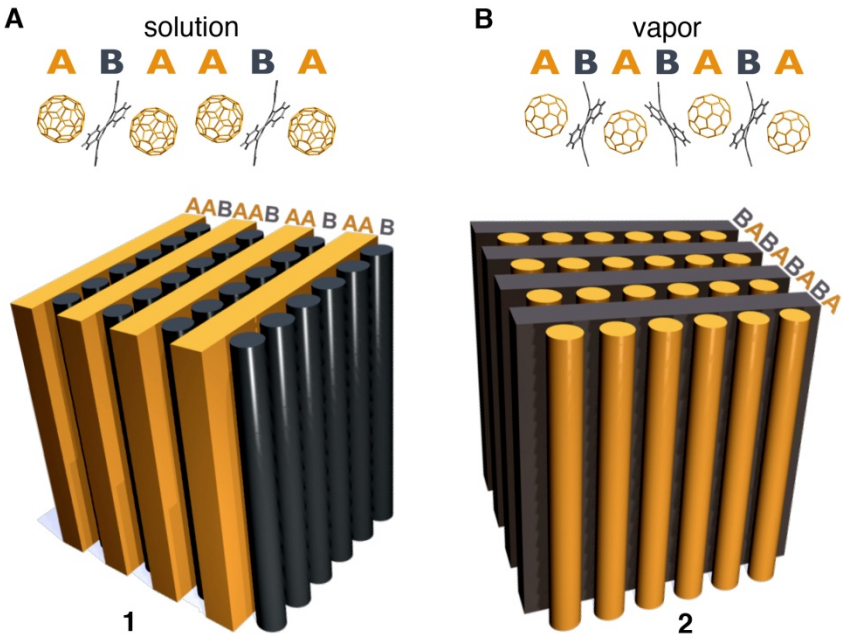

Figure 5-2 Organization of HBC and C_{60} in co-crystals of C_{60} and HBC (a) from solution as complex **1** and (b) from the gas phase as complex **2** (*right*).

We were also able to co-crystallize these molecules without solvent using horizontal physical vapor transport.[21] We placed HBC and C_{60} powders in the hot zone (550 ºC) of a horizontal, gradient-temperature furnace. Crystals (complex 2) formed in the cold zone of the furnace (330 ºC). The composition of **2** was 1:1 HBC:C_{60} (Figure 5-2(b)).

The assembly of HBC and C_{60} in **2** is different from **1**. The HBC and C_{60} organize in an ABAB repeating pattern in **2** (Figure 5-2(b)). In this structure there are two crystallographically inequivalent HBC sites. Every HBC has two C_{60} nearest neighbors with the C_{60} having two non-identical HBC neighbors. Each C_{60} is centered directly in the middle of the core six-membered ring in one type of HBC at a π–π distance of 2.93 Å. Each C_{60} is also centered over another HBC just outside one of the bonds of the core six-membered ring at a π–π distance of 3.07 Å. The HBC molecules in **2** are organized in sheets (Figure 5-2(b)).

Even though there are two inequivalent HBC sites, they are assembled into a rectangular array with a center-to-center distance of 11.36 Å. Every HBC molecule has a 3.63 Å close carbon-tocarbon contact with four neighboring HBCs.

The C_{60} molecules in **2** form columns (Figure 5-2(b)). The center-to-center distance between the columns is 9.88 Å, which is one of the shortest C_{60}-C_{60} distances reported to date.[22, 23] The fullerenes assemble in a zigzag pattern with a 111º bend (center-to-center) at each C_{60}. The columns are spaced 15.87 Å apart from one another. A spacing of 9.88 Å is within the range of previously reported values for C_{60}-C_{60} spacings in the pure crystal, but 15.87 Å is significantly larger than those values, indicating that C_{60} forms columns in **2**.

5.3 Device Measurement of Co-crystals.

The solution-grown crystals of **1** were large enough that we were able to directly measure the resistance of single crystals using evaporated silver electrodes (Figure 5-3). These crystals are insulating, which is expected as both HBC and C_{60} individually are semiconductors. The resistance was significantly reduced after the same species was kept in vacuum at room temperature for twelve days. We presume that this is due to the slow evaporation of chlorobenzene. Illumination of the devices causes a 1,000-fold decrease in resistance. Crystals of **2** were not large enough to measure in single-crystal devices.

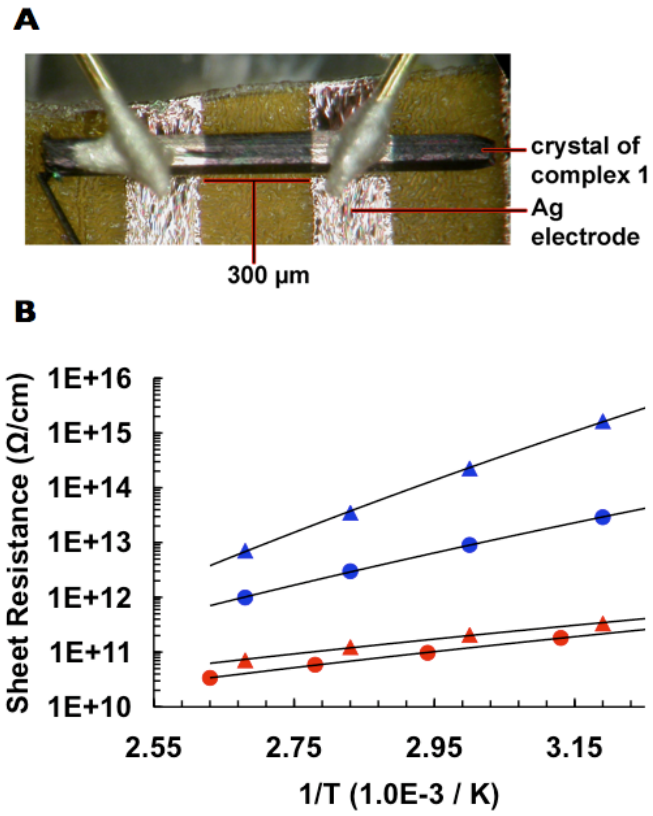

Figure 5-3 (a) Labeled photograph of a single-crystal device of complex **1**. (b) Inverse temperature vs. sheet resistance of the device measured before annealing (triangles), after annealing (circles), with illumination (red), and without illumination (blue).

5.4 Photovoltaic Cell Fabrication Using Hexabenzocoronene and C_{60}

We made OPV devices to test our hypothesis that the large decrease in resistance in the crystals is due to charge transfer between the n- and p-type molecules. We chose an OPV bilayer architecture (Figure 5-4(a)) rather than a BHJ architecture because it is easier to optimize the former. We used an electrode pattern that allowed for rapid and reproducible electronic characterization of over 200 devices at a time. Standard electrode materials were deliberately used for all devices for direct comparison to literature values.[24] We measured the electrical characteristics of these devices in the dark, and then again when they were

exposed to a 1.5 AM solar-simulated light source (power density = 1 sun, 100 mWcm^2). The devices were open to air during the measurements unless otherwise noted.

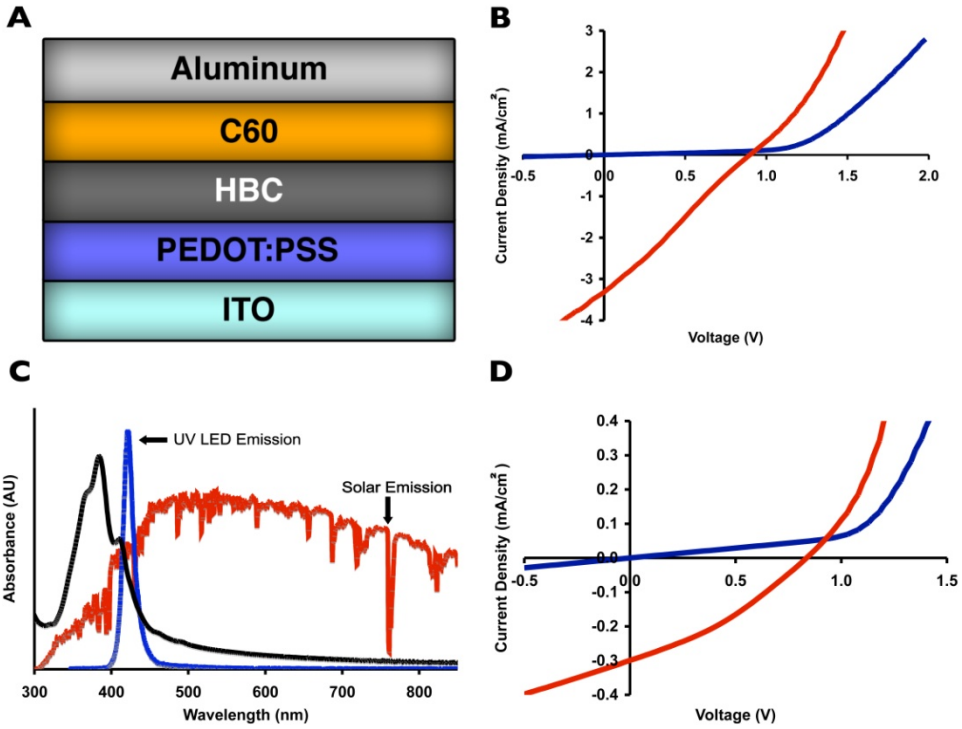

Figure 5-4 (a) Schematic of the OPV device architecture: PEDOT:PSS (25nm), HBC (25nm), C60 (40nm), Aluminum (60nm). Device are is 0.16 cm^2. (b) J-V characteristics of *contorted*-HBC OPVs in the dark (blue) and illuminated with 1.5 AM solar simulated light source (red). (c) Absorbance spectrum of a thin film of *contorted*-HBC (black) overlaid with the emission of the UV LED light source (blue) and the solar spectrum (red). (d) J-V characteristics of *contorted*-HBC OPVs in the dark (blue) and illuminated with UV LED light source at 422 nm and an intensity of 1.5 mW/cm^2 (red).

The illumination-dependent current density/voltage characteristics of an HBC/C_{60} device appear in Figure 4B: a short-circuit current density (J_{SC}) of 3.32 mA/cm^2, open-circuit voltage (V_{OC}) of 0.88 V, and a fill factor of 0.27 yield an efficiency of 0.77 %. These values are not high enough to be viable in technology, but are very good given the poor absorbance of the HBC and the high V_{OC} in the device. It charts a path to more efficient devices that would shift the absorbance of the HBC to absorb more broadly in the solar region of the spectrum As support for this, the normalized external quantum efficiency (EQE) spectra show the highest value for the relative efficiency near 390 nm. This is close to the maximum in the absorbance of the HBC thin film (Figures 5-5 and 5-6).

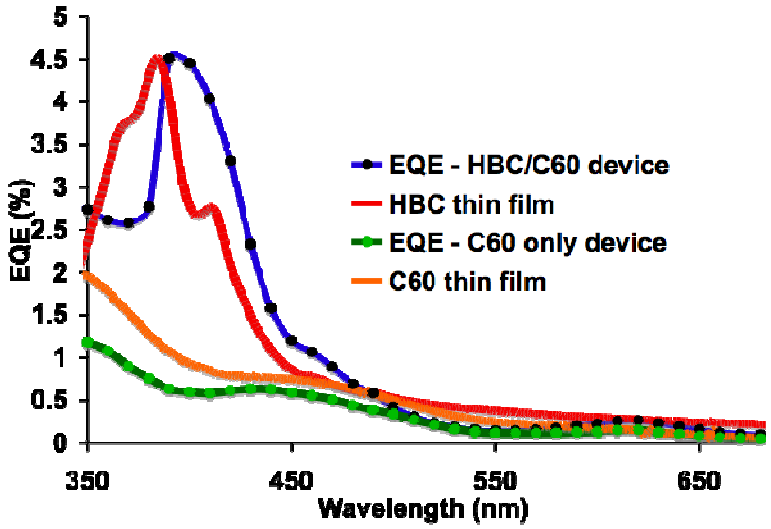

Figure 5-5 External Quantum Efficiency (EQE) spectrum of a *contorted*-HBC/C_{60} device (black dots) and EQE of a C60 device without the HBC layer (light green dots). Blue and green lines are guides to the eye. The spectra has been normalized and represents relative values. The normalized absorbance of HBC (red line) and C_{60} (orange line) thin films are also shown for comparison.

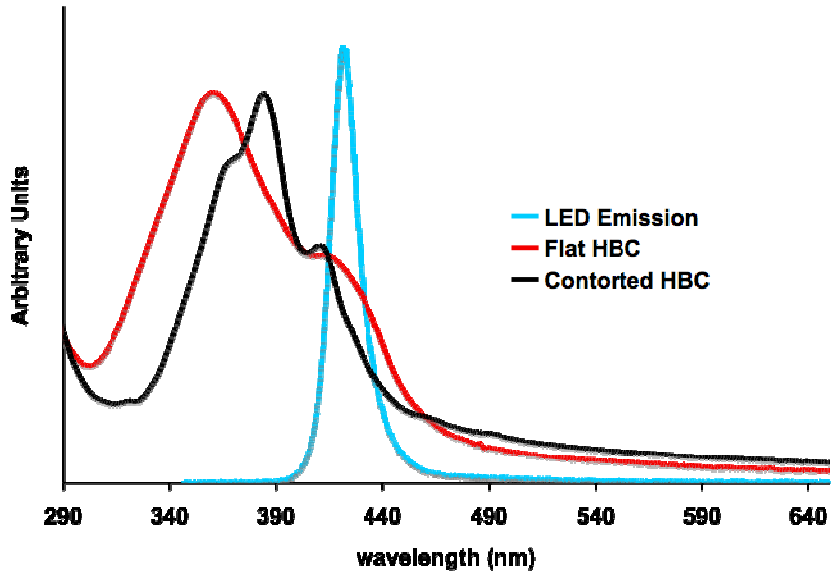

Figure 5-6 Overlaid thin-film absorption spectra of *contorted*-HBC and *flat*-HBC along with the emission spectrum of the UV LED light source.

The efficiency of a photovoltaic device is proportional to the magnitude of the V_{OC}. To a first approximation, the theoretical maximum V_{OC} for our devices is the energy difference between the highest occupied molecular orbital (HOMO) of HBC at ~5.5 eV and the lowest unoccupied molecular orbital (LUMO) of C_{60} at ~4.5 eV. Our V_{OC}s approach this difference of 1.0 V. These are among the highest values reported for OPVs.[3]

The efficiency of a photovoltaic device is also directly proportional to the J_{SC}. Upon illumination, the current density of the HBC/C_{60} devices clearly increases, regardless of the applied bias. This is consistent with our observations of photoconductivity[15, 16] in HBC films and HBC/C_{60} co-crystals (Figure 5-3).

The device performance observed here is unexpectedly good given that the absorbance of HBC overlaps poorly with the simulated solar spectrum (Figure 5-4(c)). When

the devices were irradiated at 422 nm near the maximum of the normalized EQE spectrum, we observed conversion efficiencies of up to 5.7% (Figure 5-4(d)).[25] There is only a slight change in the average V_{OC} of these devices upon moving from solar to UV LED illumination (Figure 5-4(b), (d)). The performance of HBC/C_{70} devices is essentially the same as that of HBC/C_{60} devices (Figure 5-7). All the devices were operated in ambient atmosphere without any encapsulation.

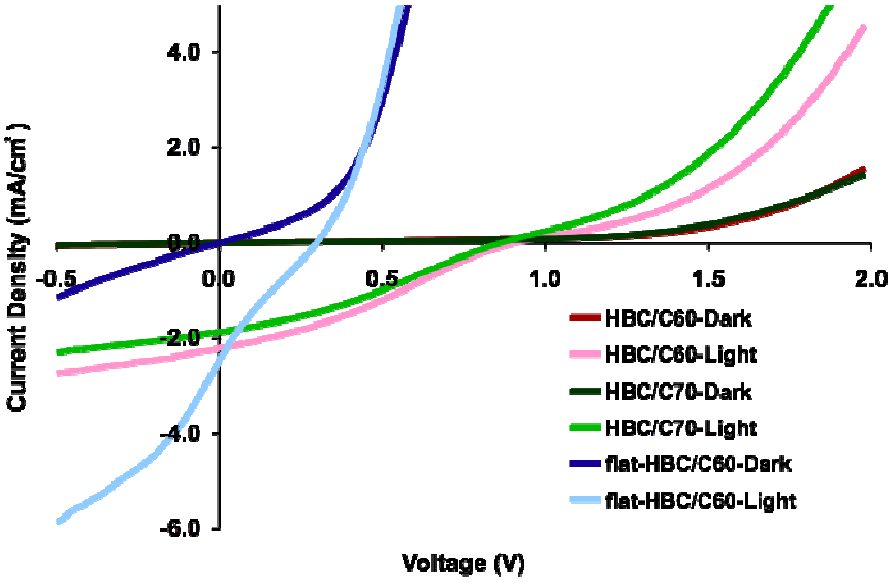

Figure 5-7 Current vs. voltage graphs show the average device characteristics for **1**) *contorted*-HBC/C_{60}: red (hidden behind dark green) is the dark current; pink is the illuminated current. **2**) *contorted*-HBC/C_{70}: dark green is the dark current; light green is the illuminated current. **3**) *flat*-HBC/C_{60}: dark blue is the dark current, and light blue is the illuminated current.

We have seen that HBC and C_{60} form a tight molecular complex. We have also seen that bilayer OPV devices using these two compounds have good functional performance. We have previously used grazing incidence X-ray diffraction (GIXD) to detect co-crystalline regions within polymer/fullerene BHJs[26] and herein we use the same technique to analyze the HBC/C_{60} interface. We collected GIXD data from HBC-coated silicon substrates after stepwise depositions of C_{60} onto the HBC (25 nm). We increased the thickness (x nm) of the C_{60} layer from 0 nm to the optimal device thickness of 40 nm (Figure 5-8).

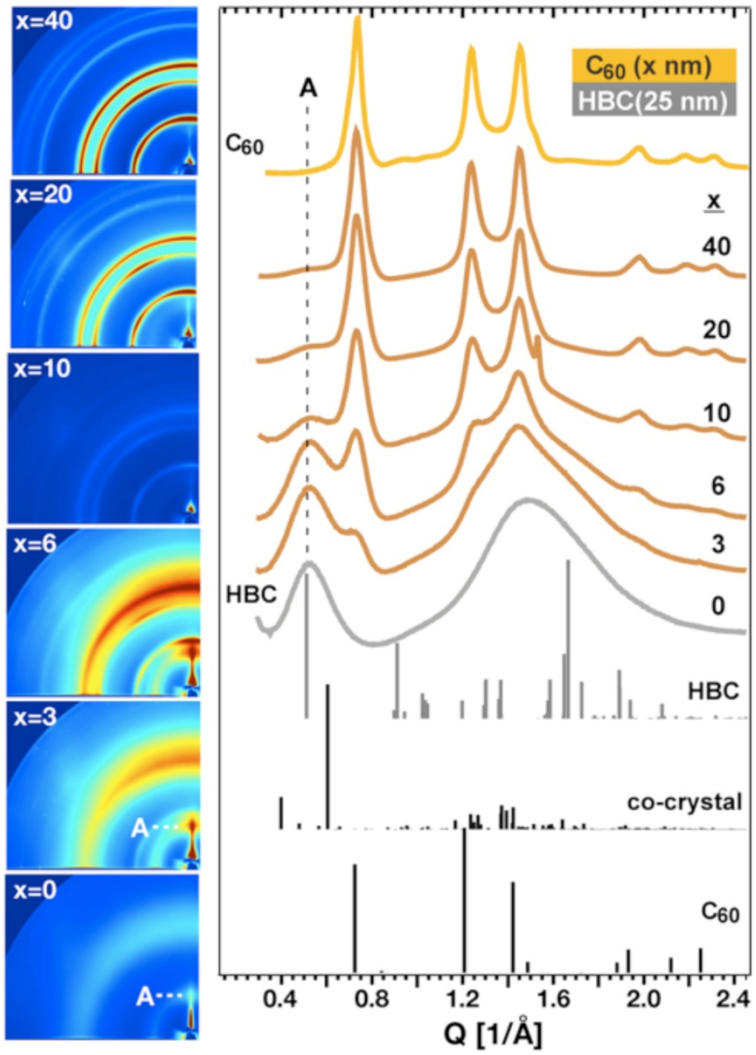

Figure 5-8 GIXD measurements (2-D images on the left and integrated intensity on the right) for films of C_{60} (40 nm), bilayers of decreasing thickness of C_{60} on HBC, and pure HBC (25 nm). Integrated intensities of the diffraction pattern are normalized by the maximum peak height; 2-D images for x=0-10 nm share the same intensity scale while x-20 and 40 nm have a larger upper limit due to the thickness of the film. Feature A indicates diffraction intensity confined to the Qz direction which increases in intensity at the HBC/C_{60} interface before disappearing under the C_{60} signal.

The film of pure HBC shows weak crystalline order; a weak (100) reflection at Q=~0.5 $Å^{-1}$, labeled "A" in Figure 5-8, is largely confined to the vertical direction (Q_z) and indicates that the HBC molecules are oriented within a 5–108 tilt from the surface normal, while the breadth of the peak indicates small crystallite domains. The broad peak centered at Q=~1.5 $Å^{-1}$ is dominated by the signal from the SiO_2 substrate which overwhelms that of any HBC reflections. When 3–6 nm of C_{60} is deposited on top of the HBC film, the intensity of peak A increases significantly along the vertical, and C_{60} peaks [Q = ~0.75 (peak B), 1.24 and 1.5 $Å^{-1}$] also appear. However, in the absence of an interaction between HBC and C_{60}, the (100) reflection from pure HBC should be damped rather than enhanced by a thin C_{60} layer at grazing incidence. Instead, we find that while the intensity of the C_{60} peaks increase linearly with increasing film thickness for all deposition steps, the intensity of peak A increases for thin C_{60} films ($x \leq 6$ nm), that is, at the interfacial region, before decreasing as it becomes buried by the C_{60} (see Figure 5-8 inset). The increase in intensity of peak A suggests the C_{60} introduces an additional degree of order at the bilayer interface. Since reflections due to complex **2** appear in the Q region of A while C_{60} reflections do not (Figure 5-8), we anticipate that, under the present conditions, deposition of C_{60} on the HBC surface would result in the formation of some small co-crystalline regions at the interface. This interpretation is supported by the shift of the (111) reflection of C_{60} (peak B) from its nominal position (0.73 $Å^{-1}$) to lower Q (0.7 $Å^{-1}$), toward the co-crystal reflections, for the 3 nm C_{60} film, as well as the width of peak A, which is roughly consistent with a 3 nm interface layer.

To further probe the local electronic and geometric structure of the HBC/C_{60} interface, it was investigated with surface-sensitive X-ray photoelectron (XPS) and near-edge X-ray absorption spectroscopy (NEXAFS). For this experiment, the interface was modeled by

depositing 2 nm C_{60} on a 10 nm HBC film on ITO. The spectral differences between the C_{60} (2 nm)/HBC(10 nm) bilayer and pristine (10 nm) films of either HBC or C_{60} then afforded insight into the unique interaction between the shape complementary donor and acceptor molecules.

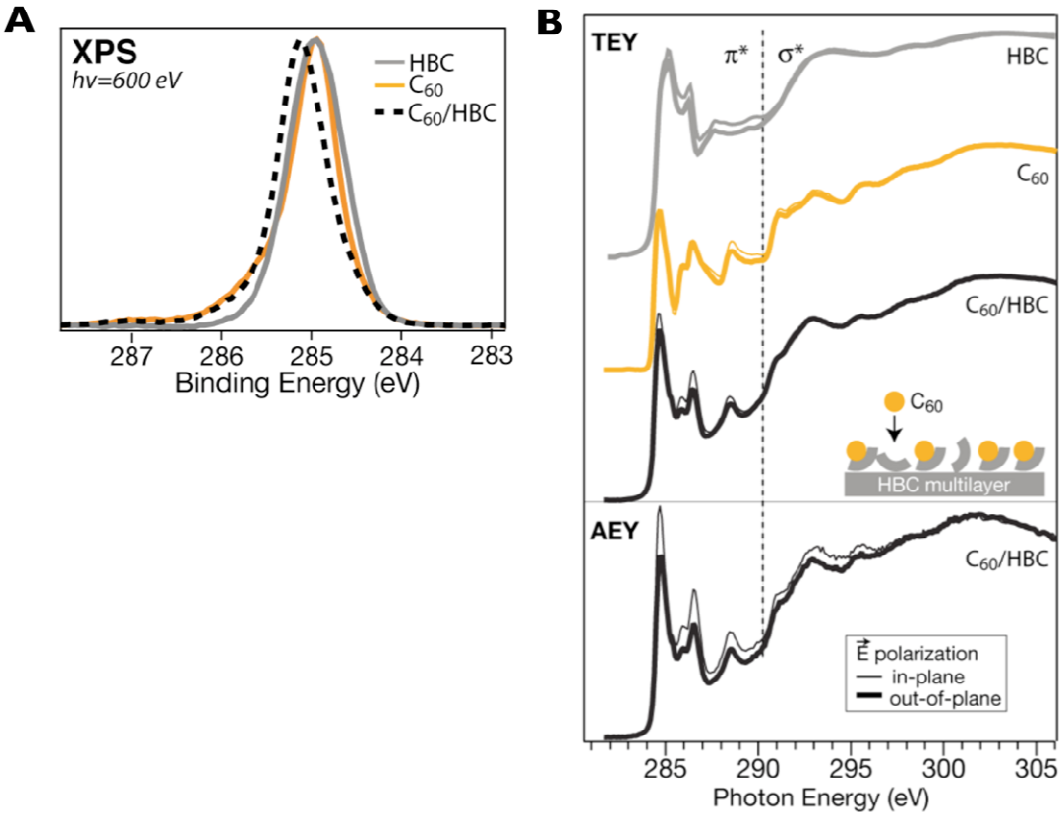

Figure 5-9 (a) C 1s XPS measured at photon energy 600 eV for: C_{60}(10 nm)/ITO (dashed line), HBC (10 nm)/ITO (solid black line), and C_{60}(2 nm)/HBC(10 nm)/ITO. (b) Polarization dependent XAS of HBC(10 nm)/ITO, C_{60}(10 nm)/ITO, and C_{60}(2 nm)/HBC(10 nm)/ITO measured in Total Electron Yield (TEY) mode. The surface-sensitive Auger Electron Yield (AEY) XAS of C_{60}(2 nm)/HBC(10 nm)/ITO is also shown. A schematic of the C_{60}-HBC bilayer interface is inset.

XPS probing the C1s region (Figure 5-9) provides direct evidence for an electronic interaction between C_{60} and HBC in the deposited films. Specifically, relative to the pure HBC and C_{60} films, the bilayers have a shift to higher binding energy by 0.2 eV, a change in peak shape, and a narrowing in peak width. Such features are consistent with charge transfer at donor-acceptor interface, which affects the ability of the system to screen and stabilize the core-ionized final state, thereby altering the shape, width[27] and energy[28–29] of the photoemission peak. This supports the presence of an intimate interaction between the donor and acceptor molecules.

Surface-sensitive, polarization-dependent NEXAFS, shown in Figure 5-9, indicates that the electronic interaction between acceptor and donor is accompanied by a physical ordering of the molecules at the HBC/C_{60} interface. In the total electron yield (TEY) signal, which probes the bulk of the 10 nm films, no polarization dependence is observed, indicating the lack of a preferred molecular orientation in the film. However, an anisotropy in bond geometry is uniquely observed for the HBC/C_{60} bilayer in the Auger electron yield (AEY) signal, which probes the ~1–2 nm near-surface region; that is, the HBC/C_{60} interface. From the polarization dependence of the integrated p* resonances,[28–31] we estimate that the HBC molecules interacting with C_{60} are oriented at an average tilt angle of ~40º with respect to the surface plane. If the HBC ordering is related to a spontaneous assembly of the molecular partners at the bilayer interface into complex **2**, this HBC tilt angle orients the (110) plane of the co-crystal parallel to the surface plane. In this geometry, X-rays diffracted from the (110) plane of complex **2** would contribute intensity confined to the Q_z direction at Q = 0.48 $Å^{-1}$ and thereby explain the increase in peak A in the GIXD data at the HBC/C_{60} interface (Figure 5-8). The data suggests that there is sufficient solid-state and surface

mobility of the molecular partners for coalescence into an ordered state at the interface that can be modeled by the “ball and socket” structure shown in Figure 5-2.

The sequential deposition of the two shape-complementary molecules thus does produce an interface that is at least partially organized. Do the OPVs benefit from this molecular organization? To assess this we tested p-type molecules that lack the doubly-concave distortion from planarity of our HBC but is otherwise very similar. Flat hexa-peri-hexabenzocoronene (*flat*-HBC) is an excellent candidate for comparison to the HBC under investigation (*contorted*-HBC) (Figure 5-10). These two molecules have similar electronic structures, band gaps, molecular weights, chemical formulas, evaporation temperatures, molecular dimensions, and UV/Vis absorption spectra in thin films (Figure 5-6). The most obvious difference between *flat*-HBC and our *contorted*-HBC is shape: one is perfectly flat while the other is severely distorted from planarity. While the *contorted*-HBC is shape-complementary to fullerenes, the *flat*-HBC is not.

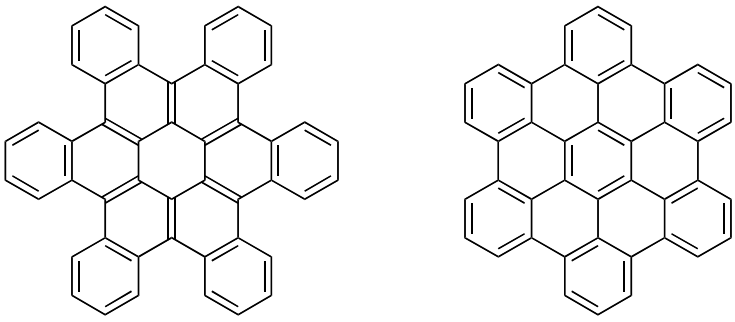

contorted-HBC *flat*-HBC

Figure 5-10 Chemical structures of *contorted*-HBC and *flat*-HBC.

Devices made with the two HBC molecules behaved quite differently under simulated solar irradiation. Devices based on *contorted*-HBC are more efficient than those based on *flat*-HBC (0.55% versus 0.07 %). The former also have higher V_{OC}s than the latter (0.84 V versus 0.19 V, Figure 5-7, Supporting Information). This supports the notion that shape complementarity contributes to the higher V_{OC} values for *contorted*-HBC.

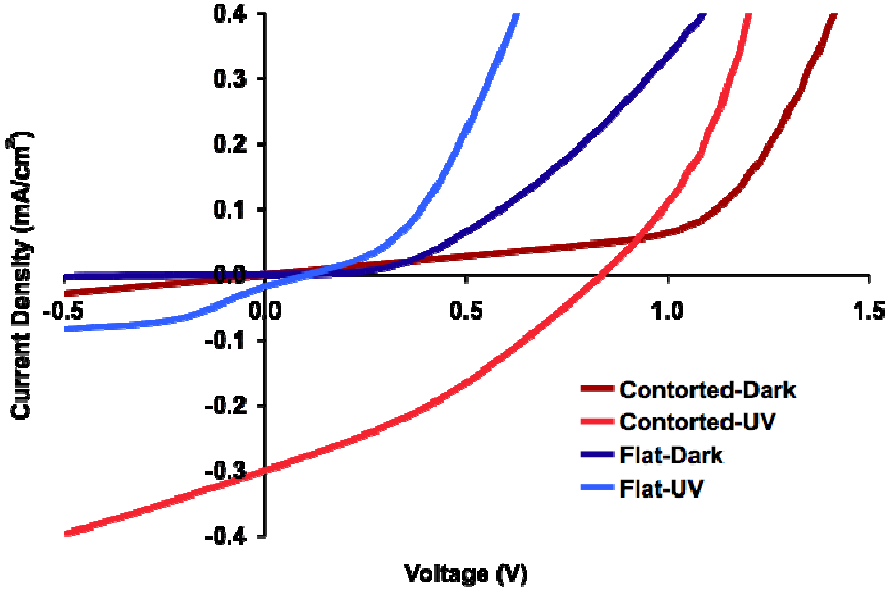

Figure 5-11 Typical *contorted*-HBC/C_{60} device. I-V characteristics compared to those of a *flat*-HBC/C_{60} device when illuminated under a UV LED.

Notably, under UV-LED irradiation, *contorted*-HBC device outperformed *flat*-HBC by more than two orders of magnitude (average efficiencies of η=3.36% versus 0.03 %, Figure 5-11). The emission spectrum of the UV-LED covers the longest-wavelength

absorbance shoulder for thin films of both HBCs (Figures 5-2(c) and 5-11). Although *contorted*-HBC devices had V_{OC}s similar to those of *flat*-HBC devices under solar irradiation, the V_{OC}s of *contorted*-HBC devices were over ten times greater than *flat*-HBC (0.80 V versus 0.07 V) under UV light. These results further support our assertion that the shape-complementary interface is essential for peak device performance.

In summary, we reported that shape complementarity improves the donor/acceptor interface and, consequently, the photovoltaic properties of bilayer OPVs. We showed that *contorted*-HBC forms intimate complexes with the fullerenes. We also showed that differences in complementarity directly translate to differences in OPV performance. Better shape complementary improves the interface between donor and acceptor materials in our devices and leads to some of the highest V_{OC}s reported to date, with a maximum of 0.95 V. We also observe efficiencies of up to 5.7 % in ambient atmosphere for narrow width UV irradiation and 1.04 % for solar illumination. This data indicates that our OPV cells may be ideally partnered with longer wavelength absorbing layers to achieve higher efficiency solar cells.

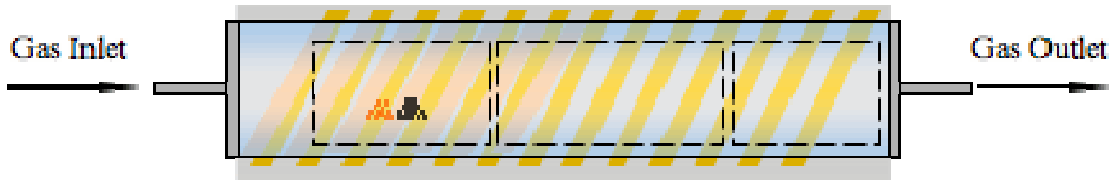

Figure 5-12 Schematic of the HPVT.

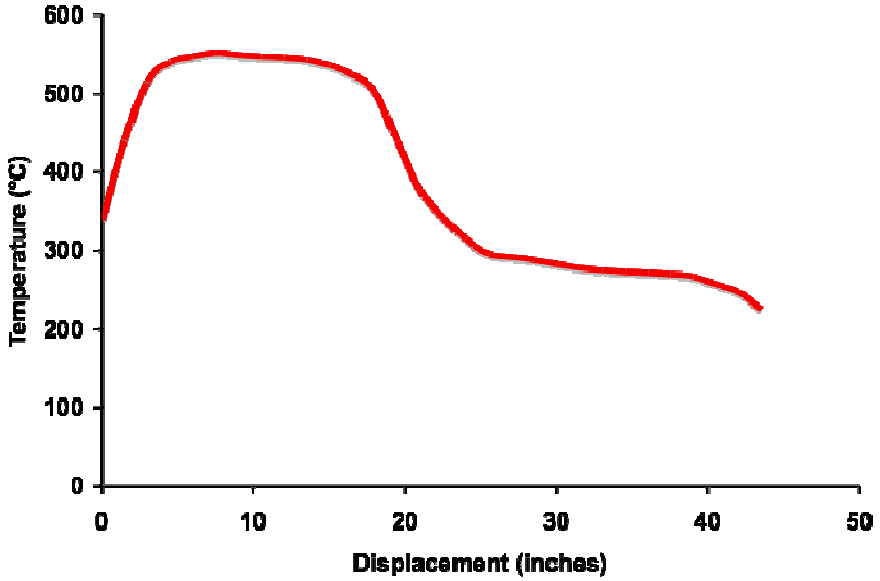

Figure 5-13 The temperature (in degrees Celsius) of the gradient in the quartz tube plotted as a function of displacement along tube (in inches).

Experimental Section

5.1. Synthesis

Contorted hexabenzocoronene and derivatives (*contorted*-HBC) and hexa-peri-hexabenzocoronene (*flat*-HBC) were synthesized according to literature procedures. C_{60} (Catalog No: BU-603; CAS: 99685-96-8) and C_{70} (Catalog No: BU-703; CAS: 115383-22-7) were purchased from BuckyUSA, Inc. Anhydrous chlorobenzene (Catalog No: 284513; CAS:108-90-7) was purchased from Sigma-Aldrich. PEDOT:PSS was purchased under the name Baytron P (Catalog No: 01016141; CAS: 7732-18-5) from H.C. Stark.

5.2. Device fabrication

The thicknesses of all thin films were calibrated via atomic force microscopy of either a masked off edge and/or a stratched film. All thermal depositions were performed under a pressure of ~$1*10^{-6}$ torr at an average rate of ~1.0 Å/sec.

Patterned indium-tin oxide glass substrates were cleaned thoroughly by sonication in acetone and isopropyl alcohol, dried under a stream of nitrogen, and UV-ozone etched for five minutes. PEDOT:PSS was spun at 5000 rpm for 60 seconds and the film was subsequently baked at 200 °C for 30-45 minutes. The unmodified c*ontorted*-HBC or *flat*-HBC were thermally evaporated to a thickness of 25 nm. Solution processable HBC derivatives were spincoated from a 2 -4 mg/mL toluene solution at 1000 rpm. Either C_{60} or C_{70} was then thermally evaporated to a thickness of ~ 40 nm. The substrates were taken out of ultra-high vacuum (UHV) and moved to a nitrogen atmosphere where they were masked and placed under UHV again. Aluminum was deposited to a thickness of ~ 60 nm.

5.3. Electrical measurements

Finished devices possessed an area of 0.16 cm^2. They were moved to ambient atmosphere and measured with Keithley 2602/2400 sourcemeters under both dark conditions and under illumination with a solar simulated lightsource. Ultra-violet light emitting diodes (LED) were from NEBO™. All illumination sources were calibrated using a silicon photodiode.

5.4. Light-emitting diode calibration

The optical power of the UV source was measured with a silicon photodiode. Light was incident on the detector, and the current induced was recorded. The area of the photodetector was 1 cm^2 yielding units of A/cm^2. The spectrum of the light source was then taken using a spectrometer and this spectrum was normalized (to set the integral to unity) and point-wise multiplied by the responsivity curve of the photodetector to compensate for nonlinearities in the current response. The resulting integration is the power conversion factor for the light source, in Watts/Amp. This value directly converts the previous photovoltaic response to the optical power of the light source.

5.5. Growth of complex 1

Saturated solutions of C_{60} and HBC in chlorobenzene were combined (5 mL each) and the resulting mixture was allowed to sit in an unsealed small vial sealed within a larger container. Long purple-gray needles (1-3 mm) formed within three weeks, with minimal evaporation of chlorobenzene (<10%).

5.6. Growth of complex 2

Complex **2** crystals were grown using horizontal physical vapor transport (HPVT), as shown in Figure 5-11. A quartz tube was wrapped with heating coils such that it had a temperature gradient. This gradient was measured prior to crystal growth (Figure 5-12). The HBC and C_{60} powders were placed 5-8 inches apart in the hottest region of the furnace. By flowing ultra-high-purity argon carrier gas through the furnace, crystals grew in the colder region of the furnace (330 °C).

5.7. Single-crystal electrical measurements

Silver contacts (100nm thickness) were deposited on crystals of complex **1** by using a thermal evaporator to form two electrodes with a 300μm gap between them. Steady state current was measured with a Keithley 6517A. In order to minimize transient currents, a bias voltage was applied for ten seconds before each current measurement. Sheet resistance at various temperatures was evaluated in order to extract activation energies. All measurements were performed in vacuum.

5.8. General crystal structure analysis

Distance measurements and images from the crystal structures of complexes **1** and **2** were generated using CrystalMaker™ 7.2. Close contacts were obtained by measuring the distance between two carbon nuclei on adjacent molecules. The π-π distances between HBC and C_{60} were calculated by creating a plane between the three sp^2-carbons in HBC closest to C_{60}, measuring the distance between that plane and the center of C_{60}, and then subtracting the calculated radius of that C_{60}. The radius of each C_{60} was calculated by taking the mean

distance of each carbon to the center of the molecule.

5.9 π-π distsance calculation

An example of a π-π distance calculation is shown in Figure 5-13. A plane was generated through the three carbons on HBC closest to C_{60} (in this case it was three from the center six-membered ring on HBC). All carbons of the C_{60} were selected and a centeroid was calculated (labeled Zz, Figure 5-13). A distance of 6.439 Å was found from that centroid to the plane, centered directly on the six-membered ring. A mean nuclear radius of that C_{60} was generated as part of the centroid calculation output (3.5139 Å). To get the π-π distance (2.93 Å), the mean radius was subtracted from the center-to-plane distance (6.439 – 3.514 = 2.925). To find the π-π distance between the two C_{60}'s in complex **1**, **2** mean radii (10.008 - 2 x 3.5139 = 2.98 Å) were subtracted from the distance between the two C_{60} centroids.

5.10. Sample preparation for Grazing IncidenceX-ray diffraction

Samples were prepared by cutting silicon wafers (with native oxide) to a size of approximately 1 X 1 cm. Silicon substrates were cleaned by sonication in acetone and isopropyl alcohol followed by drying in a stream of nitrogen gas. HBC was thermally evaporated to a thickness of 25 nm using the same deposition conditions as for the photovoltaic devices. Subsequently, C_{60} layers of various thicknesses were evaporated onto the silicon substrates. All samples were made in duplicate to ensure consistency. Samples were packaged within two sealed mylar bags under a nitrogen atmosphere and then shipped to the Stanford Synchrotron Radiation Lightsource (SSRL), where the measurements were performed.

5.11. Grazing-incidence X-ray diffraction measurements

Grazing Incidence X-ray Diffraction (GIXD) measurements were performed at the Stanford Synchrotron Radiation Lightsource on beam line 11-3 at a photon energy of 12.7 keV. The incident x-ray beam, k_{in}, has a grazing incidence angle with the sample surface. A 2D MAR345 image plate detector (pixel size 0.15 mm), positioned a distance L from the sample, records the scattered beam, k_{out}. This is converted into an image of the reciprocal space (Q-space) with the scattering expressed as a function of the scattering vector $Q=k_{out}-k_{in}$. Here, the sample-to-detector distance L, calibrated with a LaB_6 polycrystalline standard, was 398.6 mm. The incidence angle was chosen as 0.1°, slightly above the critical angle for total external reflection from the organic film surface. This reduces any background scattering from the substrate and gives a large diffracting volume. The samples were kept under a helium atmosphere during measurement to minimize damage to the films from the intense x-ray beam and eliminate X-ray scattering from air. A linear background, defined by regions before and after the diffraction peaks, was subtracted from the reciprocal space map. A dark (blank) image scan was also subtracted from the measurements to help isolate weaker signals from the samples.

5.12 Sample Preparation for X-ray Photoelectron (XPS) and X-ray Absorption Spectroscopy (XAS)

Samples were prepared by cutting indium tin oxide (ITO) to a size of approximately 12 mm X 5 mm. ITO substrates were cleaned by sonication in acetone and isopropyl alcohol followed by drying in a stream of nitrogen gas. Pure films of HBC and C_{60}, respectively, were thermally evaporated to a thickness of 10 nm on the ITO using the same deposition conditions

as for the photovoltaic devices. To model the C_{60}-HBC interface, 2 nm of C_{60} was deposited on separate 10 nm HBC films, prepared under the same conditions. All samples were made in duplicate to ensure consistency. Samples were packaged within two sealed mylar bags under a nitrogen atmosphere and transported to the Stanford Synchrotron Radiation Lightsource (SSRL), where the measurements were performed.

5.13. XPS and XAS Measurements

C 1s XPS and XAS measurements were performed at the Stanford Synchrotron Radiation Lightsource on beam line 13-2. Beamline 13-2 has a spherical grating monochromator and an energy range of 250-1100 eV, and the focused beam has a spot size of 0.01 x 0.075 mm^2. It is equipped with an elliptically polarizing undulator (EPU) that can be used in three different polarization modes: elliptical, horizontal and vertical; circular polarization was accomplished by summing spectra for elliptical polarization with opposite elliptical distortion. The BL13-2 station is designed for surface and solid state experiments with ultra-high vacuum compatible samples up to 10 mm in diameter. The main chamber has an electron spectrometer (SES-R3000, VG-Scienta) for photoemission spectroscopy and X-ray absorption spectroscopy.

XAS spectra were simultaneously measured in both total (TEY) and Auger electron yield (AEY) modes. The reference absorption intensity (I_0) of the incoming x-ray beam, measured on a gold coated mesh positioned just after the refocusing optics, was measured simultaneously and used to normalize the spectra to avoid any artifacts due to beam instability. TEY was obtained by the sample drain current (sampling depth > 5nm). In AEY mode, the electron spectrometer was tuned to a kinetic energy window of 230-240 eV was chosen

obtaining information restricted to the near-surface (~1-2 nm) region. All spectra were recorded in the photon energy range 280-310 eV with energy resolution better than 100 meV. The energy scale was calibrated using photoemission lines of a reliable peak from the second and third order diffracted photon, here the C1s of our C_{60} reference sample. The spectra were normalized by fitting the data points before the absorption edge by a straight line taken as zero, and normalizing the maximum intensity of the s* resonance (at ~300 eV) to 1.

XPS spectra were measured with energy resolution better than 100 meV. The XPS binding energy scale spectra taken at photon energy 600 eV was shifted 2.3 eV to higher binding energy; using the calibrated shift between the monochromator at 310 eV and actual energy (determined by higher order photoemission lines of the C_{60} C1s peak).

References for Chapter 5

[1] Lloyd, M. T.; Anthony, J. E.; Malliaras, G. G. *Materials Today* **2007**, *10*, 34–41.

[2] Dennler, G.; Scharber, M. C.; Ameri, T.; Denk, P.; Forberich, K.; Waldauf, C.; Brabec, C. J. *Adv. Mater.* **2008**, *20*, 579 –583.

[3] Thompson, B. C.; Fréchet, J. M. J. *Angew. Chem.* **2008**, *120*, 62– 82; *Angew. Chem. Int. Ed.* **2008**, *47*, 58– 77.

[4] Yu, G.; Gao, J.; Hummelen, J. C.; Wudl, F.; Heeger, A. J. *Science* **1995**, *270*, 1789 – 1791.

[5] Kim, J. Y.; Lee, K.; Coates, N. E.; Moses, D.; Nguyen, T. Q. *Science* **2007**, *317*, 222– 225.

[6] Wenger, S.; Seyrling, S.; Tiwari, A. N.; Grätzel, M. *Appl. Phys. Lett.* **2009**, *94*, 173508/1 –173508/3.

[7] Tang, C. *Appl. Phys. Lett.* **1986**, *48*, 183 –185.

[8] Kennedy, R. D.; Ayzner, A. L.; Wanger, D. D.; Day, C. T.; Halim, M.; Khan, S. I.; Tolbert, S. H.; Schwartz, B. J.; Rubin, Y. *J. Am. Chem. Soc.* **2008**, *130*, 17290 – 17292.

[9] van Herrikhuyzen, J.; Syamakumari, A.; Schenning, A.; Meijer, E. *J. Am. Chem. Soc.* **2004**, *126*, 10021–10027.

[10] Yang, X.; Loos, J. *Macromolecules* **2007**, *40*, 1353– 1362.

[11] Schmaltz, B.; Weil, T.; Mullen, K. *Adv. Mater.* **2009**, 21, 1067 – 1078.

[12] Xiao, S.; Miao, Q.; Sanaur, S.; Pang, K.; Steigerwald, M. L.; Nuckolls, C. *Angew. Chem.* **2005**, *117*, 7556 – 7560; *Angew. Chem. Int. Ed.* **2005**, *44*, 7390 –7394.

[13] Xiao, S.; Tang, J.; Beetz, T.; Guo, X.; Tremblay, N.; Siegrist, T.; Zhu, Y.; Steigerwald, M. L.; Nuckolls, C. *J. Am. Chem. Soc.* **2006**, *128*, 10700 –10702.

[14] Guo, X.; Myers, M.; Xiao, S.; Lefenfeld, M.; Steiner, R.; Tulevski, G. S.; Tang, J.; Baumert, J.; Leibfarth, F.; Yardley, J. T.; Steigerwald, M. L.; Kim, P.; Nuckolls, C. *Proc. Natl. Acad. Sci. USA* **2006**, *103*, 11452 –11456.

[15] Guo, X.; Xiao, S.; Myers, M.; Miao, Q.; Steigerwald, M. L.; Nuckolls, C. *Proc. Natl. Acad. Sci. USA* **2009**, *106*, 691–696.

[16] Cohen, Y.; Xiao, S.; Steigerwald, M. L.; Nuckolls, C.; Kagan, C. *Nano Lett.* **2006**, *6*, 2838 –2841.

[17] Wang, Z.; Dötz, F.; Enkelmann, V.; Müllen, K. *Angew. Chem. Int. Ed. Angew. Chem. Int. Ed.* **2005**, *44*, 1247 –1250.

[18] Pham, D.; Ceron-Bertran, J.; Olmstead, M. M.; Mascal, M.; Balch, A. L. *Cryst. Growth Des.* **2007**, *7*, 75– 82.

[19] Konarev, D. V.; Khasanov, S. S.; Otsuka, A.; Saito, G.; Lyubovskaya, R. N. *J. Am. Chem. Soc.* **2006**, *128*, 9292 –9293.

[20] Atwood, J. L.; Barbour, L. J.; Heaven, M. W.; Raston, C. L. *Angew. Chem*. **2003**, *115*, 3376 –3379; *Angew. Chem. Int. Ed.* **2003**, *42*, 3254– 3257.

[21] Laudise, R. A.; Kloc, C.; Simpkins, P. G.; Siegrist, T. *J. Cryst. Growth* **1998**, *187*, 449–454.

[22] Dorset, D. L.; McCourt, M. P. *Acta Crystallogr. A* **1994**, *50*, 344– 351.

[23] David, W. I. F.; Ibberson, R. M.; Matthewman, J. C.; Prassides, K.; Dennis, T. J. S.; Hare, J. P.; Krote, H. W.; Taylor, R.; Walton, D. R. M. *Nature* **1991**, *353*, 147–149.

[24] Peet, J.; Senatore, M.; Heeger, A. J.; Bazan, G. *Adv. Mater.* **2009**, *21*, 1521 –1527.

[25] Average UV LED data: efficiency = 3.4 %; J_{sc} = 0.16 mAcm^2 ; V_{oc}=0.80 V; FF=0.23.

[26] Mayer, A. C.; Toney, M. F.; Scully, S. R.; Rivnay, J.; Brabec, C. J.; Scharber, M.; Koppe, M.; Heeney, M.; McCulloch, I.; McGehee, M. D. *Adv. Funct. Mater.* **2009**, *19*, 1173–1179.

[27] Nilsson, A.; Tillborg, H.; Martensson, N. *Phys. Rev. Lett.* **1991**, *67*, 1015 – 1018.

[28] Polzonetti, G.; Battocchio, C.; Goldoni, A.; Larciprete, R.; Carravetta, V.; Paolesse, R.; Russo, M. V. *Chem. Phys.* **2004**, *297*, 307– 314.

[29] Vilmercati, P.; Castellarin Cudia, C.; Larciprete, R.; Cepek, C.; Zampieri, G.; Sangaletti, L.; Pagliara, S.; Verdini, A.; Cossaro, A.; Floreano, L.; Morgante, A.; Petaccia, L.; Lizzit, S.; Battocchio, C.; Polzonetti, G.; Goldoni, A. *Surf. Sci.* **2006**, *600*, 4018 – 4022.

[30] Stchr, J. in *NEXAFS Spectroscopy.* Springer-Verlag, Berlin, **1982**, p. 275 – 291.

[31] DeLongchamp, D. M.; Lin, E. K.; Fischer, D. in *Organic Field-Effect Transistors IV*, edited by Bao Z. and Gundlach, D. J. *Proc. of SPIE* **2005** *Vol. 5940*, 59400 A1– 5.

Chapter 6

UNUSUAL MOLECULAR CONFORMATIONS IN FLUORINATED, CONTORTED HEXABENZOCORONENES*

* Part of this chapter was reproduced with permission from *Organic Letters*:

"Unusual Molecular Conformations in Fluorinated, Contorted Hexabenzocoronenes" by Yueh-Lin Loo, Anna M. Hiszpanski, Bumjung Kim, Sujun Wei, Chien-Yang Chiu, Michael L. Steigerwald, and Colin Nuckolls.

*My contribution on this study was mainly focused on crystal growth of fluorinated HBC series. Synthesis and NMR analysis of HBCs were done by Dr. Yueh-Lin Loo.

6.1 Background

Hexabenzocoronenes (HBCs) have attracted significant scientific attention given their interesting electronic and self-assembly properties. Both planar and contorted HBCs, for example, have been incorporated as active layers in organic thin-film transistors; devices comprising unsubstituted planar HBC[1] and dodecyloxy-substituted contorted HBC[2] exhibit hole mobilities of order 10^{-2} cm^2/Vs. These materials also have a strong tendency to self assemble into supramolecular structures; both planar and contorted HBCs readily pack in a columnar fashion to generate nanorods and wires affording field-effect transistors.[1-3] Unlike planar HBCs, whose structures resemble small sections of grapheme, the molecular conformation of contorted HBCs is distorted from planarity by 20° on its periphery due to steric congestion between the proximal C-H bonds. This doubly concave conformation can thus provide unique opportunities for complexation with geometrically complementary compounds, such as C_{60}.[4]

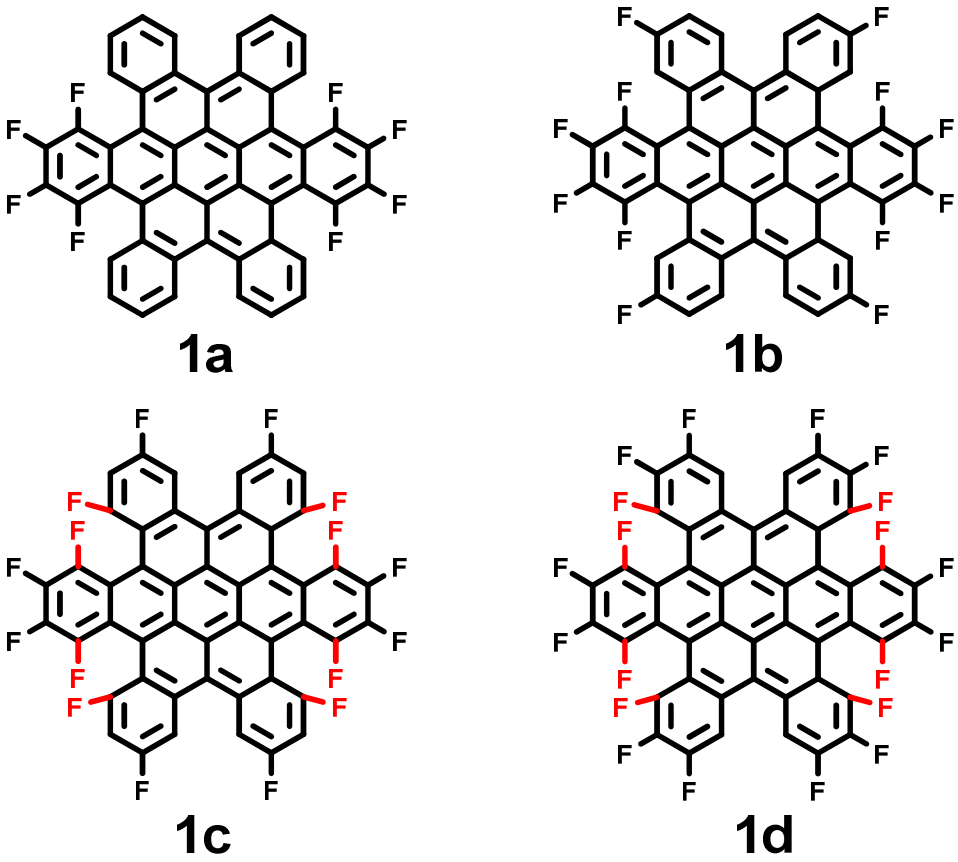

Figure 6-1 Chemical structures of 8F- (**1a**), 12F- (**1b**), 16F- (**1c**), and 20F-HBC (**1d**). Close fluorine-fluorine intramolecular contacts (< 2.6 Å) are highlighted in red for **1c** and **1d**.

The addition of fluorenyl units[5] and oligothiophenes[6] at the peripheral aromatic rings of planar and contorted HBCs, respectively, has been shown to alter the optical absorbance and the HOMO and LUMO energy levels of the parent compound in addition to improving the molecular packing in the solid state. In the same vein, select fluorination of the outer aromatic rings of planar HBC is found to enhance the molecule's electron withdrawing nature;[7] fluorinated planar HBC is reported to transport electrons with a mobility of 10^{-2} cm^2/Vs.[8] More interestingly, this compound is shown to adopt a face-to-face type packing motif in the solid state rather than the herringbone structure that is found in its parent

compound due to the larger van der Waals radius of fluorine.[8] Inspired by the work of Mori et al.,[8] we wanted to examine the influence of fluorine-fluorine intramolecular interactions on the molecular conformation of contorted HBCs given their already-unusual doubly-concave conformation.

6.2 Synthesis of Fluorinated Hexabenzocoronenes

In this study, we report the synthesis and characterization of a series of contorted HBCs with differing amounts of fluorination on its exterior aromatic rings.[9] Functionalized contorted HBCs have been previously realized via double Barton-Kellogg reactions of the appropriate pentacenequinones followed by photocyclization or Scholl cyclization.[10] The synthetic scheme used here is different than those employed in the past and is shown in Scheme 6-1. We carried out a double Corey-Fuchs[11] reaction on fluorinated pentacenequinone to provide a precursor to the fluorinated, contorted HBCs shown in Figure 6-1. This reaction yields a tetrabrominated intermediate, **2**. Subjecting **2** to a Suzuki-Miyaura[12] reaction with the appropriate fluorinated phenyl boronic acid (**3a-d**) yielded the desired bisolefin compound, **4a-d**. We then employed the Katz-modified Mallory photocyclization[13,14] on **4a-d**; the products from these reactions consisted of a mixture of half-cyclized and fully-cyclized HBCs (**1a-d**). Given the solubility differences between the half- and fully-cyclized HBCs, we isolated the half-cyclized products and imposed upon them Scholl cyclizations per Plunkett et al.[9] to yield the fully cyclized products **1a′ -d′** . Given the wide availability of functionalized phenyl boronic acids, this route brings about tremendous flexibility and modularity to the synthesis of contorted HBCs with different substitution.

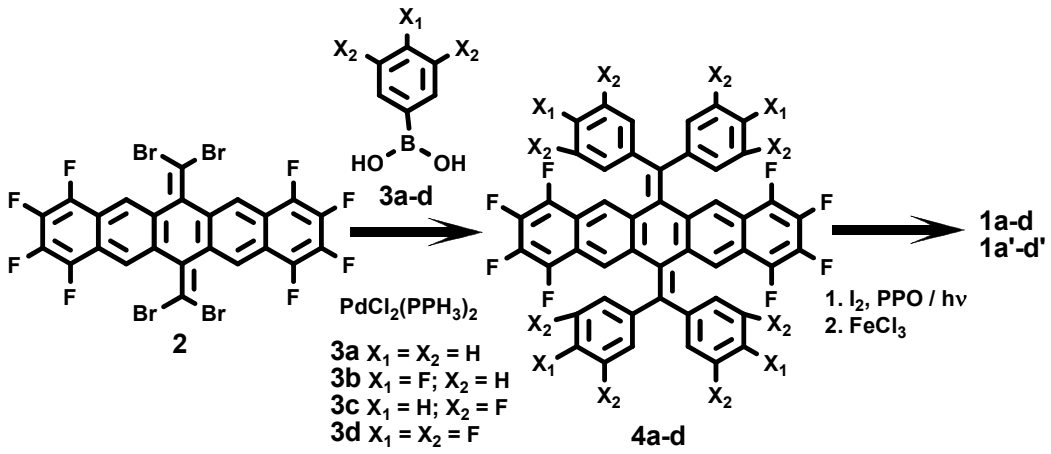

Scheme 6-1 General strategy for synthesizing fluorinated, contorted HBCs.

Examination of single crystals of **1a-d** by X-ray Crystallography indicates that the fluorinated, contorted HBCs that result from photocyclization adopt molecular conformations that are not significantly different from that of their hydrogen-substituted counterpart. They adopt, for example, the doubly concave conformation that characterizes contorted hexabenzocoronenes.[2-4] At first blush, it thus appears that substituting hydrogens with fluorines on the peripheral aromatic rings of contorted HBCs does not affect their molecular conformations.

The 1H NMR spectrum of 8F-HBC obtained upon Scholl cyclization (**1a′**) is in all respects identical to that of 8F-HBC obtained after photocyclization (**1a**), indicating that **1a′** and **1a** are chemically and conformationally indistinguishable. We found this observation to hold true for 12F-HBC also. This observation, however, does not hold true for 16F-HBC or 20F-HBC, both of which have close intramolecular fluorine-fluorine contacts (<2.6 Å). The NMR spectra of 16F-HBC obtained after photocyclization (**1c**) and after Scholl cyclization

(**1c′**) are shown in Figure 6-2. We observe two sets of resonances associated with the two proton environments in 16F-HBC. The triplet at 7.4 ppm in the NMR spectrum of **1c** is assigned to the protons on the peripheral aromatic rings that are sandwiched between fluorine substituents on the same rings. The doublet at 8.7 ppm is attributed to the less shielded protons of 16F-HBC. Integrating the proton resonances confirms equal contributions to the NMR spectrum of 16F-HBC. The NMR spectrum of **1c′** appears to be similar to that of **1c**, but both the triplet and the doublet in the spectrum of **1c′** are shifted downfield relative to those of **1c** at the same concentrations. Comparison of the placement of the proton resonance of the reference solvent (tetrachloroethane; δ = 6.0 ppm) indicates that this downfield shift seen in the spectrum of **1c′** is not an experimental artifact; rather, it reflects real differences in the molecular conformations of **1c** and **1c′**. We have also carried out NMR experiments on mixtures of **1c** and **1c′**; both sets of resonances are present, further confirming that the differences in chemical shifts stem from differences in molecular conformations.

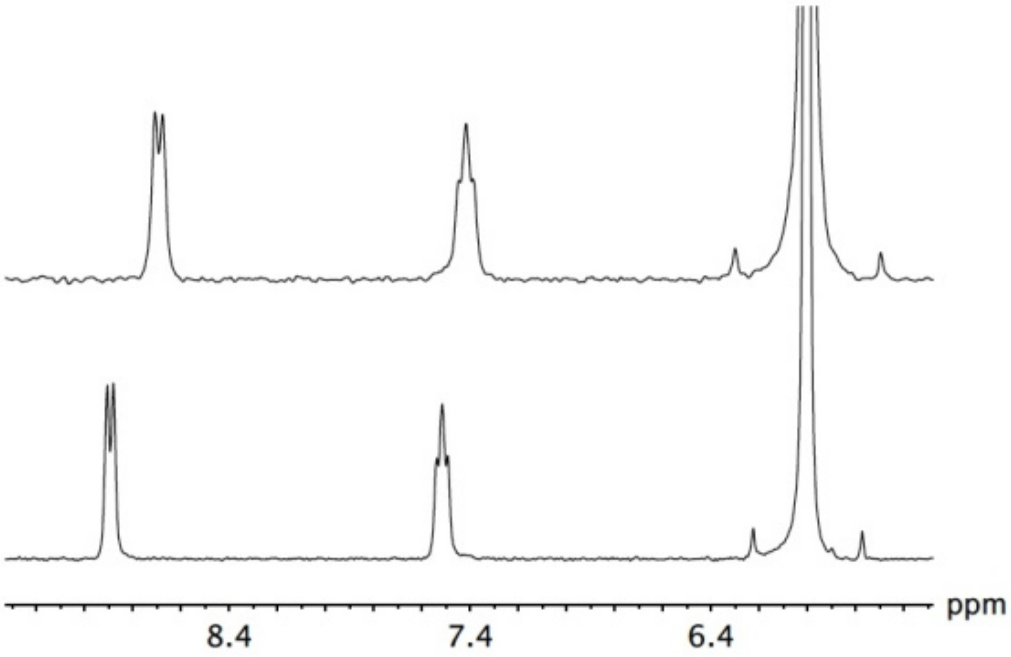

Figure 6-2 1H NMR spectra of **1c** (top) and **1c′** (bottom). The spectra have been corrected against the reference peak of tetrachloroethane at 6.00 ppm.

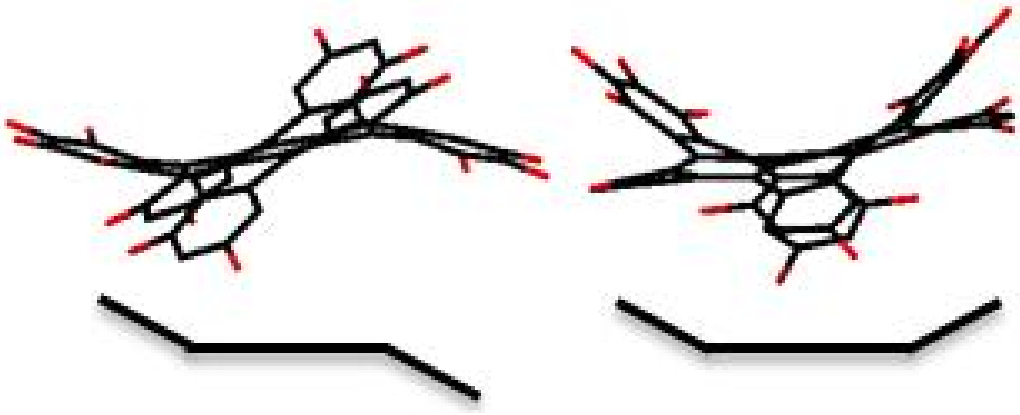

Figure 6-3 Side view of **1c** (left) and **1c′** (right) based on x-ray crystallography. Fluorine is depicted in red. Hydrogens have been removed for clarity. The stick figures below illustrate the conformations of the ring planes originating from the fluorinated pentacenequinone precursor.

Figure 6-3 shows the molecular conformations of **1c** and **1c′** observed in the crystal structure of each. We observe that the outer aromatic rings in **1c** alternate into and out of the plane defined by the core aromatic rings, resulting in a doubly concave structure that is similar to those exhibited by other contorted HBCs.[2-4] The molecular conformation of **1c′**, on the other hand, has not previously been observed. In particular, the perfluorinated outer aromatic rings originating from fluorinated pentacenequinone are contorted out of the plane defined by the core aromatic rings in the same direction, resulting in a saddle-like conformation (see the molecular models in Figure 6-3 for comparison of the positions of the outer aromatic rings originating from the fluorinated pentacenequinone precursor). The exterior aromatic rings introduced by coupling with **3c** are displaced in the opposite direction, presumably to minimize close fluorine-fluorine intramolecular contact (highlighted in red for 16F-HBC in Figure 6-1). In the solid state, both **1c** and **1c′** adopt monoclinic crystal structures having the $P2_1/C$ space group with slightly different unit cell dimensions.[15]

Minimization of free energy of these molecular conformations via density functional theory (DFT) calculations indicates that the armchair structure of **1c** depicted in the left of Figure 6-3 sits at a lower energy compared to the saddle structure of **1c′** (right of Figure 6-3). Indeed, variable temperature NMR experiments carried out on **1c′** indicates that heating above 100 °C induces a transformation in molecular conformation to that adopted by **1c**. This transformation is irreversible; cooling to room temperature does not allow reversion back to its original conformation.

6.3 NMR analysis

To quantitatively examine the transformation from the metastable conformation of **1c′** to that of **1c**, we monitored the kinetics of this process isothermally via NMR. Figure 6-4 contains sequential NMR spectra collected of **1c′** at 110 °C in 5 min intervals. As time progresses, we observe a steady increase in the intensities of the proton resonances associated with **1c**; this increase occurs concomitantly with a decrease in intensity of the original proton resonances associated with **1c′** . In fact, collapsing the spectra in Figure 6-4 reveals an isosbestic point at 7.47 ppm indicating that one species is converting into another. The conversion from the metastable to stable conformations is complete after 85 minutes. We also tracked the growth of the proton resonances associated with the more stable conformation; this quantity is plotted in Figure 6-5 for isothermal transformation at 110 °C. The data are well described by first-order kinetics; fitting yields a rate constant of 0.0004 s^{-1}, or a characteristic half time of 1700 s. Fitting the rate constants obtained at several temperatures to the Arrhenius equation yielded an energy barrier of 39 kcal/mol for this transformation. Given that the gauche-to-trans transformation of C-C bonds is estimated to require 3-6 kcal/mol,[16] an energy barrier of 39 kcal/mol seems reasonable for the transformation between the two conformations of 16F-HBC given the significant rearrangement of C-C bonds that needs to take place.

We note that the fully cyclized 20F-HBC product upon photocyclization (**1d**) adopts a molecular conformation that resembles that of **1c** and those of prior contorted HBCs. The Scholl cyclized product of **1d′** , akin to **1c′** , adopts a molecular conformation that is less stable than that of **1d**, and undergoes transformation back to the more stable form on heating. Examining the chemical structures of 16F- and 20F-HBC, we notice that both compounds

share close fluorine-fluorine intramolecular contacts (highlighted red in Figure 6-1). We believe it is the steric hindrance between adjacent fluorinated aromatic rings during ring closure that gives rise to the different molecular conformations.[17] During photocyclization, the bisolefin intermediates **4a-d** first undergo half-cyclization before complete ring closure. Given the numerous degrees of rotational freedom of the Suzuki-Miyaura intermediates, the half-cyclized species are likely to sample a number of conformations. We speculate that only conformations having minimal steric hindrance between fluorines on adjacent aromatic rings are capable of complete ring closure during photocyclization. Ring closure of the remaining half-cyclized species – due to additional fluorine-fluorine steric hindrance – only occurs during the more energetic Scholl cyclization. This hypothesis is consistent with our observation that photocyclization always yields a mixture of half- and fully-cyclized fluorinated, contorted HBCs. Extending the photocyclization reaction does not further convert the half-cyclized product into the final product.

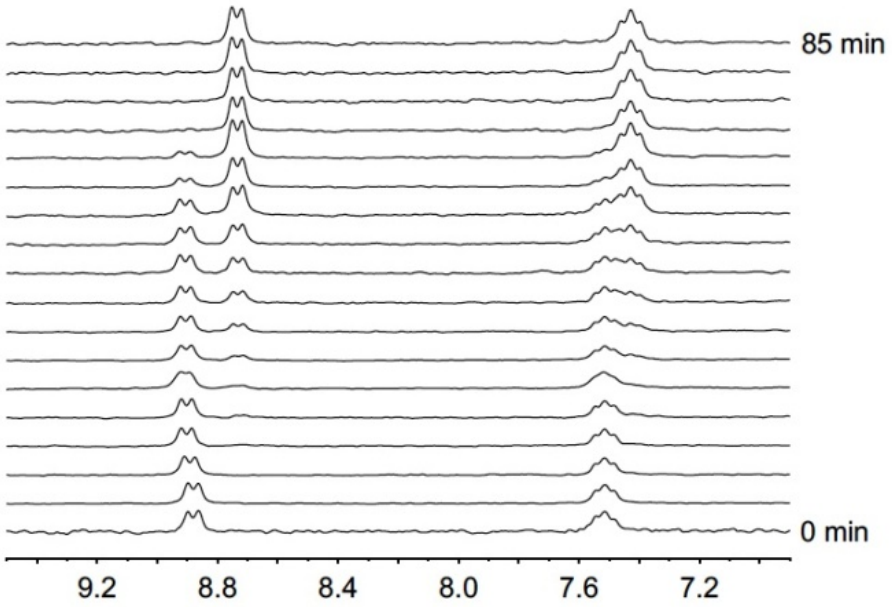

Figure 6-4 NMR spectra acquired in 5 minute intervals during isothermal transformation of 1c' at 110 °C.

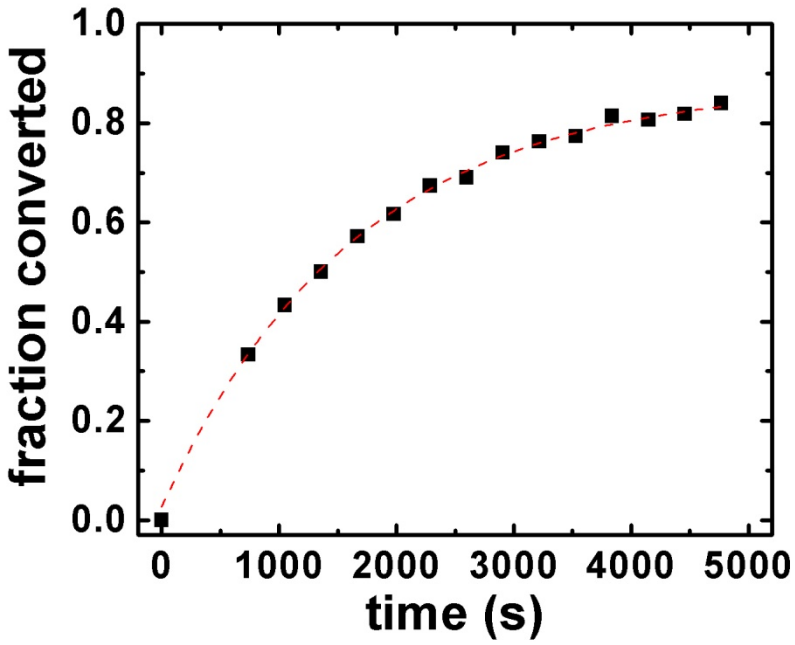

Figure 6-5 Rate of transformation from the metastable to the stable conformation of **1c′** at 110 ºC. The red line represents the first-order fit to the data.

In summary, we have demonstrated a facile and modular method for synthesizing contorted HBC having varying extents of fluorination. Close fluorine-fluorine intramolecular contact results in a metastable molecular conformation not previously observed. Our study highlights the intricacies of fluorine substitution and hints at the possibility of accessing unusual and metastable molecular conformations through fine tuning of intramolecular steric hindrance.

Experimental Section

6.1. General information

Carbon tetrabromide, triphenylphosphine, potassium carbonate, bis(triphenylphosphine)palladium(II) dichloride, fluorinated phenyl boronic acids, iodine, iron (III) chloride, and iodine were obtained from Sigma Aldrich. 1,2,3,4,8,9,10,11-octafluoro-6,13-pentacene quinone was prepared according to literature. All reactions were run in oven-dried glassware (130 ^{o}C), and monitored by TLC using silica gel 60 F_{254} pre-coated plates (EM Science). Anhydrous and oxygen-free solvents were obtained from a Schlenk manifold system with purification columns packed with activated alumina and supported copper catalyst (Glass Contour). Column chromatography was performed on a CombiFlash® Rf system using RediSepTM normal phase silica columns (ISCO, Inc.). ^{1}H and ^{13}C NMR spectra were recorded on Bruker DRX spectrometers at room temperature (unless otherwise noted) operating at 300, 400, and 500 MHz for ^{1}H NMR and 126 MHz for ^{13}C NMR. All peaks are reported as δ ppm. ^{13}C NMR could not be obtained for **1a-d** and **1a'-d'** due to low solubility of the materials. HRMS were recorded on JEOL JMS-HX110A/110A Tandem mass spectrometer. The photochemistry was carried out according to previously reported procedures.

6.2. Synthesis of 6,13-bis(dibromomethylene)-1,2,3,4,8,9,10,11-octafluoro-6,13-dihydropentacene (2).

Carbon tetrabromide (879.6 mg, 2.65 mmol) and triphenylphosphine (1.391 g, 5.30 mmol) were added in a 50 mL roundbottom flask, which was then closed with a rubber

septum. Upon their addition, the white solids began to turn yellow. Approximately 10 mL toluene was added to the solids and stirred at room temperature for 10 minutes during which time white solids precipitated from the mixture. 1,2,3,4,8,9,10,11-octafluoro-6,13-pentacene quinone (300 mg, 0.664 mmol) was added to the flask, causing the color to change to brown, and the solution was left stirring overnight at 80°C. The mixture was filtered—washing with toluene—and toluene was removed from the filtrate by rotary evaporation. The remaining solids were dissolved in a minimal amount of DCM. **2** was precipitated from the solution by the addition of approximately 50 mL methanol and isolated using a Millipore vacuum filtration apparatus, yielding 433 mg (84%) of a beige-pink solid. ^{1}H NMR (400 MHz, CD_2Cl_2) δ 8.56 (s). ^{13}C NMR (126 MHz, $C_2Cl_4D_2$) δ 143.34 – 141.02 (dm, J = 256.7 Hz), 139.62 – 137.20 (dm, J = 269.2 Hz), 137.47 (s), 134.24 (s), 119.73 (s), 118.20 – 117.81 (m), 94.09 (s). HRMS calculated for $C_{24}H_4Br_4F_8$: 759.6919 found: 759.6900.

6.3. General procedure for Suzuki-Miyaura coupling of fluorinated-phenylboronic acids (4a-d).

2 (146 mg, 0.191 mmol), potassium carbonate (845.3 mg, 6.116 mmol), bis(triphenylphosphine)palladium(II) dichloride (20.12 mg, 0.029 mmol), and phenyl boronic acid **(3a)** (126.5 mg, 0.956 mmol) were added together in a nitrogen-purged, 100 mL, two-neck roundbottom flask attached to a condenser and capped with a rubber septum. Distilled water (1.7 mL to make 2 mol K_2CO_3 solution) and THF (6.7 mL, 4 times the volume of water) were added, and the clear yellow mixture was left stirring and refluxing at 70 °C overnight. The reaction was stopped when **2** was consumed (verified by TLC hexanes/DCM 3:1) and the solution had become brown. The product was then extracted with dichloromethane, separated

from the aqueous phase, washed with brine solution, and extracted with dichloromethane and separated again. The organic phase was then dried over $MgSO_4$, filtered, and purified using flash column chromatography (hexane/DCM 3:1) to isolate 94 mg (65%) of **4a.**

6.4. General procedure for photocyclization.

In approximately 20 mL of benzene, 94 mg (0.125 mmol) of **4a** was dissolved by sonication and heating, yielding a clear solution with a yellow tint. The solution was added into the photoreaction glassware with an additional ~500 mL benzene. After 15 minutes of purging the reaction vessel with nitrogen, iodine (190 mg, 0.749 mmol) and 20 mL of propylene oxide were added, making the solution purple. The UV lamp was turned on and the reaction proceeded with a nitrogen purge until the solution became yellow and **4a** was depleted (confirmed by TLC hexanes/DCM 3:1). Silica gel chromatography typically indicated the presence of two products under λ = 254 nm light — blue fluorescence from the half-cyclized product and green fluorescence from the fully-cyclized product. Solvents were removed from the solution by rotary evaporation, and the remaining material was dissolved in a minimal amount of DCM. Methanol was added to precipitate fully-cyclized **1a** and its half-cyclized form, and the products were filtered using a Millipore vacuum apparatus, yielding 83.0 mg (89%) of the yellow solid. Alternately, the fully cyclized form can be selectively precipitated and the solids filtered before additional methanol is added to precipitate the half cyclized form given solubility differences between the two species. This fractionation by solubility differences thus allowed the isolation of the fully-cyclized **1a-d** from the half cyclized products; subsequent Scholl cyclizations on the half cyclized products thus yield **1a'-d'**.

6.5. General procedure for ring closure via Scholl cyclization.

A minimal amount of DCM was used to dissolve 83 mg (0.110 mmol) of **1a** and its half-cyclized form, and the solution was sealed in a roundbottom flask with a rubber septum. Iron (III) chloride (143 mg, 0.882 mmol) was dissolved in a minimal amount of nitromethane (1 mL) and added dropwise to the flask, making the solution dark green. The reaction was stirred overnight at room temperature until silica gel chromatography showed only green fluorescence that is attributed to the fully-cyclized product. The reaction was quenched with the addition of methanol, which also caused the fully-cyclized yellow products to precipitate out of solution. The product was isolated by filtration with a Millipore vacuum apparatus without further purification yielding 43.7 mg (53%).

References for Chapter 6

[1] van de Cratts, A.M.; Warman, J.M. Fechtenkötter, A.; Brand, J.D.; Harbison, M.A.; Müllen, K. *Adv. Mater*. **1999,** *11,* 1469-1472.

[2] Xiao, S.; Myers, M.; Miao, Q.; Sanaur, S.; Pang, K.; Steigerwald, M.L.; Nuckolls, C. *Angew. Chem,. Int. Ed.* **2005,** *44*, 7390-7394.

[3] Xiao, S.; Tang, J.; Beetz, T.; Guo, X.; Tremblay, N.; Siegrist, T.; Zhu, Y.; Steigerwald, M.L.; Nuckolls, C. *J. Am. Chem. Soc.* **2006,** *128,* 10700-10701.

[4] Tremblay, N.J.; Gorodetsky, A.A.; Cox, M.P.; Schiros, T.; Kim, B.; Steiner, R.; Bullard, Z.; Sattler, A.; So, W.-Y.; Itoh, Y.; Toney, M.F.; Ogasawa, H.; Ramirez, A.P.; Kymissis, I.; Steigerwald, M.L.; Nuckolls, C. *ChemPhysChem* **2010,** *11,* 799-803.

[5] Wong, W.W.H.; Singh, T.B.; Vak, D.; Pisula, W.; Yan, C.; Feng, X.; Williams, E.L.; Chan, K.L.; Mao, Q.; Jones, D.J.; Ma, C.-Q.; Müllen, K.; Baüerle, P.; Holmes, A.B. *Adv. Func. Mater.* **2010,** *20,* 927-938.

[6] Unpublished data.

[7] Etani, S.; Kaji, T.; Ikeda, S.; Mori, T.; Kikuzawa, Y.; Takeuchi, H.; Saiki, K. *J. Phys. Chem. C* **2009,** *113,* 6202-6207.

[8] Mori, T.; Kikuzawa, Y.; Takeuchi, H. *Org. Electron.* **2008,** *9,* 328-332.

[9] Gorodetsky, A.A.; Chiu, C.Y.; Schiros, T; Palma, M.; Sattler, W.; Kymissis, I.; Steigerwald, M.; and Nuckolls, C. *Angew. Chem,. Int. Ed.* published online Sept. 16,

2010; DOI: 10.1002/anie.201004055.

[10] Plunkett, K.N.; Godula, K.; Nuckolls, C.; Tremblay, N.; Whalley, A.C.; Xiao, S. *Org. Lett.* **2009,** *11*, 2225-2228.

[11] Neidlein, R.; Winter, M. *Synthesis* **1998**, 1362.

[12] a) Miyaura, N.; Suzuki, A. Chem. Rev. **1995,** *95*, 2457; b) Bauer, A.; Miller, M.W.; Vice, S.F.; McCombie, S.W. *Synlett* **2001**, *2*, 254.

[13] Mallory, F.B.; Wood, C.S.; Gordon, J.T.; Lindquist, L.C.; Savitz, M.L. *J. Am. Chem. Soc.* **1962,** *84*, 4361-4362.

[14] Liu, L.; Yang, B.; Katz, T.; Poindexter, M.K. *J. Org. Chem.* **1991,** *56*, 3769-3775.

[15] The unit cell dimensions for **1c**: *a* = 12.966 Å; *b* = 8.566 Å; *c* = 14.310 Å; □ = 90.27°. The unit cell dimensions for **1c'**: *a* = 14.740 Å; *b* = 13.624 Å; *c* = 16.060 Å; □ = 99.12°.

[16] Wiberg, K.B.; Murcko, M.A. *J. Am. Chem. Soc.* **1988,** *110*, 8029-8038.

[17] Coates, G.W.; Dunn, A.R.; Henling, L.M.; Dougherty, D.A.; Grubbs, R.H. *Angew. Chem., Int. Ed.* **2003,** *36*, 248-251.